ACTIVE VIBRATION CONTROL OF FLEXIBLE PANELS USING PIEZOELECTRIC ACTUATORS- IIR FILTERING BASED ADAPTIVE APPROACHES AND AN INDUSTRIAL DEMONSTRATION

by

Utku Boz

A Dissertation Submitted to the
Graduate School of Sciences and Engineering
in Partial Fulfillment of the Requirements for
the Degree of

Doctor of Philosophy
in
Mechanical Engineering

KOÇ UNIVERSITY

February 2016

Koç University

Graduate School of Sciences and Engineering

This is to certify that I have examined this copy of a doctoral thesis by

Utku Boz

and have found that it is complete and satisfactory in all respects,
and that any and all revisions required by the final
examining committee have been made.

Committee Members:

_____

Ipek Basdogan, Ph. D. (Advisor)

_____

Yaman Arkun, Ph. D.

_____

Kenan Yüce Şanlıtürk, Ph. D.

_____

Alper Ertürk, Ph. D.

_____

Arif Karabeyoğlu, Ph. D.

Date: _____

ABSTRACT

ACTIVE VIBRATION CONTROL OF FLEXIBLE PANELS USING PIEZOELECTRIC ACTUATORS- IIR FILTERING BASED ADAPTIVE APPROACHES AND AN INDUSTRIAL DEMONSTRATION

Consequences of severe vibrations may lead to decrease in service life or even cause damage on the components of a structure. The passive isolation techniques are not generally feasible and efficient for low frequency vibration suppression; instead, Active Vibration Control (AVC) can be used to suppress the low frequency vibrations. The contributions of this thesis in the field of AVC can be grouped in two main cathegories. First cathegory is to develop IIR filtering based adaptive approaches for active vibration control and demonstrate the efficiency of the developed methodologies on two different case studies. The other category is to develop a methodology to suppress vibration level on the wheelhouse of a newly designed commercial vehicle produced by Ford OTOSAN.

The first case study on adaptive control includes an implementation of an IIR filter integrated with the online modelling secondary path modelling methodology to develop a novel controller configuration for AVC. In order to develop such a methodology, Filtered-U LMS (FULMS) algorithm is used to update the controller filter parameters while a recently developed online secondary path modelling algorithm continuously update the modeling filter parameters. The controller is implemented on a vehicle panel and piezoelectric patches (PZT actuators) are used as sensors and actuators for their low-weight, and high performance properties.

The second case study on adaptive control includes implementation of Steiglitz-McBride (SM) IIR filtering technique for active vibration control. The Steiglitz-McBride

algorithm is demonstrated on an experimental setup where the controller is implemented on a quarter body in white vehicle where PZT actuators are attached on one of the panels. Later, the algorithm is computationally enhanced by developing a novel approach (hybrid SM) which combines the frequency domain adaptive filtering methodology with the classical algorithm. Efficiency of the developed methodology is demonstrated both experimentally and numerically.

Finally, an active vibration control methodology on a real vehicle is demonstrated for controlling the road induced disturbances. A vehicle produced by Ford-OTOSAN Company is used in the AVC studies. Two different feedback controller approaches, Positive Position Feedback (PPF) and Linear Quadratic Regulator (LQG), are implemented and compared. The resuls showed that both algorithms performed well at the problematic region. However, the vibration level at the higher modes are amplified when the PPF algorithm is used whereas this problem is eliminated when the LQG controller is used.

All of the studies presented in this thesis demonstrate that the developed AVC approaches are effective in terms of vibration suppression and can be used effectively for solving vibration related problems in flexible panels.

Keywords: Active Vibration Control, Adaptive Control, IIR Filtering, Steiglitz-McBride Algorithm, FXLMS, FULMS, Feedback Control, NVH

ÖZETÇE

ESNEK PANELLERİN PZT YAMALAR ARACILIĞI İLE AKTİF TİTREŞİM KONTROLÜ- SONSUZ DÜRTÜ CEVAPLI (IIR) FİLTRE TABANLI ADAPTİF YAKLAŞIMLAR VE BİR ENDÜSTRİYEL ÇÖZÜM

Bu çalışmada amaç, düşük frekanslardaki titreşim seviyelerinin bastırılmasına yönelik adaptif aktif titreşim control yaklaşımlarının geliştirilmesi ve bunun yanısıra geri beslemeli kontrol yaklaşımı ile yol tabanlı titreşim problemlerinin ticari bir araç üzerinde çözümlenmesidir.

İlk kısımda IIR filtreler ile çevrimiçi modelleme yaklaşımını birleştiren bir özgün yaklaşım geliştirilmiştir. Bir kompleks panel üzerinde geliştirilen yaklaşımın numerik ve deneysel gerçeklemesi yapılmıştır. PZT yamalar seçilen sensör ve tahrik kaynaklarıdır. 4 PZT yama yüzeye sabitlenmiş ve bunlardan bir tanesi istenmeyen titreşimi simüle etmek için kullanılmıştır. Diğer yamalardan bir tanesi kontrol kaynağı için kullanılmış, kalan yamalar ise sensör olarak değerlendirilmiştir. Belirlenen konfigürasyon kullanılarak geliştirilen kontrolör uygulanmıştır.

İkinci kısımda ise, Steiglitz-McBride (SM) algoritması tabanlı özgün bir yaklaşım geliştirilmiş ve uygulanmıştır. Gerçek bir aracın 4 te 1 i kullanılarak bir kompleks yapı oluşturulmuş ve geliştirilen yaklaşımın numeric ve deneysel uygulamasında kullanılmıştır. Yapı üzerine 3 adet PZT yama yapıştırılmıştır. 1 sallayıcı aracılığı ile istenmeyen titreşim simüle edilmiş ve 1 adet PZT yama kontrol kaynağı olarak kullanılmıştır. Kalan yamalar ise sensör olarak kullanılmış ve belirlenen konfigürasyonla kontrol uygulaması yapılmıştır.

Son kısımda ise Doğrusal Karesel Gaus (LQG) tabanlı geri beslemeli kontrolcü kullanılarak aktif titreşim kontrol uygulaması Ford Araç Firması tarafından üretilen bir ticari araç üzerinde uygulanmıştır. Bu amaçla 2 adet PZT yama yüzey üzerine yapıştırılmış,

1 adet yama kontröl kaynağı olarak kullanılırken diğeri ise sensör olarak kullanılmıştır. Belirlenen konfigürasyon ile kontrol uygulaması yapılmış ve gerçek yol üzerinde araç hareket halinde iken performans değerlendirilmiştir. PZT yamaya ek olarak 2 adet ivmeölçer aracılığı ile yapının uzak kısımlarındaki titreşim seviyeleri de gözlemlenmiştir.

Tüm kısımlarda elde edilen sonuçlar göstermiştir ki; geliştirilen ve uygulanan yaklaşımların hepsi titreşim seviyesini azaltmada başarılı olmuş ve pasif yaklaşımlara etkili bir alternative olarak kullanılabilecekleri kanıtlanmıştır.

Anahtar Kelimeler: Aktif Titreşim Kontrolü, Adaptif Kontrol, IIR Filtreleme, Steiglitz-McBride Algoritması, FXLMS, FULMS, Geri Beslemeli Kontrol, NVH

ACKNOWLEDGEMENTS

I gratefully thank my supervisor Assoc. Prof. Ipek Basdogan for her valuable support and wisdom. Her proficiency in vibration analysis and professional view on research guided me in the times that I think it is impossible to endure. I also thank thesis comitee members Prof. Yaman Arkun, Prof. Arif Karabeyoğlu, Prof. Kenan Yüce Şanlıtürk and , Prof. Alper Ertürk for their valuable support and critical reading of my work. I would like to thank TUBITAK for the funding and scholarship granted during my PhD. I also thank Ford Motor Company and Ford OTOSAN for their support.

I also thank Serkan Külah, Denizhan Edeer, Ramazan Karataş and Engin Çukuroğlu for their friendship even after our professional paths are separated. They are the brothers that I have in this life.

I thank Güray Kuzu and Barış Çağlar for their companionship and support as home mates and sidekicks. They helped me to create peaceful and funny off-work time in my home.

I also appreciate Fatma Virdil and Mehmet Ayyıldız for their valuable support in my hard times. I always knew that they are entrusted friends and secret keepers.

Without, VALUE and RML crew, especially Ömer, Ozan, Ahmet and Yasemin, my spare times in Koç universtiy would not be funny and motivating.

Finally I would like to appreciate my mother Ayten, my father Celaleddin, my sister Ukte and my other half Kübra. Their love, support and respect to my decisions, their guidance in love and their endeavours on my well being led me to the position I am in now. I love you all and I owe my success to your presence.

TABLE OF CONTENTS

LIST OF TABLES

LIST OF FIGURES

NOMENCLEATURE

x(n)	the reference or input signal for any time instant n
y(n)	output of the adaptive filter
e(n)	error signal
$\mathbf{W}(n)$	FIR filter coefficients
$\mathbf{X}(n)$	vector of reference signal samples
$\hat{g}_{(.)}$	gradient operator
μ,	adaptation step size
$\mathbf{A}(n)$	Forward loop coefficients of IIR filter
$\mathbf{B}(n)$	Feedback loop coefficients of IIR filter
$\mathbf{D}(n)$	vector of desired signal samples
$\mathbf{Y}(n)$	vector of output samples of IIR filter
$\mathbf{P}(\boldsymbol{z})$	primary path
$\mathbf{S}(\boldsymbol{z})$	secondary path
$\widehat{\mathbf{S}}(\boldsymbol{z})$	secondary path model
$\mathbf{X_f}(n)$	filtered reference signal vector
$\mathbf{Y_f}(n)$	filtered output signal vector
f(n)	secondary path filter modeling error
$v_m(n)$	identification signal
v(n)	modified identification signal
$\rho(n)$	power ratio
$P_f(n)$	power of the f(n)
$P_e(n)$	power of the e(n),

λ	forgetting factor between 0.9 and 1
G(n)	the gain scheduling parameter
$\sigma_{v_{min}}, \sigma_{v_{max}}$	min and max variances of the modified identification signal.
R(n)	mean square error ratio between e(n) and d(n)
$pf_{(.)}(n)$	prefiltering of a signal
$\boldsymbol{PF}_{(.)}(n)$	prefiltered signal vector
m	block index
$(.)^H$	Complex Conjugate
$\mathbf{f}_{(.)}$	%50 overlap vector processing
$\mathbf{F}_{(.)}$	FFT of $\mathbf{f}_{(.)}$
$\mathbf{R}_{(.)}$	Frequency domain gradient
$\mathbf{r}_{(.)}$	Time domain conversion of $R_{(.)}$
δ	Modal coordinates of the target structure
η	PPF compensator coordinate
ω,ω_f	Structure and PPF filter frequencies
ζ,ζ_f	Structural and PPF compensator damping ratios
g	Scalar gain of the PPF controller.
P_k	Error covariance matrice
K_{lqr}	LQR Gain
K_{obs}	Kalman Gain

Chapter 1

INTRODUCTION

1.1 Overview

Consequences of severe vibrations may lead to decrease in service life or even cause damage on the components of a structure. To avoid such effects, active vibration control has been implemented widely in the literature. Beginning from the 1980s, researchers have designed and applied active vibration control on lightly damped structures with smart materials for solving low frequency vibration problems. Among the first few pioneering studies that combines smart material technology with active vibration control, Bailey and Hubbard [1] utilized piezoelectric materials in the form of a distributed actuator for the active damping of a cantilever beam. Later, Crawley and Luis [2] developed an analytical model of a surface bonded and embedded piezoelectric actuator patch. They predicted response of the host structure together with the piezoelectric patch with their model and verified their modeling methodology experimentally for various host structures.

There are review articles discussing fundamental aspects of active vibration control using Lead-Zirconate-Titanate (PZT) type piezoelectric actuators in the literature. Rao and Sunar [3], published a review paper addressing the use of piezoelectric materials as sensors and actuators for control of flexible structures. In this review paper, they presented the control strategies and illustrated the efficiency of those strategies by presenting different case studies available in literature. Loewy [4] reviewed the key applications of smart structures in aeronautical applications with potential uses. Aridogan and Basdogan [5] reviewed the active vibration and noise control for plate-like structures with piezoelectric

applications. In this work, they categorized and described different control architectures and presented various applications that involved vibration control.

It is important to choose an applicable control strategy and carefully position the sensor/actuator pair for effective active vibration control. Alkhatib and Golnaraghi [6] reviewed the controller architectures and presented the general design procedures for active vibration control systems. They presented the advantages and disadvantages of different controller architectures with various examples. Gupta et al. [7] reviewed the optimal positioning of piezoelectric sensors and actuators for various host structures including cantilevered and simply supported structures. They presented the optimization techniques and gave the results of former research studies.

In the mean time, the piezoelectric materials also attracted attention of the researchers working on noise control. Chopra [8] stated that most of the applications invoving piezoelectric materials focus on minimization of vibration levels; however, interior and exterior noise reduction using piezoelectric materials have also a potential research area for control of structure born noise. Hanselka [9] named the use of smart materials in active noise and vibration control as an innovative technology and analyzed active noise reduction for different applications including plate-like structures. In their studies, piezoelectric materials served as sensors and actuators to reduce structural-borne noise and the results showed that this application of technology was feasible and advantageous.

In the following section, an overview of active vibration control systems is presented and various architectures are discussed.

1.2 Active Vibration Control

Active vibration control means to suppress vibration level by inducing an external excitation which has cancelling effects on the original vibration characteristics. The develeopments in the signal processing technology and the computational power enhanced the use of active vibration control on various structures [6]. In the actve vibration control

applications, usually an undesired vibration source induces the disturbance on the system. The vibration level of the structures are measured with sensors and control actuators are used to create counter effects at the actuator locations to suppress the vibration.

Different controller architectures can be implemented to achieve a succesfull active vibration control system. In the following section, an overview of the controller algorithms for active vibration control systems are presented.

1.2.1 Active Vibration Control Architectures

Generally, tracking a trajectory and rejecting a disturbance are the main goals in control applications. Rejecting a disturbance can be achieved via feedback and feedforward controllers. Feedback controllers utilize the level of the sensor signal for generating a control input. In feedforward control, major disturbance loads are measured at the source and on the structure to generate the controller output. The advantages and disadvantages of those controllers are listed in Table1.1.

Table 1. 1 Advantages and Disadvantages of Control Algorithms on Active Vibration Control

Type of control	Advantage	Disadvantage
Feedback		
Active Damping	• Simple to implement • Does not require accurate model of plant • Guaranteed stability when sensors an actuators are collocated	• Effective only near resonance
Model Based(LQR,LQG,H_∞...)	• Global method • Requires accurate model of the plant • Attenuates all disturbance within the control band-with	• Limited bandwidth • Requires low delay for wide bandwidth • Spillover
Feedforward		
Adaptive filtering	• No model is necessary • Robust to inaccuracies in plant estimate and to change in plant transfer functions • More effective for narrowband disturbance	• Reference/error signal is required • Large amount of real-time computations

1.2.1.1 Feedback Control

Feedback algorithms are divided to two general groups. Active damping systems and model based controllers [10]. Among active damping systems, proportional feedback control is widely used as the control architecture. General form of the feedback control configuration is shown in Figure 1.1.

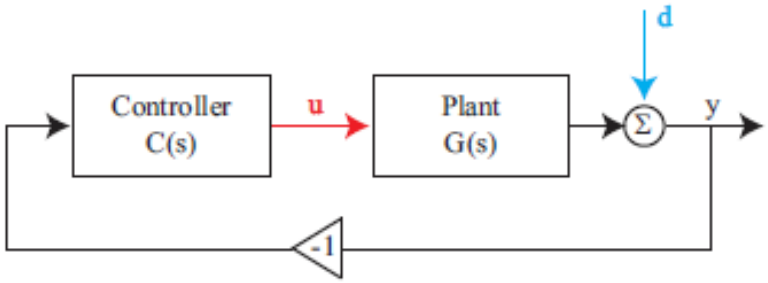

Figure 1. 1 Generic Feedback Controller Block Diagram

Proportional feedback control is simply to control a plant by feeding proportionally amplified error signal to a control actuator. Using a predefined sensor, error measurements on the sensor location is acquired and processed. Processing of the error signal means to generate a control signal which is proportionally related to the error signal in magnitude. Next step is to transmit the control signal to the control actuator. Different researchers used proportional feedback algorithms for vibration control applications. Fakhari et al numerically analyzed effectiveness of feedback control algorithms for functionally graded plates [11]. Okumura and his colleagues analyzed feedback control behavior of a clamped plate numerically for surface bonded PZT patches [12]. Boz et al. used an analog controller to suppress vibration on a fully clamped plate [13].

Model based feedback controllers utilize structural models. Models for accurate system representation are created via different methods such as experimental modeling, theoretical modeling and finite element modeling (FEM). Model based controllers are classified as robust and optimal controllers. Optimal controller can be defined as the controller type that minimizes a cost function based on the available system model. In optimal control, measured or observed states are fed back to the system after matrix multiplication of states with a predefined optimal gain matrix. Weights of the states and the inputs are tuning parameters for the cost function minimization which in turn affects the optimal gain matrix.

In the literature, many researchers used optimal controllers for vibration suppression. Ryall et al. analyzed effectiveness of optimally placed piezoceramic patches using optimal feedback control [14]. Boz et.al implemented optimal controller on a fully clamped plate to attenuate vibrations and compared the performance of the optimal controller with the velocity feedback algorithm [15].

Robust controllers concentrate on balancing the performance and stability of the control architecture when there is uncertainty in the system model and noise in both inputs and outputs of the system.[6]. LQG controllers are among the type of the controllers which offer robustness by incorporating the optimal control theory with a stochastic state estimator algorithm. This type of controller is used in Chapter 4 since the application presented is suitable for optimal control approach and may have model uncertainty due to different operation conditions. LQG minimizes an optimal cost function with consideration of the characteristics of system uncertainties. In literature, many researchers utilized LQG in active vibration control. Chomette et al. proposed an LQG controller and demonstrated its effectiveness for Printed Circuit Board (PCB) systems [16]. Hwang et al. demonstrated effectiveness of LQG controller for optimally placed sensors and actuators [17]. Sanda and Takashi utilized LQG to suppress flutter of aluminum wing plate [18]. Besides those

studies just explained in detail, there are other studies in literature concentrating on the implementation of the LQG for active vibration control [19-22].

1.2.1.2 Feedforward Control

There are different forms of the feedforward controllers. In this thesis, feedforward control approach is utilized in adaptive control applications in Chapters 2 and 3. Feedforward control architecture for adaptive control applications is given in Figure 1.2.

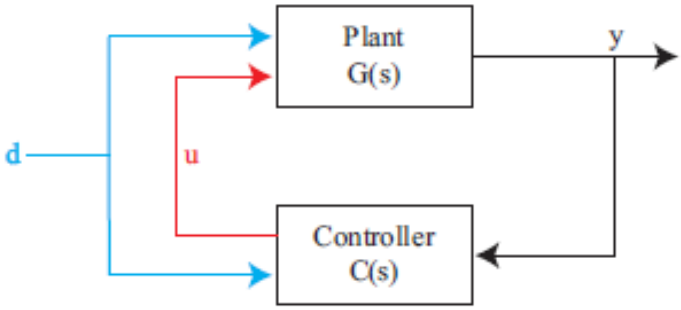

Figure 1. 2 Generic Feedforward Controller Block Diagram

In adaptive control applications the main goal is to find optimal filter parameters that ensure the best performance in terms of the control objective. Least mean square (LMS) based algorithms are widely used in adaptation process. The adaptation process in adaptive algorithms is based on the existence of an error between the output of the filter and the measured disturbance. In vibration problems, the measured vibration level is the error itself and its variation at every time step forms an error surface as the adaptive filter parameters change [23].

The adaptive feedforward control utilizes mainly two different filtering techniques. Those are Finite Impulse Response (FIR) filters and Infinite Impulse Response (IIR) filters. The descriptions of those filtering techniques are given in detail in section 2.2.

FIR filtering based algorithms offer optimal convergence of the set of parameters and unconditional stability. However, FIR filtering based algorithms relies on two basic assumptions. First assumption is; the reference signal is highly correlated with the vibration source signal and the other is; the controller output should not affect the reference signal [24]. The condition regarding the correlated nature of the vibration source and the reference signal must be satisfied to ensure that the controller works properly. In real life applications, the interference of the reference signal with the control signal is unavoidable. Furthermore, if the structural damping is low, the length of the filter must be increased to compensate for that.

On the other hand, The IIR filtering offers advantage of representing the system dynamics with less filter parameters and compensating for the interference of the reference signal with the controller signal. However, there is possibility of the unstability of the IIR filter and convergence to the local minimum when the output error form is used for adaptation. In chapter 3 and chapter 4, two IIR filtering based approaches are used for vibration suppression.

1.2.2 Sensors and Actuators

In this section, an overview of the literature about piezoelectric sensor and actuator is presented

Piezoelectric materials have a recoverable strain of 0.1 % under electrical field. Those materials can be used as sensors and actuators [25]. Piezoelectric materials are divided into two major categories; Polymers and ceramics. Piezopolymers are recruited as sensors mostly since they require extremely high voltage and have limited control authority.Piezoceramics are used as both actuators and sensors. Piezoceramics are effective even in ultrasonic applications and suit well for the applications with high precision even in

nanometer range. The best known piezoelectric material is Lead Ziconate Titanate (PZT) [26].

Piezoelectric materials are started to be used in vibration control over 25 years ago. Bailey and Hubbard [1] designed a system to control vibration of cantilever beam. In time, new materials like PVDF and PZT are introduced and researchers utilized those materials for their applications. Piezoelectric materials are used in many research studies. Aoki et al [27] analyzed piezoelectric materials for velocity feedback control. Caruso et al simulated application of piezoelectric materials to suppress vibration of steel cantilevered plate [28]. Chellabi et al applied state feedback controller to plate structure utilizing piezoelectric materials [29]. Besides those studies, there are other simulation and experiment based vibration control analysis with piezoelectric materials [30-32].

1.3 Contributions & Outline of the Thesis

Considering all of the advancements in the previous studies, this thesis can be grouped in two main contribution categories. First contribution category can be summarized as developing IIR filtering based adaptive approaches for active vibration control systems and demonstrate the efficiency of the developed methodologies on two different case studies by using surface-bonded piezoelectric patches as actuators and sensors. The details of the first category are

In the first case study presented in Chapter 2:

- IIR filtering based adaptive algorithm is combined with online modelling of the plant dynamics such that the controller compensates for the changing plant conditions.
- The efficiency of the developed approach is demonstrated both numerically and experimentally on a flexible structure which is a vehicle panel and

compared with FIR filtering based counterpart to show that the approach yields faster convergence

In the second case study presented in Chapter 3:

- Frequency Domain Adaptive Filtering (FDAF) approach is used in combination with Steiglitz-McBride (SM) IIR filtering for vibration control of a quarter body in white vehicle where PZT actuators are attached on one of the panels.
- Efficiency of the developed methodology is demonstrated both experimentally and numerically.

Second contribution category can be summarized as developing a methodology to suppress the vibrations on the wheelhouse of a newly designed commercial vehicle produced by Ford OTOSAN. This study was presented in Chapter 4 and it involved the demonstration of the Active Vibration Control methodology while the vehicle was running in real operating conditions. In operating conditions, since the disturbance on the structure is induced by various sources, it is extremely difficult to find a suitable position for the reference sensor. For that reason, in this study a feedback controller is used. The details of the second category are

- Road induced disturbances on the wheelhouse are suppressed by using Active Vibration Control and piezoelectric sensor/actuators in the operating conditions.
- A stand alone controller configuration with low power consumption is developed in combination with a signal conditioner unit. The developed configuration is suitable for the vehicle applications in operating conditions and can be powered by the electrical supply available in the vehicle.

Chapter 2

COMBINATION OF THE ADAPTIVE IIR FILTERING WITH ONLINE SECONDARY PATH MODELING

2.1 Introduction

In this chapter, adaptive IIR filtering technique is implemented in combination with the online modelling secondary path modelling methodology to develop a novel controller configuration for Active Vibration Control. In order to develop such methodology, Filtered-U LMS (FULMS) algorithm is used to update the controller filter parameters while a recently developed online secondary path modelling algorithm continuously update the modeling filter parameters. Piezoelectric patches are the preferred sensors and actuators for their low-weight, high performance properties. Using PCI interface of a host computer, the sensor signal is transferred to a computer and the developed methodology is implemented via a rapid prototyping controller unit to generate the output for vibration suppression.

2.2 Adaptive Filtering

Digital filters are the systems that perform mathematical operations on a sampled, discrete-time signal to satisfy certain application requirements. It is possible to design digital filters which have fixed coefficients, however such configuration depends on well-defined operation requirements. On the other hand, in real life applications, it is common to have a system where the specifications are not explicitly known or time varying [33]. In such cases the solution is to utilize digital filters with time-varying coefficients, known as adaptive filters.

Since the specifications are not known explicitly, in adaptive filtering two set of signals namely, reference and desired signals, are used to determine the update of the adaptive filter parameters. Figure 2.1 shows the general adaptive filtering configuration.

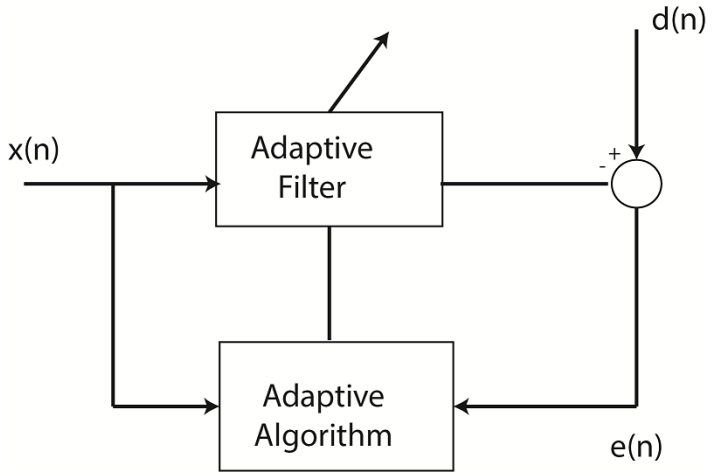

Figure 2. 1 General Form of the Adaptive Filter

Here x(n) is the reference or input signal for any time instant n. The y(n) is the output of the adaptive filter and the e(n) is the error which is calculated as the difference between the desired signal and the filter output. The error signal e(n) and reference signal x(n) are then used to minimize a pre-defined objective function for appropriate updating of the filter coefficients.

In sections 2.2.1 and 2.2.2, Finite Impulse Response (FIR) filters and Infinite Impulse Response (IIR) filters. are introduced.

2.2.1 Finite Impulse Response (FIR) Filters

An FIR filter is defined as a filter whose impulse response settles to zero in finite time. The output of the FIR filter is obtained by using Equation 2.1

$$y(n) = \sum_{i=0}^{N-1} w_i(n)\, x(n-i) = \mathbf{W}^T(n)\mathbf{X}(n) \qquad 2.1$$

Here the $w_i(n)$ shows the i^{th} coefficient of the FIR filter. The reference signal x is shifted by the index of the corresponding filter parameter and the result is the summation of the multiplication of the filter coefficient with the corresponding shifted reference signal value. Here $\mathbf{W}(n) = [w_0(n)\ w_1(n) \dots w_{N-1}(n)]$ is the (Nx1) vector of the filter weight coefficients at time n and $\mathbf{X}(n) = [x(n)\ x(n-1) \dots x(n-N+1)]$ includes the N most recent reference signal values. Figure 2.2 illustrates the operation of the FIR filter.

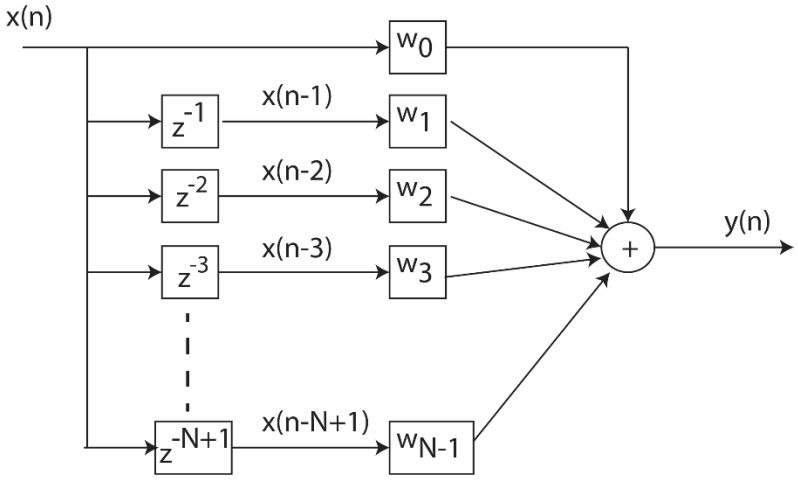

Figure 2. 2 FIR filter

The adaptation procedure is considered as an optimization problem and least mean square (LMS) algorithm is a widely utilized line search algorithm used for the adaptation. The LMS algorithm is based on the gradient descent algorithm and for detailed information on the algorithm please refer to [33]. The objective function of the LMS algorithm is

$$J = E\{e^2(n)\} \quad 2.2$$

As explained in the section 2.1 the error signal e(n) is the difference between the desired signal d(n) and the filter output y(n) yielding

$$e(n) = d(n) - y(n) \quad 2.3$$

Replacing the e(n) in the Equation 2.2 with the Equation 2.3 and combining with the the objective function becomes

$$J = E\{(d(n) - \mathbf{W}^T(n)\mathbf{X}(n))^2\} \quad 2.4$$

In order to calculate the gradient of the objective function with respect to W(n), the derivative of the J with respect to $\boldsymbol{W}$ must be calculated. Please note that rather than calculating the expected value of the error square and deriving it with respect to W, it is possible to replace the objective function with the $e^2(n)$. Replacing the J with the $e^2(n)$ and taking the derivative of the $e^2(n)$ with respect to W(n) yields the gradient vector $\hat{g}_w$ as

$$\hat{g}_w = \frac{\partial e^2(n)}{\partial W} = \frac{\partial (d(n) - \mathbf{W}^T(n)\mathbf{X}(n))^2}{\partial W} = -2e(n)\boldsymbol{X}(n) \quad 2.5$$

The resulting gradient-based update equation then becomes

$$\boldsymbol{W}(n+1) = \boldsymbol{W}(n) - \mu\hat{g}_w = \boldsymbol{W}(n) + 2\mu e(n)\boldsymbol{X}(n) \quad 2.6$$

Here μ is the step size for the adaptation and should be chosen in a range to guarantee convergence.

2.2.2 Infinite Impulse Response (IIR) Filters

An IIR filter is a filter whose impulse response settles to zero in infinite time due to recursion used in calculation of the output based on the one or more past and present outputs of the filter itself. The recursion due to such nature of the IIR filters may lead to unstability. On the other hand, it offers advantage of representing the required dynamics with less number of total filter parameters than the FIR filters. The recursive nature of the IIR filters yields a filter transfer function of

$$H(z) = \frac{a_0 + a_1 z^{-1} + \cdots + a_{M-1} z^{-M+1}}{1 - b_1 z^{-1} - \cdots - b_N z^{-N}} \quad 2.7$$

Here the a's are the coefficients of the forward loop while the b's are the coefficients of the feedback loop. There are predominantly two forms of the IIR filters used in the adaptive filtering. Those are equation error and the output error formulations.

2.2.2.1 Equation Error Formulation

Considering the Figure 2.3 below, IIR filter output can be calculated in the equation error form using the reference signal and the one or more previous values of the desired signal.

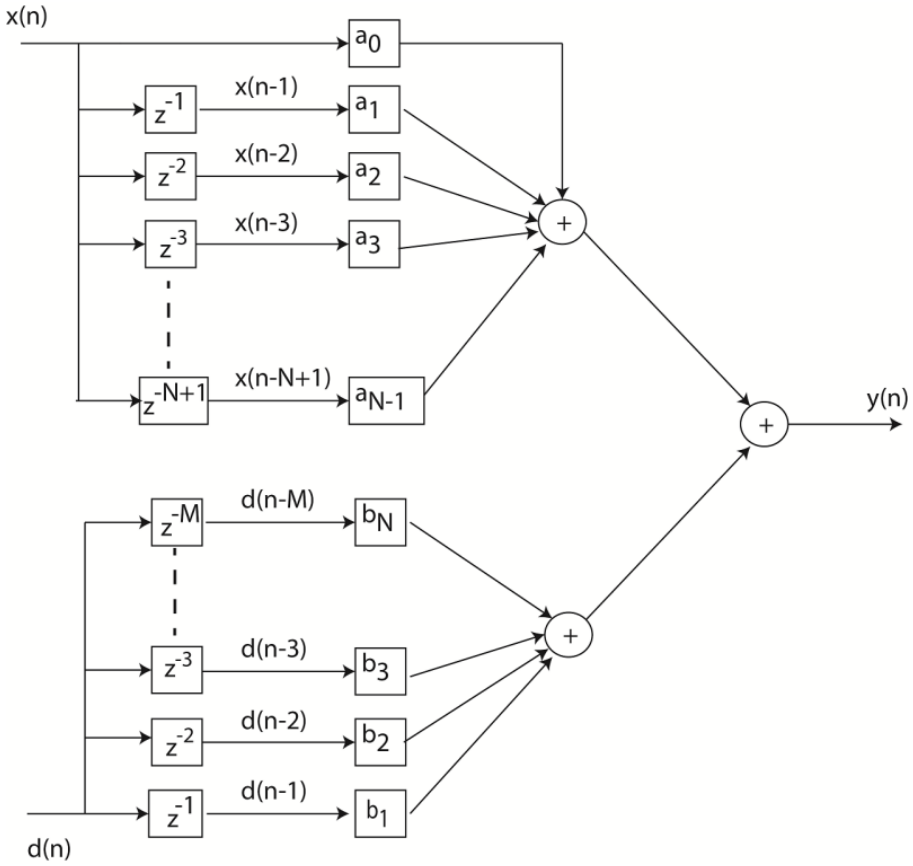

Figure 2. 3 IIR Filter in Equation Error Form

Output of the IIR filter in equation error form is calculated by Equation 2.8

$$y(n) = \sum_{i=0}^{N-1} a_i(n)\, x(n-i) + \sum_{j=1}^{M} b_j(n)\, d(n-j) = \mathbf{A}^T(n)\mathbf{X}(n) + \mathbf{B}^T(n)\mathbf{D}(n) \qquad 2.8$$

Here the $a_i(n)$ shows the i^{th} coefficient of the forward loop of the IIR filter. The $b_i(n)$ shows the i^{th} coefficient of the feedback loop of the IIR filter. The reference signal x(n) and the desired signal d(n) are shifted by the index of the corresponding filter parameter and the result is the summation of the multiplication of the filter coefficient with the corresponding shifted reference and desired signal values. Here $\mathbf{A}(\mathrm{n}) = [\mathrm{a}_0(\mathrm{n})\ \mathrm{a}_1(\mathrm{n})\ \ldots\ \mathrm{a}_{\mathrm{N}-1}(\mathrm{n})]$ is the (Nx1) vector of the filter weight coefficients for the forward loop of the IIR filter at time n and $\mathbf{B}(\mathrm{n}) = [\mathrm{b}_1(\mathrm{n})\ \mathrm{b}_2(\mathrm{n})\ \ldots\ \mathrm{b}_{\mathrm{M}}(\mathrm{n})]$ is the (Mx1) vector of the filter weight coefficients for the feedback loop. $\mathbf{X}(\mathrm{n}) = [\mathrm{x}(\mathrm{n})\ \mathrm{x}(\mathrm{n}-1)\ \ldots \mathrm{x}(\mathrm{n}-\mathrm{N}+1)]$ includes the N most recent reference signal values while $\mathbf{D}(\mathrm{n}) = [\mathrm{d}(\mathrm{n}-1)\ \mathrm{d}(\mathrm{n}-2)\ \ldots \mathrm{d}(\mathrm{n}-\mathrm{M})]$ includes the M most recent desired signal values.

For the equation error formulation, LMS algorithm can be used in parallel with the coefficient adaptation procedure of the FIR filters since the output of the equation error form IIR filter is nothing but combination of two FIR filters. Recalling Equation 2.2 and Equation 2.8 and combining them the objective function of the LMS algorithm becomes

$$J = E\left\{(d(n) - \underbrace{\mathbf{A}^T(n)\mathbf{X}(n) - \mathbf{B}^T(n)\mathbf{D}(n)}_{(\boldsymbol{\theta}^T(n)\boldsymbol{\varphi}(n))})^2\right\} \quad 2.9$$

Here $\boldsymbol{\theta}^T(n)$=[$\mathrm{a}_0(\mathrm{n})\ \mathrm{a}_1(\mathrm{n})\ \ldots \mathrm{a}_{\mathrm{N}-1}(\mathrm{n})\ \mathrm{b}_1(\mathrm{n})\ \mathrm{b}_2(\mathrm{n})\ \ldots \mathrm{b}_{\mathrm{N}-1}(\mathrm{n})$] and $\boldsymbol{\varphi}(n) = [\mathrm{x}(\mathrm{n})\ \mathrm{x}(\mathrm{n}-1)\ \ldots \mathrm{x}(\mathrm{n}-\mathrm{N}+1)\ \mathrm{d}(\mathrm{n}-1)\ \mathrm{d}(\mathrm{n}-2)\ \ldots \mathrm{d}(\mathrm{n}-\mathrm{M})]$. Recalling the derivation procedure of the parameter adaptation in section 2.2.1, it is possible to show that the gradient based update equation becomes

$$\boldsymbol{\theta}(n+1) = \boldsymbol{\theta}(n) - \mu\hat{g}_\theta = \boldsymbol{\theta}(n) + 2\mu e(n)\boldsymbol{\varphi}(n) \quad 2.10$$

Here μ is again the step size of the gradient descent algorithm. The equation error algorithm ensures the adaptive parameters to converge to the true set of parameters. However, if the desired signal is noisy, the result of the adaptation procedure becomes

biased. In some cases, such bias may yield set of parameters which are completely unsatisfactory[23].

2.2.2.2 Output Error Formulation

General output error formulation for IIR filters is shown in Figure 2.4. The main difference between the equation error and output error formulation is that the equation error formulation uses the desired signal while the output error formulation uses the actual output of the filter for the filter output calculation.

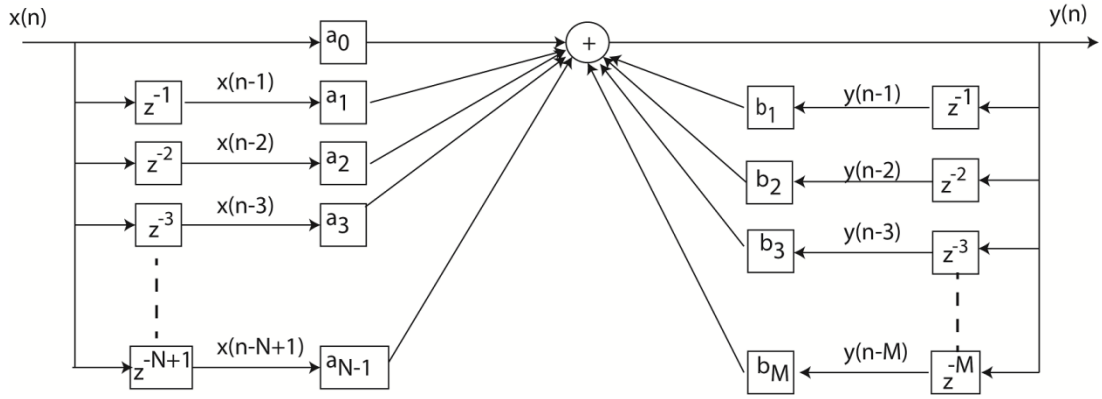

Figure 2. 4 IIR Filter in Output Error Form

The formulation for the calculation of output of the IIR filter in output error form is shown by Equation 2.11

$$y(n) = \sum_{i=0}^{N-1} a_i(n)\, x(n-i) + \sum_{j=1}^{M} b_j(n)\, y(n-j) = \mathbf{A}^T(n)\mathbf{X}(n) + \mathbf{B}^T(n)\mathbf{Y}(n) \qquad 2.11$$

Here the $a_i(n)$ shows the i^{th} coefficient of the forward loop of the IIR filter. The $b_i(n)$ shows the i^{th} coefficient of the feedback loop of the IIR filter. The reference signal x(n) and the filter output y(n) are shifted by the index of the corresponding filter parameter and the result is the summation of the multiplication of the filter coefficient with the corresponding shifted reference and filter output values. Here $\mathbf{A}(n) = [a_0(n)\ a_1(n) \ldots a_{N-1}(n)]$ is the (Nx1) vector of the filter weight coefficients for the

forward loop of the IIR filter at time n and $\mathbf{B}(n) = [b_1(n)\ b_2(n) \dots b_M(n)]$ is the (Mx1) vector of the filter weight coefficients for the feedback loop. $\mathbf{X}(n) = [x(n)\ x(n-1) \dots x(n-N+1)]$ includes the N most recent reference signal values while $\mathbf{Y}(n) = [y(n-1)\ y(n-2) \dots y(n-M)]$ includes the M most recent filter output values.

For the output error formulation, LMS algorithm can be used in parallel with the coefficient adaptation procedure of the FIR filters and the equation error IIR filters. However there is a problem in gradient calculation. Recalling Equations 2.2 and Equation 2.8 and combining them the objective function of the LMS algorithm becomes

$$J = E\left\{(d(n) - \underbrace{\mathbf{A}^T(n)\mathbf{X}(n) - \mathbf{B}^T(n)\mathbf{Y}(n)}_{(\boldsymbol{\theta}^T(n)\boldsymbol{\varphi}(n))})^2\right\} \quad 2.12$$

Here $\boldsymbol{\theta}^T(n)$=[$a_0(n)\ a_1(n) \dots a_{N-1}(n)\ b_1(n)\ b_2(n) \dots b_{N-1}(n)$] and $\boldsymbol{\varphi}(n) = [x(n)\ x(n-1) \dots x(n-N+1)\ y(n-1)\ y(n-2) \dots y(n-M)]$. Please note that the gradient estimation of the objective function requires deriving objective function with respect to coefficient vector b and the previous values of the y(n) are also function of the B as well. In order to calculate the gradient of the objective function with respect to $\boldsymbol{\theta}(n)$, the derivative of the J with respect to $\boldsymbol{\theta}(n)$, must be calculated. Please note that rather than calculating the expected value of the error square and deriving it with respect to $\boldsymbol{\theta}(n)$, it is possible to replace the objective function with the $e^2(n)$. Replacing the J with the $e^2(n)$ and taking the derivative of the $e^2(n)$ with respect to $\boldsymbol{\theta}(n)$, yields the gradient vector $\hat{g}_\theta$ as $\hat{g}_\theta = \frac{\partial e^2(n)}{\partial \boldsymbol{\theta}}$

This can be separated into feedback and feedforward parameters such as

$$\frac{\partial e^2(n)}{\partial a_i} = -2e(n)\frac{\partial y(n)}{\partial a_i} \quad 2.13$$

and

$$\frac{\partial e^2(n)}{\partial b_j} = -2e(n)\frac{\partial y(n)}{\partial b_j} \tag{2.14}$$

Evaluating those derivatives given in Equation 2.13 and 2.14 gives

$$\frac{\partial y(n)}{\partial a_i} = x(n-i) + \sum_{j=1}^{N} a_j(n)\frac{\partial x(n-j)}{\partial a_i(n)} \tag{2.15}$$

and

$$\frac{\partial y(n)}{\partial b_j} = y(n-j) + \sum_{i=1}^{N} a_i(n)\frac{\partial y(n-i)}{\partial b_j(n)} \tag{2.16}$$

Assuming that the convergence coefficient is small and the change in parameters are not significant the values of the derivations in Equations 2.15 and 2.16 becomes

$$\frac{\partial x(n-j)}{\partial a_i(n)} \approx \frac{\partial x(n-j)}{\partial a_i(n-j)}, and\ \frac{\partial y(n-i)}{\partial b_j(n)} \approx \frac{\partial y(n-i)}{\partial b_j(n-i)} \tag{2.17}$$

Thus $\frac{\partial y(n)}{\partial \boldsymbol{\theta}}$ becomes

$$\boldsymbol{\psi}(n) = \boldsymbol{\varphi}(n) + \sum_{j=1}^{N} a_j(n)\boldsymbol{\psi}(n-j)\,, where\ \boldsymbol{\psi}(n) = \frac{\partial y(n)}{\partial \boldsymbol{\theta}(n)} \tag{2.18}$$

The update equation for the IIR filter parameters become

$$\boldsymbol{\theta}(n+1) = \boldsymbol{\theta}(n) + 2Me(n)\boldsymbol{\psi}(n) \tag{2.19}$$

Where $M = \begin{bmatrix} \mu_{a_0} & 0 & 0 & 0 \\ 0 & \ddots & 0 & 0 \\ 0 & 0 & \ddots & 0 \\ 0 & 0 & 0 & \mu_{b_M} \end{bmatrix}$ is the diagonal matrix of convergence coefficients.

2.3 Adaptive FIR and IIR Filtering in Active Vibration Control

In section 2.2, the theory of FIR and IIR filters are explained in detail. In this section, the utilization of the FIR and IIR filters for the AVC application will be explained. The main difference between the adaptive filtering techniques and the adaptive form of the digital filtering for the AVC is the presence of the secondary path which is the dynamics

between the control actuator and the error sensor. Thus the additional dynamics of the secondary path should be included in the adaptation procedure. The FIR and IIR filtering based applications are widely used in active vibration control literature. Thus, it is suitable to present a literature review on the subject prior to the theoretical description of the algorithms utilized in this thesis

2.3.1 Literature Review

Finite Impulse Response (FIR) filter based adaptive algorithms are widely used in active vibration control. Among those algorithms, FXLMS algorithm is one of the commonly used algorithms because of its simplicity and effectiveness. Recently, Huang et. al developed a variable step-size FXLMS algorithm for a narrowband active noise control system [34]. They introduced a new objective function for the adaptive algorithm to include effects of the residual noise signal as well as variable step sizes. The proposed algorithm performed better than the original FXLMS algorithm in stationary noise environments with improved convergence rate similar to that of the Filtered-X Recursive Least Squares (FXRLS) algorithm. In another study by Yang et al., the authors proposed a random vibration power spectral density (PSD) reproduction control algorithm based on the frequency domain FXLMS algorithm [35]. They experimentally demonstrated that their algorithm ensured convergence of the iteration process with a high convergence rate. There are other forms of the FIR filtering based adaptive algorithms such as Filtered-X Recursive Least Square (RLS) and Modified FXLMS. For further information on those algorithms please refer to [23].

IIR filtering based algorithms are not popular as the FIR filtering based adaptive algorithms. The IIR filtering based algorithms are divided to two categories. Those are output error form and equation error form. Among the output error formulation based algorithms, FULMS is the most popular one. FULMS is first implemented by Kim et al. for

controlling noise propagation in ducts [36]. Recently Huang et.al, implemented FULMS in multi input multi output (MIMO) vibration control of a cantilevered plate [24]. Comparison of the FULMS and FXLMS performances in their study proved that FULMS ensured faster convergence. Gao et. al implemented and compared FXLMS and FULMS algorithms for active vibration control and reported the same observation about the convergence of the FULMS algorithm [37].

2.3.2 Filtered-X LMS (FXLMS) Algorithm

In this section, the theory of the FIR filtering based FXLMS and IIR filtering based FULMS are presented. FXLMS is a widely known adaptive filtering algorithm. The algorithm is slightly modified version of the Least Mean Square (LMS) algorithm and it utilizes gradient descent algorithm to update parameters of the FIR filter that generates the control output [23]. FXLMS algorithm considers the path from the control actuator to the error sensor, known as "secondary path", to avoid instability. FXLMS algorithm is preferred in adaptive vibration control due to its robustness and quick convergence properties [23]. In Figure 2.5, block diagram of the FXLMS algorithm is shown.

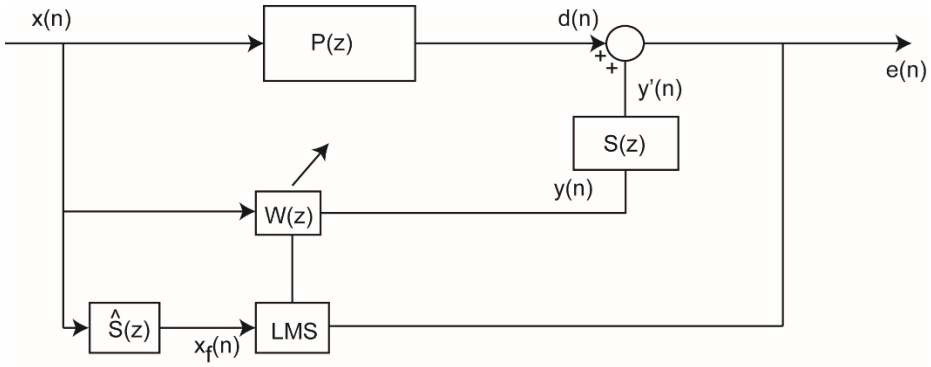

Figure 2. 5 Block diagram of the FXLMS controller

Here P(z) is the primary path between the disturbance source and the error sensor, S(z) is the secondary path, W(z) is the adaptive control filter, and $\hat{S}(z)$ is the model of the

secondary path which enables FXLMS algorithm to consider the dynamics between the control actuator and the error sensor. The signal, x(n) is the reference signal acquired by the reference sensor to mimic the characteristics of the disturbance at time n. The error signal e(n) is the measured vibration signal and it is simply superposition of the disturbance signal, d(n) and the controller output signal y'(n). y(n) is the control signal generated by the controller filter W(z). $\mathbf{W}$(n) is a (Nx1) vector of the filter weight coefficients at time n, and it can be written in the following form [23]:

$$\mathbf{W}(\mathrm{n}) = [\mathrm{w}_0(\mathrm{n})\ \mathrm{w}_1(\mathrm{n})\ \ldots\ \mathrm{w}_{\mathrm{N}-1}(\mathrm{n})]^T \tag{2.20}$$

The filter coefficients of the W(n) at every time step is updated as follows

$$\mathbf{W}(\mathrm{n}+1) = \mathbf{W}(\mathrm{n}) - 2\mu_{\mathrm{w}}\mathrm{e}(\mathrm{n})\mathbf{X_f}(\mathrm{n}) \tag{2.21}$$

where μ_w is the step size of the gradient descent algorithm and $\mathbf{X_f}$(n) is the (Nx1) filtered reference signal vector. The $\mathbf{X_f}$(n) is generated by filtering the reference sensor input by the secondary path model $\hat{\mathbf{S}}$ which is a *m*-order finite impulse response vector such that $\hat{\mathbf{S}} = [\hat{\mathrm{s}}_0\ \hat{\mathrm{s}}_1\ \ldots\ \hat{\mathrm{s}}_{m-1}]$.

The filtered reference signal vector $\mathbf{X_f}$(n) includes the N most recent filtered reference signal values as shown below

$$\mathbf{X_f}(\mathrm{n}) = [\mathrm{x_f}(\mathrm{n})\ \mathrm{x_f}(\mathrm{n}-1)\ \ldots\ \mathrm{x_f}(\mathrm{n}-\mathrm{N}+1)] \tag{2.22}$$

The elements of the vector $\mathbf{X_f}$(n) are calculated by

$$\mathrm{x_f}(\mathrm{n}) = \sum_{j=0}^{m-1} \hat{\mathrm{s}}_{\mathrm{j}}\, \mathrm{x}(\mathrm{n}-\mathrm{j}) \tag{2.23}$$

2.3.3 Filtered-U LMS (FULMS) Algorithm

Despite its simplicity and efficiency, FXLMS lacks the ability to consider the interference between the control signal and the reference signal. To overcome this problem, FULMS can be used as an alternative solution [38]. FULMS algorithm is simply an extension of the FXLMS algorithm and it utilizes one or more previous outputs of the control filter to calculate the controller output. The block diagram of the FULMS algorithm is shown in Figure 2.6.

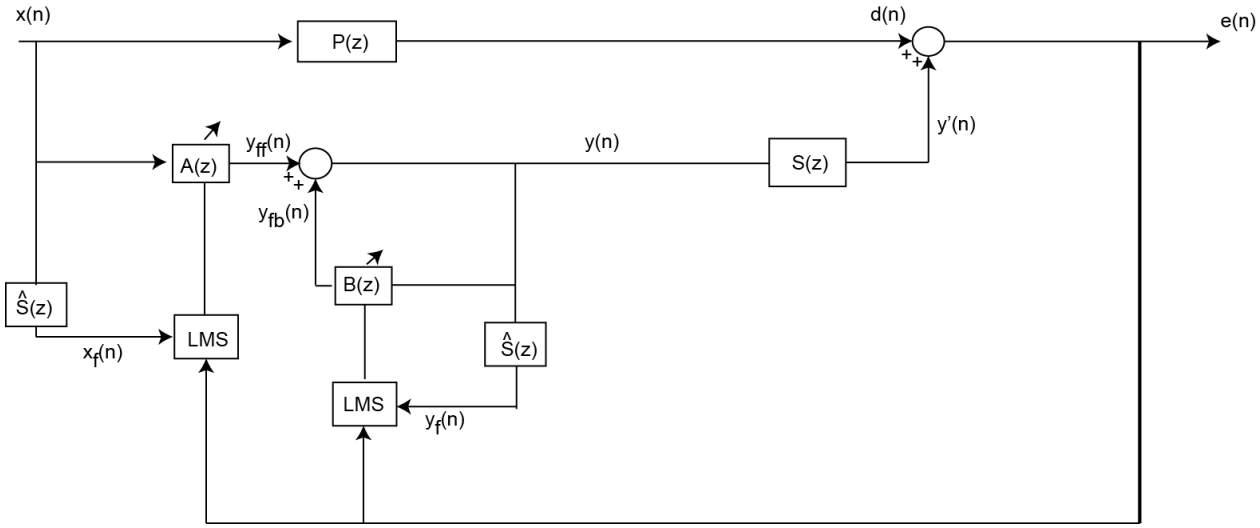

Figure 2. 6 Block diagram of the FULMS algorithm

In this configuration, control signal y(n) is superposition of the output, y_{ff} (n), which is feedforward part of IIR filter and the output, y_{fb}(n), which is the feedback part of the IIR adaptive filter. The feedforward part of the adaptive IIR filter is updated similar to the FXLMS algorithm as previously explained in Section 2.1. A(z) is the feedforward part of the IIR filter. **A**(n) is a (Mx1) vector of the filter weight coefficients and it can be written in the following form as:

$$\mathbf{A}(n) = [a_0(n)\ a_1(n) \dots a_{M-1}(n)]^T \tag{2.24}$$

The filter coefficients of the A(n) at every time step is updated as follows

$$\mathbf{A}(\mathrm{n}+1) = \mathbf{A}(\mathrm{n}) - 2\mu_{\mathrm{a}}\mathrm{e}(\mathrm{n})\mathbf{X_f}(\mathrm{n}) \tag{2.25}$$

where μ_a is the step size of the gradient descent algorithm for the feedforward part of the control filter. The $\mathbf{X_f}(\mathrm{n})$ is the filtered reference signal vector which is defined previously in section 2.1

On the other hand, the feedback part, **B**(z) is updated in a very similar way but with a slight difference. **B**(n) represents the (Lx1) vector of the filter weight coefficient for the feedback part of the controller and can be defined as

$$\mathbf{B}(\mathrm{n}) = [\mathrm{b}_0(\mathrm{n})\ \mathrm{b}_1(\mathrm{n})\ \ldots\ \mathrm{b}_{\mathrm{L}-1}(\mathrm{n})]^T \tag{2.26}$$

The filter coefficients of the B(n) at every time step is updated as follows,

$$\mathbf{B}(\mathrm{n}+1) = \mathbf{B}(\mathrm{n}) - 2\mu_{\mathrm{b}}\mathrm{e}(\mathrm{n})\mathbf{Y_f}(\mathrm{n}) \tag{2.27}$$

where μ_b is the step size of the gradient descent algorithm and $\mathbf{Y_f}(\mathrm{n})$ is the Lx1 filtered output vector of the controller with one step delay. The calculation of the $\mathbf{Y_f}(\mathrm{n})$ is similar to $\mathbf{X_f}(\mathrm{n})$ however, rather than the reference signal, the output signal of the controller for the previous time instant is filtered using the secondary path model,$\widehat{\boldsymbol{S}}(z)$.

The filtered output signal $\mathbf{Y_f}(\mathrm{n})$ includes the L most recent filtered output signal values and can be written as:

$$\mathbf{Y_f}(\mathrm{n}) = [\mathrm{y_f}(\mathrm{n})\ \mathrm{y_f}(\mathrm{n}-1)\ \ldots\ \mathrm{y_f}(\mathrm{n}-\mathrm{L}+1)]^{\mathrm{T}} \tag{2.28}$$

The elements of the vector $\mathbf{Y_f}(\mathrm{n})$ are calculated as follows

$$y_f(n) = \sum_{j=0}^{m-1} \hat{s}_j \, y(n-1-j) \tag{2.29}$$

2.4 Proposed Methodology with Online secondary path modeling

FXLMS and FULMS adaptive controller algorithms and the necessity of including secondary path models were explained in the sections 2.3.1 and 2.3.2. There are two basic approaches of secondary path modeling; online and offline modeling. Furthermore, in real applications, the dynamics of a plant might differ significantly from one operation condition to the other. Thus, online estimation of the secondary path modeling is a better alternative for better performance of the controller.

Addressing the online identification of the secondary path model during active control of vibration, a recent method proposed by Akhtar et.al. is suitable for its efficiency and simplicity [39, 40]. Since in this chapter, the results presented are obtained using the specified online modelling method, this section first presents the online modeling methodology and then presents the developed methodology based on the FULMS and the presented online secondary path modeling approach. The Figure 2.7 shows the block diagram of the online secondary path modelling developed by [39, 40]. Their algorithm is composed of two components. First one is the selected controller algorithm which is chosen as FXLMS originally and the second component is their secondary path modeling method. For the adaptation of the secondary path model and the FXLMS control filter, a modelling error signal $f(n)$ is defined as $f(n) = e(n) - v_f'(n)$ where $e(n)$ is the measured error signal and $v_f'(n)$ is the output of the estimated secondary path model. Then the filter coefficients of the FXLMS algorithm, $\mathbf{W}(n)$, at every time step is updated as follows

$$\mathbf{W}(n+1) = \mathbf{W}(n) - 2\mu_w f(n)\mathbf{X_f}(n) \tag{2.30}$$

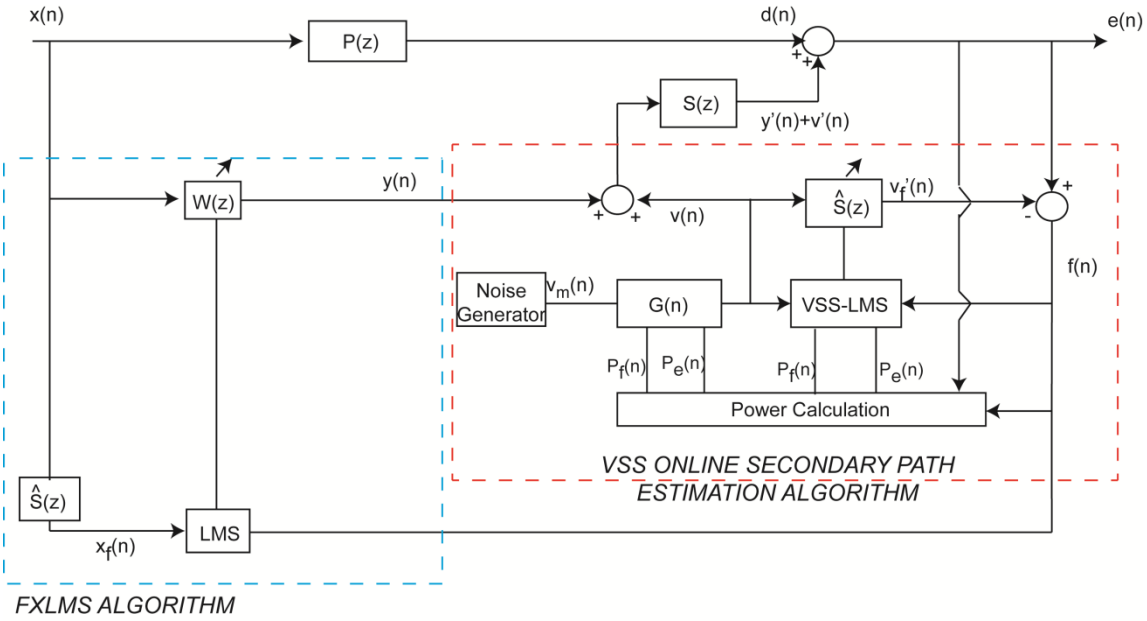

Figure 2. 7 Block diagram of FXLMS with online secondary path modeling (adapted from [39, 40])

In this chapter, the online secondary path modeling component of the aforementioned method is integrated with the IIR filtering based FULMS algorithm for an active vibration control problem. Figure 2.8 shows the proposed methodology for the adaptive active vibration control. The online secondary path modeling method utilizes Variable Step Size VSS and gain scheduling to enhance convergence of the secondary path modeling process and modify the level of the generated identification signal, $v_m(n)$. Implementation of the VSS and gain scheduling requires a defined power ratio $\rho(n)$ between power of the f(n), $P_f(n)$ and the power of the e(n), $P_e(n)$.

$$\rho(n) = P_f(n)/P_e(n) \tag{2.31}$$

Where

$$P_f(n) = \lambda P_f(n-1) + (1-\lambda)f(n)^2 \tag{2.32}$$

$$P_e(n) = \lambda P_e(n-1) + (1-\lambda)e(n)^2 \tag{2.33}$$

Here λ is the forgetting factor between 0.9 and 1. The initial conditions of the both $P_f(n)$ and $P_e(n)$ are chosen as 1.The identification signal $v_m(n)$ is modified using the gain scheduling parameter G(n) to generate the modified identification signal, v(n). The G(n) for each time step n is determined using, the min, $\sigma_{v_{min}}$ and max, $\sigma_{v_{max}}$, variances of the modified identification signal. Those limits are determined experimentally to calculate the gain scheduling parameter, G(n), in order to update the v(n) as follows:

$$G(n) = \sqrt{\big(1-\rho(n)\big)\sigma^2_{v_{min}} + \rho(n)\sigma^2_{v_{max}}} \tag{2.34}$$

$$v(n) = G(n).v_m(n) \tag{2.35}$$

In online secondary path modeling, the parameters of the secondary path model is time dependent and $\hat{\mathbf{S}}(n)$ is the vector of time varying finite impulse response modeling parameters. The adaptation equation of the $\hat{\mathbf{S}}(n)$ is as follows:

$$\hat{\mathbf{S}}(n+1) = \hat{\mathbf{S}}(n) + 2\mu_s(n)f(n)\mathbf{V}(n) \tag{2.36}$$

From Figure 2.8, it can be observed that the measured vibration level, e(n), can be written as e(n)=d(n)+$y'(n) + v'(n)$. Thus using the definition of f(n), f(n) becomes, f(n)=d(n)+$y'(n) + v'(n) - v'_f(n)$. When $\hat{\mathbf{S}}$ converges to **S,** $v'_f(n)$ converges to $v'(n)$ and the effect of the identification signal, v(n) on the measured vibration level is eliminated. The vector, **V**(n) contains most recent identification signal samples, such that **V**(n)=[v(n),v(n-1),…v(n-m+1)], where m is the order of the finite impulse response modeling filter $\hat{\mathbf{S}}(n)$. Online secondary path estimation method used in this study is a VSS

method which modifies the step size $\mu_s(n)$ based on the previously defined power ratio $\rho(n)$.

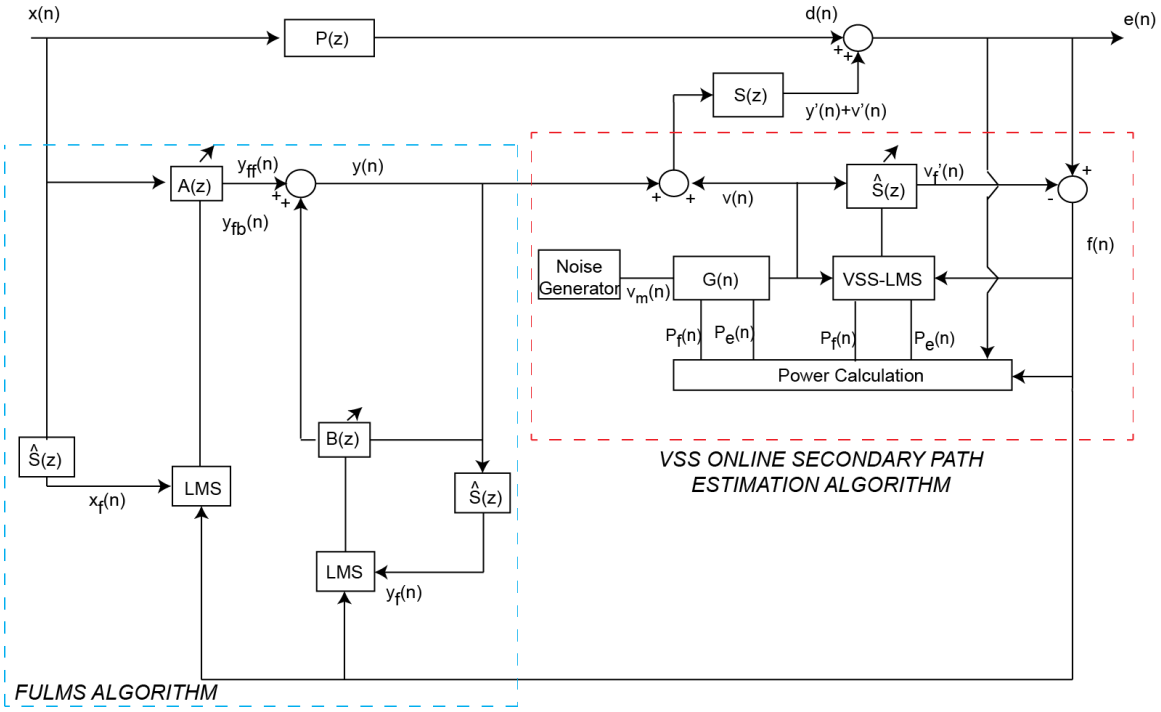

Figure 2. 8 Proposed FULMS method integrated with online secondary path modeling

The variable step size, $\mu_s(n)$ is updated as follows:

$$\mu_s(n) = \rho(n)\mu_{s_{min}} + (1 - \rho(n))\mu_{s_{max}} \tag{2.37}$$

Where $\mu_{s_{min}}$ and $\mu_{s_{max}}$ are the minimum and maximum values for the VSS which are identified experimentally. Finally, the coefficients of the control filter **A**(n) and **B**(n) are updated using the modeling error signal, f(n). The logic behind using the f(n) for the filter parameter update is that the measured error e(n) includes the additional effect of the identification signal, v(n) and the modeling filter error, f(n), eliminates effects of the additional noise on the filter parameter update as the $\hat{\mathbf{S}}$ converges to **S**. The filter coefficients of the **A**(n) and **B**(n) at every time step for FULMS is modified as follows:

$$\mathbf{A}(n+1) = \mathbf{A}(n) - 2\mu_a f(n)\mathbf{X_f}(n) \quad (2.38)$$

$$\mathbf{B}(n+1) = \mathbf{B}(n) - 2\mu_b f(n)\mathbf{Y_f}(n) \quad (2.39)$$

2.5 Experimental set-up

In this section the experimental set-up used for the demonstration of the developed methodology is presented.

2.5.1 System Architecture

The experimental set-up used to verify the proposed methodology is shown in Figure 2.9. The experimental set-up contains the vehicle panel, PZT sensors and actuators, a digital controller, signal generator, signal analyzer and a host PC. The panel is hanged to an aluminum frame to ensure free-free boundary conditions.

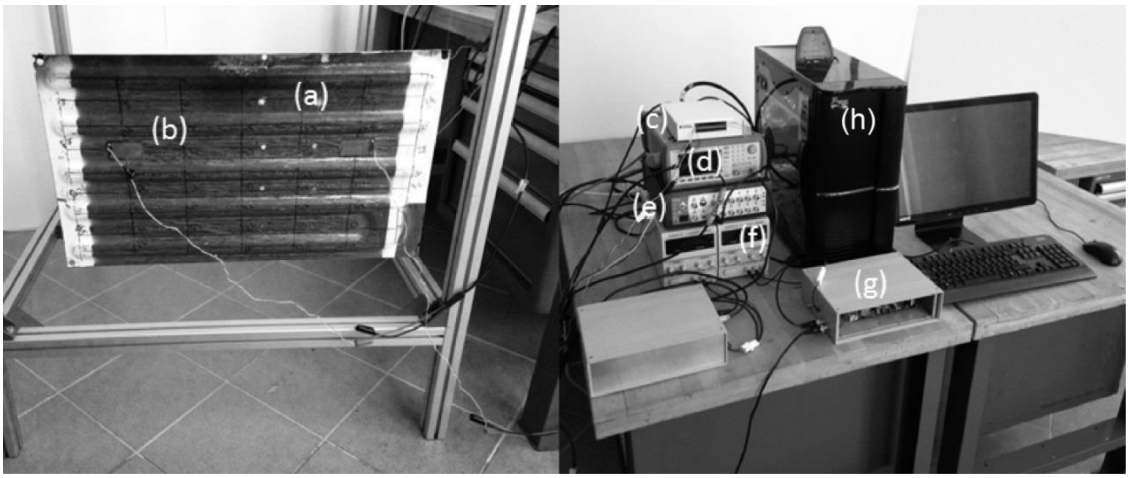

Figure 2. 9 Details of the experimental set-up a) Vehicle Panel b) PZT actuator c) Controller Connector Block d) Signal Generator e) Signal Analyzer f) DC Power Supply g) PZT amplifier h) Host PC

The panel is made of steel and has thickness of 1.2mm. The PI-p876.A12 type PZT patches are used as actuators and sensors. They are low weight high voltage actuators which can be implemented without altering the dynamic characteristics of the system. The

operating voltage of the actuators are between -100V to +400V. The operation voltage is obtained by amplifying the input signal by 50 using PI E413.D2 PZT amplifiers. The PZT sensors required no signal conditioning since the level of PZT sensor outputs are within the desired sensor signal range of ±10V. Properties of the vehicle panel and the PZT actuators are summarized in Table 2.1.

Table 2. 1 Properties of the vehicle panel and the PZT patch

Property	**Panel**	**PZT Patch**
Material	Steel	Lead-Zirconate-Titanate
Length (mm)	680	65
Width (mm)	400	31
Depth (mm)	1.2	0.5
Elastic Modulus (GPa)	200	70.2
Poisson's Ratio	0.3	0.36
Density (kg/m^3)	7300	7800
Weight (kg)	2.38	0.0028
Piezoelectric Strain Constant d_{31} (10^{-10} m/V)	-	1.74
Piezoelectric Strain Constant d_{33} (10^{-10} m/V)	-	3.94
Piezoelectric Strain Constant d_{51} (10^{-10} m/V)	-	5.35

2.5.2 Sensor/actuator placement

For vibration control, it is crucial to have control authority on the system for the targeted frequency range. The PZT actuators used in this study are strain type actuators. In order to use them efficiently, high strain regions should be identified for the targeted vibration modes[41]. For this purpose, a Finite Element Model (FEM) of the structure is generated using ABAQUS. Then, modal analysis is performed for the frequency range of

0-100 Hz. Results of the modal analysis in FEM is verified by the experimental modal analysis. The analysis showed that the structure has 4 modes between 0-100 Hz frequency range. The modal frequencies of the structure for the first four modes are listed in Table 2.2. The high strain regions for the first four modes of the structure are shown in Figure 2.10.

Table 2. 2 Modal frequencies of the host structure

	Mode 1	Mode 2	Mode 3	Mode 4
Experimental	20.1 Hz	33.2 Hz	54.6 Hz	86.7 Hz
FEM	20.5 Hz	33.4 Hz	54.9 Hz	86.3 Hz

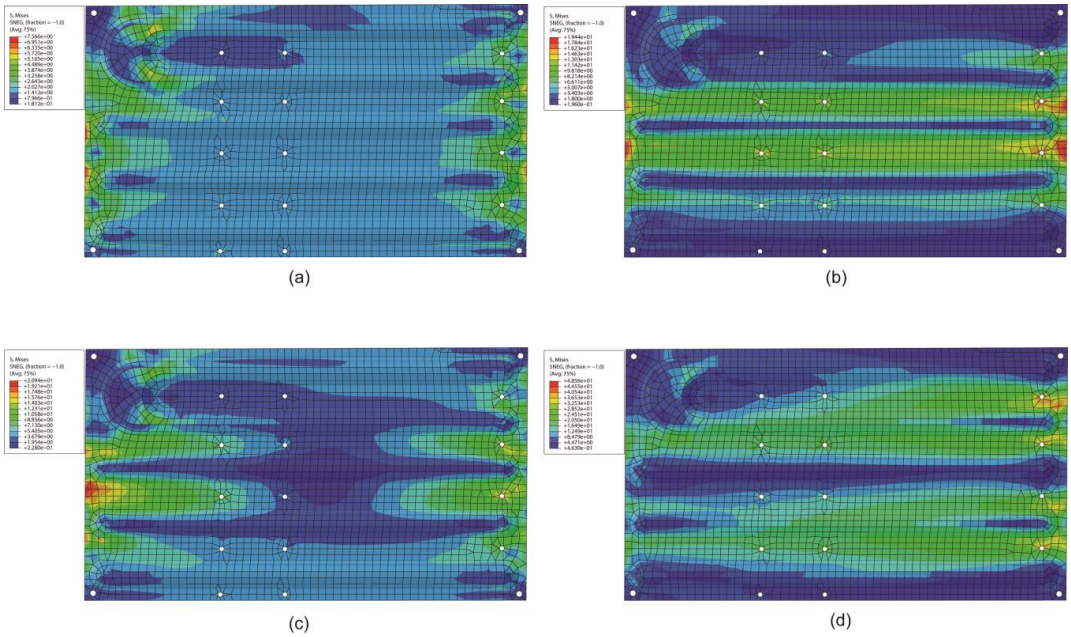

Figure 2. 10 High strain regions for the vibration modes between 0-100 Hz. a) First mode b) Second Mode c) Third Mode d) Fourth Mode

The second and third modes of the structure are targeted for the active vibration control. For this purpose, the sensor/actuator pairs are located on the structure as shown in Figure 2.11. The actuators are positioned 95 mm away from the left and right sides of the structure respectively. The strain distribution of the PZT actuator position suggests that the PZT actuators are capable of exciting the second and third modes effectively.

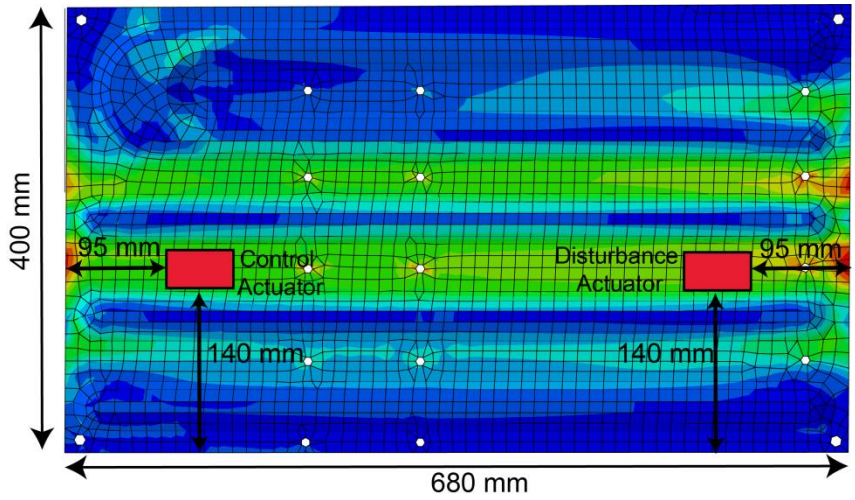

Figure 2. 11 PZT positions and dimensions of the vehicle panel for control applications

2.5.3 Modelling of the System

In order to generate accurate representation of the system, the models of the primary path P(z), and secondary path S(z) are generated. Both of the modelling procedures are accomplished in time domain using FIR filters and 750 parameters are used for the representation of the dynamics.

For the modelling of the primary path, P(z), a random signal with variance of 1 is generated and filtered to confine the signal within the bandwidth of the 0-100 Hz. By using output channel of the NI-PCI 6220 m-series DAQ unit, the generated signal is send to the amplifier E413.D2 to drive the disturbance actuator. Using a collocated PZT sensor with the disturbance actuator, the reference signal, x(n) is measured. Meanwhile, the error sensor, which is collocated with the control actuator is used to measure the e(n) and using

MATLAB/Simulink, LMS algorithm is implemented to extract the model of the P(z). Figure 2.12 shows the error level between the estimated output at the error sensor using the reference signal and the actual measured error signal.

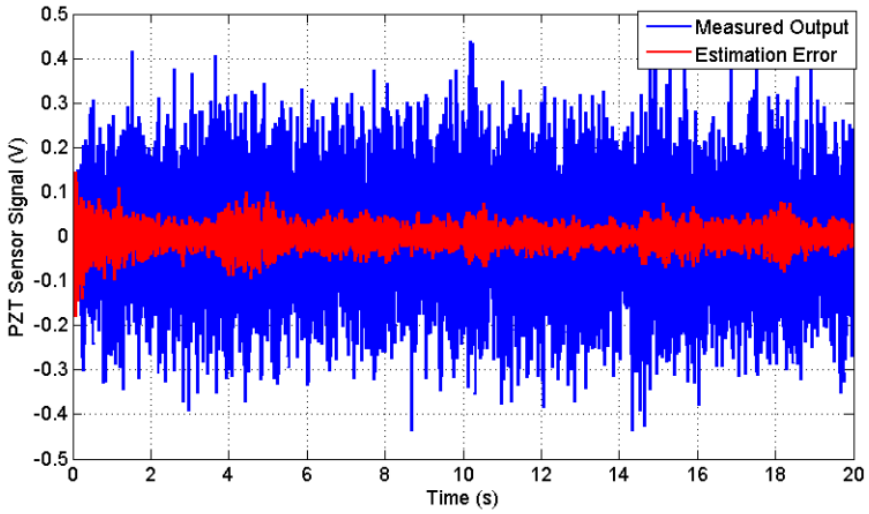

Figure 2. 12 Modeling of the P(z)

The LMS algorithm is also used for the derivation of the secondary path model, S(z). For the modelling of the S(z), again the NI-PCI 6229 is used to generate a random signal with the properties explained for deriving the P(z). However, this time the generated signal itself is used as the reference signal and the error sensor is used to measure the error signal e(n). Using MATLAB/Simulink, the LMS algorithm is implemented and the resultant filter parameters are used for further analysis. Figure 2.13 shows the actual output level of the error sensor measurement and the error between the estimated model output and the actual output.

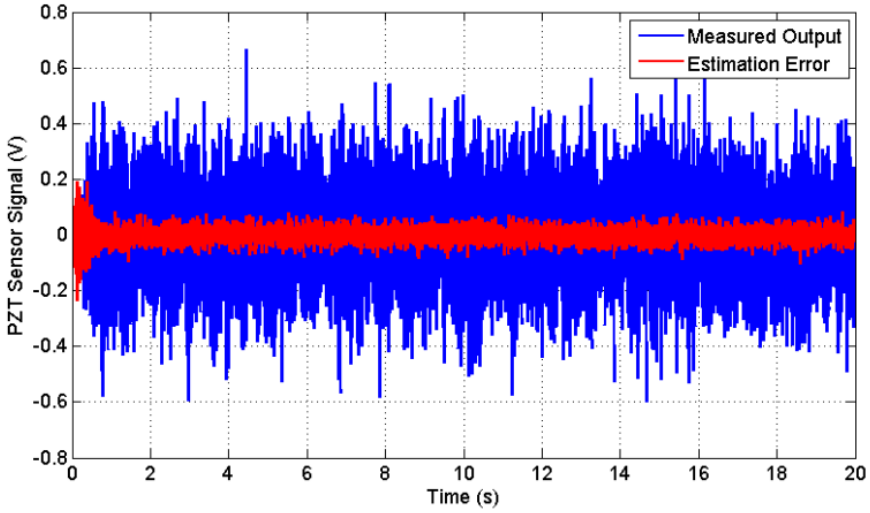

Figure 2. 13 Modeling of the S(z)

Figure 2.14 a-b shows the filter parameters obtained after the modeling procedure and the Figure 2.14 c-d shows the frequency responses of the modeling filters for primary and secondary paths respectively. Please note that the behavior of the modeling filters observed in frequency domain differs from the FRF measurements and this is due to nature of the FIR filters.

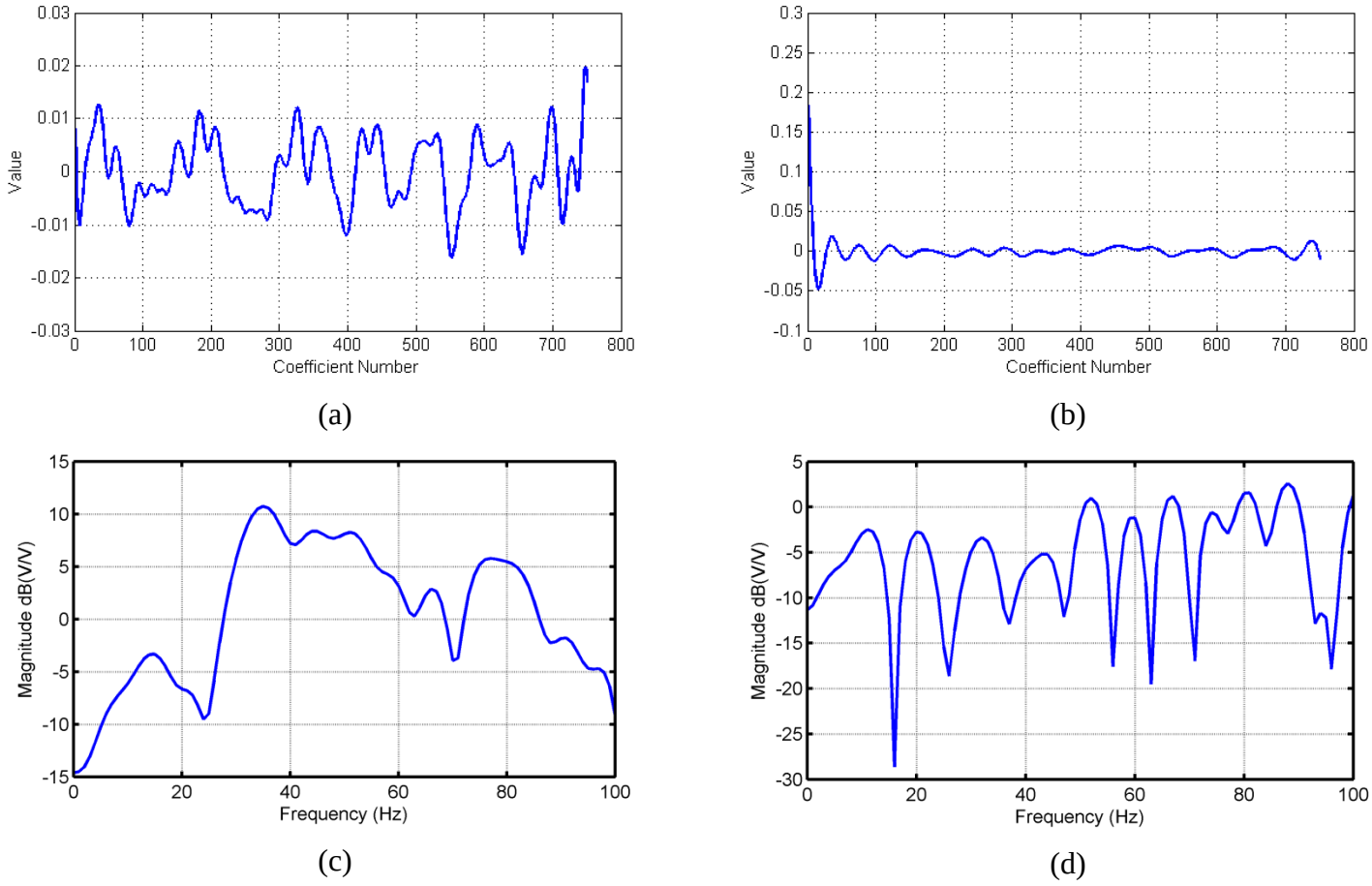

Figure 2. 14 Modeling Filter Parameters a) Primary Path P(z) b) Secondary Path S(z) c) Frequency response of the P(z) modeling filter d) Frequency response of the S(z) modeling filter

2.6 Controller implementation

The schematic of the controller is shown in Figure 2.15. The undesired vibration effects are generated using a signal generator and the disturbance actuator is used to generate undesired vibrations on the plate structure. The PZT actuators are high voltage actuators thus the generated signal is amplified using an E413.D2 type PZT amplifier. The reference sensor is placed on the structure in collocated configuration with the disturbance actuator. The control actuator is used to suppress vibration of the structure and the error

sensor is also collocated with the control actuator. NI-PCI 6229 m-series multifunction data acquisition (DAQ) unit is used to implement control algorithm. Using PCI interface of the host computer, NI-PCI 6229 can be programmed as an interface and host computer is used to implement control algorithm via NI-PCI 6229 DAQ unit. To monitor the vibration suppression performance of the controller a signal analyzer is used.

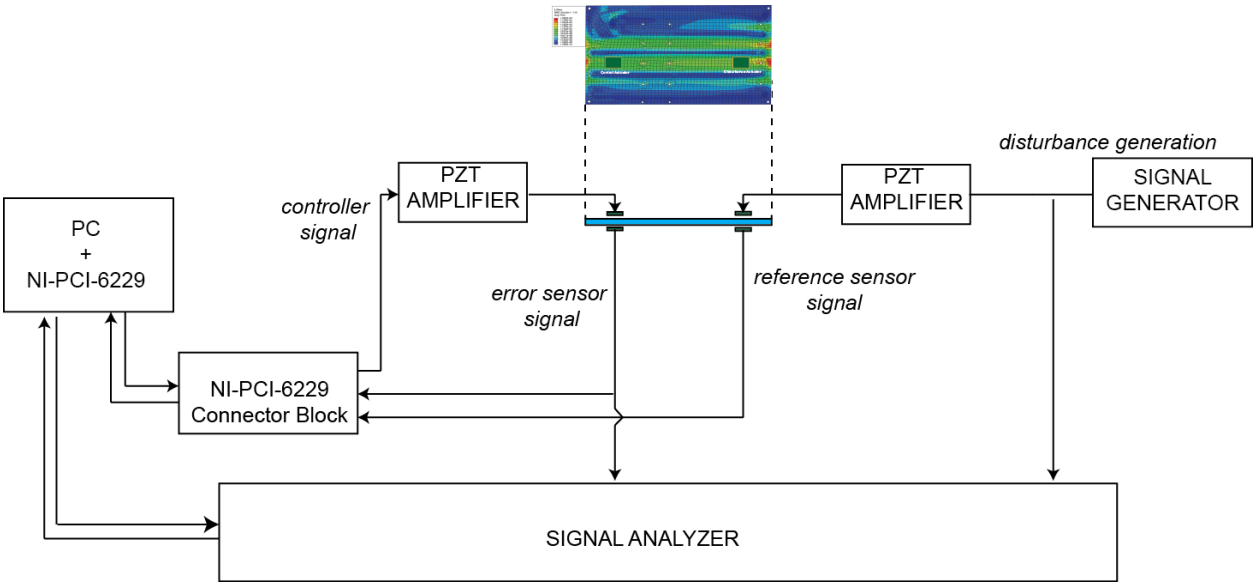

Figure 2. 15 Schematics of the controller configuration

2.7 Numerical and experimental results

In this section, numerical and experimental performance evaluations of the FXLMS and FULMS controllers with online secondary modeling are presented. Controller performances for the FXLMS and FULMS are evaluated for the second and third modes of the structure. Primary and secondary paths P(z) and S(z) are FIR filters with 750 parameters in both simulations and experiments. Performance of the controller is evaluated

for the sinusoidal reference signal with the variance of 0.5Vrms. The signal to noise ratio of the reference signal is adjusted to 30 dB. A Matlab/SIMULINK model is used for the numerical evaluations. The simulations and experiments are completed for two disturbance signals; one at 33.2 Hz and the other at 54.6 Hz which correspond to second and third modes of the structure, respectively.

Sampling frequency of the system is adjusted to 5000Hz in all of the performance evaluation cases. The controller used for the FXLMS algorithm is an FIR filter with 1500 filter parameters. The step size of the controller is 0.000001 in both simulation and experiments. The secondary path model is also an FIR filter with 750 filter parameters. The variables of the algorithm concerning secondary path modeling are as follows. The identification signal is a Gaussian white noise signal which has variance of 1Vrms. The maximum ${\sigma_{max}}^2$ and minimum ${\sigma_{min}}^2$ variances of the identification signals are adjusted to 0.03 and 0.002, respectively. The step size parameters of the modeling filter, $\mu_{s_{min}}$ and $\mu_{s_{max}}$, are adjusted to 0.00003 and 0.002. For the FULMS implementation, the secondary path estimation algorithm parameters are exactly the same with the FXLMS. The length of controller filter is adjusted to 750 parameters for both the feedforward and feedback paths. The step sizes of the adaptive algorithm for feedforward and feedback paths are tuned to 0.0000025 and 0.00000025, respectively in both simulations and experiments. The step sizes for the simulations are adjusted according to the experimental limitations observed during the controller implementation. Furthermore, all of the design variables are the same for the performance evaluation of the second and third mode.

In Figure 2.17, the controller performance for the second mode using FXLMS and FULMS with online secondary path modeling is presented. Figures 2.17 a-b and 2.17 c-d show the second mode performance of the simulated and experimental results of the FXLMS and FULMS algorithms, respectively. The controller is activated after 2 seconds of the signal initiation in both simulations and experiments. For better understanding the

behavior of the algorithms, mean square error of the system (MSE) for the controller online and offline configurations are calculated as follows:

$$MSE_{d(n)} = (\sum_{i=1}^{n} d(i)^2)/n \ , \ MSE_{e(n)} = (\sum_{i=1}^{n} e(i)^2)/n \quad (2.40a\text{-}b)$$

where *d(i)* and *e(i)* corresponds to the level of the vibration when the controller is offline and online, respectively.

Then the ratio between those two configurations, *R(n)* is calculated as:

$$R(n) = 10log_{10}(\frac{MSE_{e(n)}}{MSE_{d(n)}}) \quad (2.41)$$

The Figures 2.16 e-f show the change of *R(n)* as a function of iteration number in simulation and experiment for the second mode. As it can be observed from Figure 2.17, *R(n)* is always negative for both algorithms which indicates the suppression of vibration by the controller. From the figures, it is concluded that the FULMS converges faster than the FXLMS controller. Such behavior of the FULMS with respect to FXLMS controller is previously shown in the literature utilizing offline secondary path modeling technique [37]. The Figures 2.17 e-f shows that such properties of the FULMS are still valid in the case of online modeling. As it can be observed from the figures there is a slight difference between the simulation and experimental results due to the uncertainties of the experimental configuration settings.

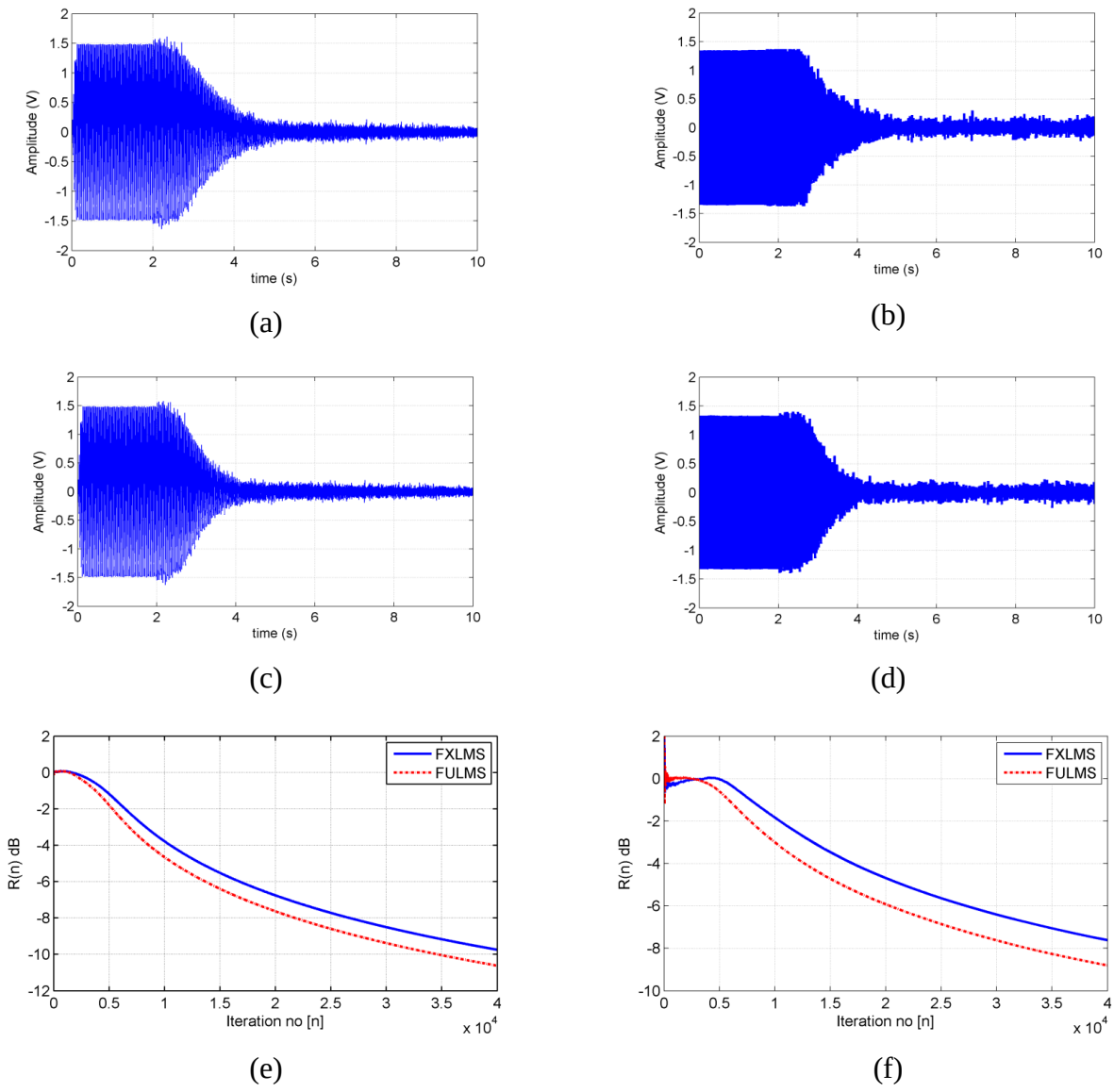

Figure 2. 16 Simulation results of the FXLMS and FULMS controller with online secondary path modeling for the second mode a) FXLMS performance in simulation b) FXLMS performance in experiment c) FULMS performance in simulation d) FULMS performance in experiment e) Mean Square Error of the system with respect to iteration number in simulation f) Mean Square Error of the system with respect to iteration number in experiment

.

For further analysis, the system is excited with the third mode frequency at 54.6 Hz. The controller performances for both of the algorithms are shown in Figure 2.17. Figures 2.17 a-b and 2.17c-d show the second mode performance of the simulated and experimental results of the FXLMS and FULMS algorithms, respectively. The Figures 2.17 e-f show the change of *R(n)* as a function of iteration number in simulation and experiment for the third mode. The FULMS controller also converges faster than the FXLMS in the case of third mode.

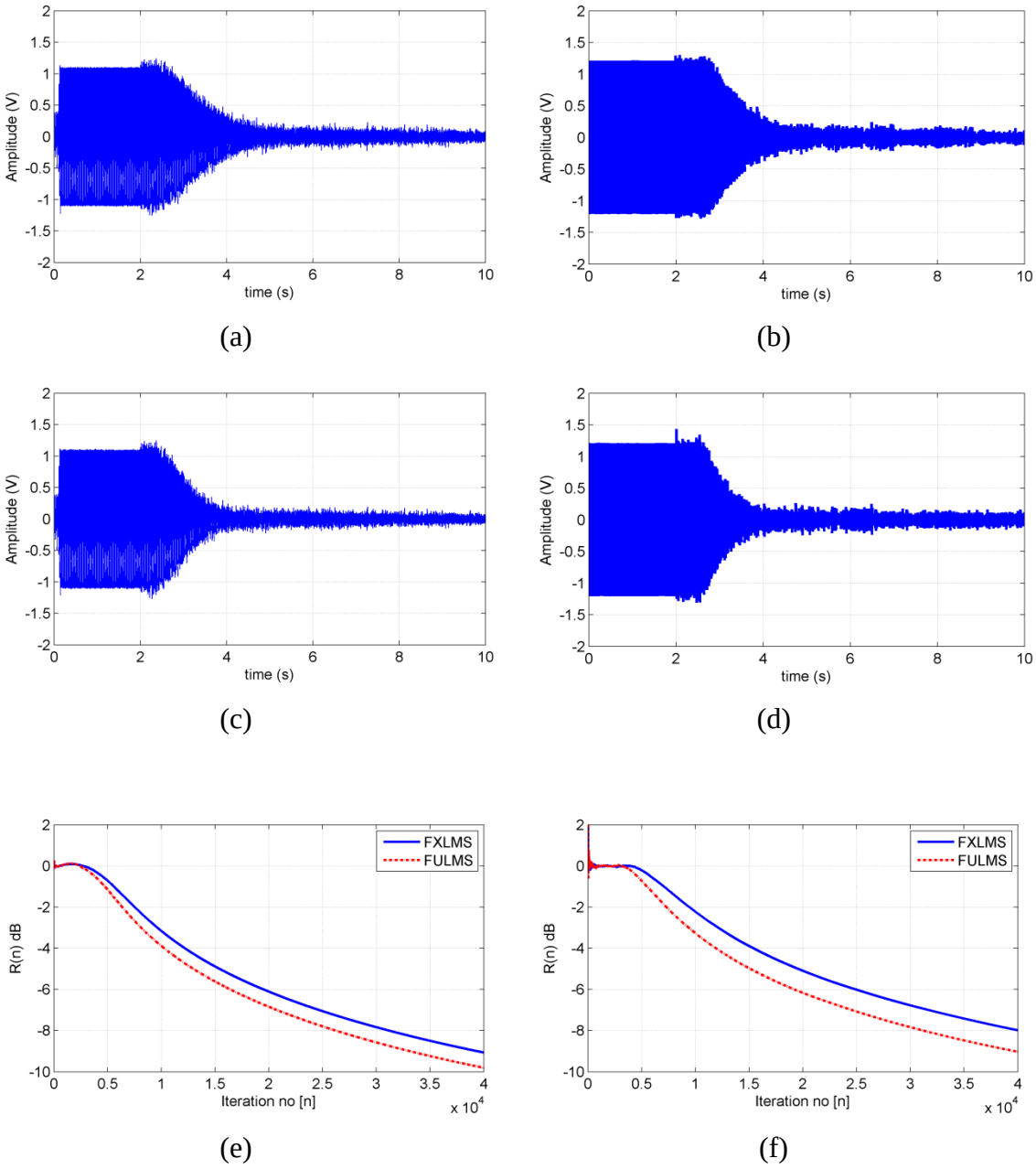

Figure 2. 17 Simulation results of the FXLMS and FULMS controller with online secondary path modeling for the third mode a) FXLMS performance in simulation b) FXLMS performance in experiment c) FULMS performance in simulation d) FULMS performance in experiment e) Mean Square Error of the system with respect to iteration number in simulation f) Mean Square Error of

the system with respect to iteration number in experiment

From the Figures 2.16 and 2.17, it can be also observed that the controller is not effective for the first 500 milliseconds because of the time required for the secondary path modeling filter parameters $\hat{\mathbf{S}}(z)$ to converge to the actual secondary path $\mathbf{S}(z)$. Initially, the secondary path modeling filter, $\hat{\mathbf{S}}(z)$ is a null vector, thus the filtered reference signal $\boldsymbol{X_f}(n)$ in both FXLMS and FULMS and the filtered controller output signal $\boldsymbol{Y_f}(n)$ in FULMS are 0. Thus, the controller requires time to generate the actual level of the filtered signals to be effective.

For periodic input type, it is clear that the FULMS controller with online secondary path modeling had a better performance in suppressing the vibration of the plate compared to the FXLMS controller with online path modeling. However, in real life applications, the input type is not always periodic. Thus, the broadband performance of the controller is also crucial. For this purpose, to evaluate the performance of the FULMS controller, system is excited using random noise including the frequency band of 0-100 Hz. The reference signal variance is adjusted to 0.5Vrms. The identification signal is a 0-100 Hz band-limited Gaussian white noise with variance of 1Vrms. The maximum ${\sigma_{max}}^2$ and minimum ${\sigma_{min}}^2$ variances of the identification signals are adjusted to 0.03 and 0.002, respectively. The number of parameters of the adaptive control filters and secondary path modeling filter are kept the same as the previous case study. However, the controller step sizes are adjusted to μ_w 0.0001, μ_d 0.00001 for FULMS controller and $\mu_{s_{min}}$ and $\mu_{s_{max}}$, are adjusted to 0.001 and 0.005 for secondary path estimation algorithm. The broadband vibration suppression performance of the FULMS controller is shown in Figure 2.18. The percent suppression levels at the modes are given in the Table 2.3. Please note that the first mode is not visible since the actuators and sensors are at the nodal point of that mode. In addition, the fourth

mode is also suppressed by 43% although the second and third modes of the structure are targeted in this study.

Table 2. 3 Vibration suppression levels for the broadband disturbance

	Mode 2	Mode 3	Mode 4
Suppression Level	74%	63%	43%

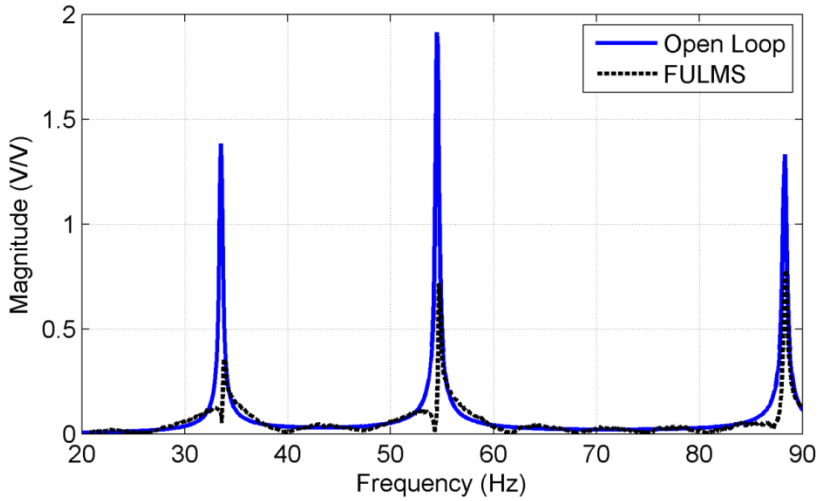

Figure 2. 18 Frequency response of the controllers in 0-100 Hz bandwidth

2.8 Conclusion

In this chapter, a method to combine the IIR filter based control algorithm with the online secondary path modeling technique for active vibration control of a plate-like structure is presented and discussed. For this purpose, IIR filter based FULMS algorithm is implemented utilizing online secondary path estimation method. The FULMS algorithm compensates for the control signal interference with the reference signal. The simulation and experimental performance of the FULMS controller with online secondary path

modeling is compared with the FXLMS counterpart. The results showed that FULMS with online secondary path modeling achieves better controller performance in terms of convergence speed and steady state error compared to the FXLMS counterpart. Results indicate that the FULMS is an effective alternative to the FXLMS in active vibration control applications.

Chapter 3

A TIME-FREQUENCY DOMAIN STEIGLITZ-MCBRIDE ADAPTIVE CONTROL ALGORITHM FOR ACTIVE VIBRATION SUPRESSION

3.1 Introduction

In this chapter, implementation of Steiglitz-McBride (SM) adaptive IIR filtering technique for active vibration control is demonstrated and enhanced computationally. For this purpose, in the first step, the experimental evaluation of the Steiglitz-McBride algorithm for active vibration controller is demonstrated. Later, the algorithm is computationally enhanced by developing a novel configuration (hybrid SM) which combines the frequency domain adaptive filtering methodology with originally proposed algorithm. Efficiency of the developed configuration is demonstrated both experimentally and numerically.

The controller configuration used in this chapter consists of a quarter body in white vehicle with PZT actuators bonded on the surface. The sensor signal is transferred using PCI interface of the host computer and the developed methodology is implemented via a rapid prototyping controller unit to generate the output for vibration suppression. A shaker is used stimulate the undesired vibrations. The low- frequency modes which are up to 220Hz of a structure explained in section 3.5.1 is used to demonstrate the efficiency of the approach. Furthermore a simulation configuration that mimics the controller configuration is used to demonstrate and predict the vibration suppression behavior before the experiments. The results are evaluated for both time and frequency domain using a random input type.

3.2 Literature Review.

.

In this chapter, a hybrid methodology is developed that integrates the frequency domain adaptive filtering approach with the classical SM algorithm. SM Algorithm includes the output error and the equation error formulations which was described in Section 2.2.2. Like all IIR filters, it has the possibility of the unstability. However, it almost always ensure the convergence of the filter parameters to optimal values. The classic SM method is originally proposed by Steiglitz and McBride[42]. The SM algorithm formulation requires extra all-pole filtering of the reference and desired signals. The approach guarantees the near-optimal solution for the filter parameters when the signal to noise ratio is high and the measurement noise is not colored [43]. The SM for noise and vibration control is first proposed by Sun and Meng [44]. In their work, they demonstrated efficiency of the SM algorithm for different test cases based on system models available in [45] and [46]. It is shown that the SM type algorithm ensures global convergence to the optimal parameters and it has robustness against the measurement noise and/or the insufficient filter order selection [44]. There are also other forms of the IIR filtering like lattice forms for vibration control as well. However those are beyond the scope of this thesis. For further information please refer to [23].

The adaptive algorithms are generally implemented in time domain. On the other hand it is possible to implement those algorithms in frequency domain as well. In frequency domain approach, the Fourier Transform is used before the algorithm implementation. One benefit of the frequency domain approach is the reduction of the computational complexity by employing the block updating stage where the Fast Fourier Transform (FFT) implementation is usable [23]. On the other hand, during the block processing, FFT approach may yield a delay in the adaptation since update of the filter output and the new weight coefficients are calculated after accumulating one block of data. To address this issue, one efficient alternative is to implement the controller filter

continuously in time domain while updating parameters of the controller filter in the frequency domain [23]. In the past, some noise and vibration control studies have been performed using frequency domain approach. In a recent study, Tang and Lee proposed a methodology for noise control using a time-frequency domain filtered-x LMS (FXLMS) algorithm [47]. They demonstrated that, with a new time-frequency domain approach, it is possible to increase the convergence speed and decrease the computational complexity. They demonstrated the success of their method by comparing it to the time domain FXLMS algorithm for active noise control of a representative system. Moreover, Das et al. [48] developed a frequency domain FXLMS methodology for a virtual microphone. They presented that their method is equivalent to the performance of the time domain counterpart while providing computational advantage.

The frequency domain approach is possible to implement for both FIR and IIR filters [49]. The IIR filtering in frequency domain is first proposed by Shynk and Goch [50]. Later, Fan and Yang [51] analyzed the Frequency-Domain approach adopted by Shynk and Goch. Fan and Yang concluded that there are many equivalent parameter sets of global minimum and the algorithm converges to one of these sets. Nowak and Veen [52] used adaptive IIR filtering in frequency domain for active noise control and concluded that the algorithm is advantageous with its filter adaptation capability when input signal is constrained.

3.3 Steiglitz-McBride Algorithm and AVC Implementation

In this section, the form of SM algorithm for AVC is presented. The main advantage of the classical SM approach is that it combines equation error and output error formulations for IIR filtering. Although it is based on equation error formulation, the extra all pole filtering property of the SM algorithm modifies its behavior to include features of the output error formulation. Thus, the optimal parameter adaptation is unbiased and the

convergence of those parameters is always near to the global optimum. The classic Steiglitz-McBride algorithm developed for noise and vibration control is shown in Figure 3.1.

In Figure 3.1, $\boldsymbol{A}(z)$ and $\boldsymbol{B}(z)$ are the forward and feedback loops of the IIR filter with N_f and N_b weight coefficients respectively. $y(n)$ is the controller signal and the $u(n)$ is the effect of the controller on the structure. $\boldsymbol{P}(z)$ is the primary path which represents the dynamics between the reference signal and the generated disturbance on controlled structure. The, $\widehat{\boldsymbol{S}}(z)$ is the secondary path model. The signals $pf_{x_f}(n)$ and $pf_{d'}(n)$ are the prefiltered signals of the filtered reference $x_f(n)$, and the estimated disturbance, $d'(n)$ by $\boldsymbol{B}(z)$ respectively.

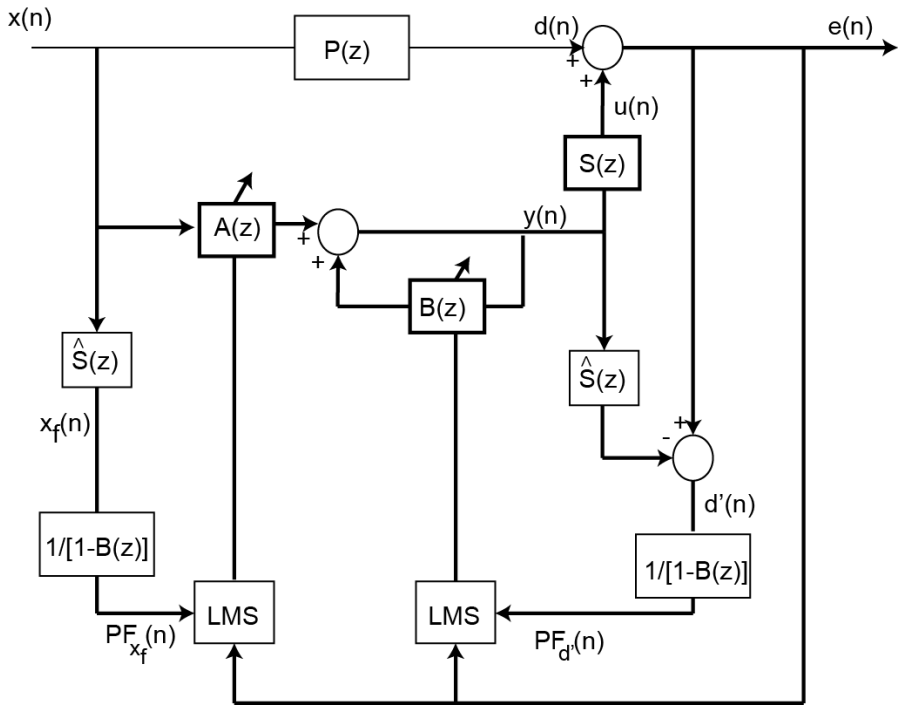

Figure 3. 1 Block diagram of the classic SM for noise and vibration control

As previously explained the additional dynamics due to presence of the controller must be included in the control algorithm to avoid unstability. Thus, the effect of the $\boldsymbol{S}(z)$ is included in the control algorithm by filtering the reference signal $x(n)$ via the M order finite impulse response vector $\widehat{\boldsymbol{S}}$ such that $\widehat{\boldsymbol{S}}$=[$\hat{S}_0$ ... $\hat{S}_{M-1}$], as indicated in Equation.(3.1).

$$x_f(n) = \sum_{i=0}^{M-1} \hat{S}_i x(n-i) \tag{3.1}$$

Furthermore, the $d'(n)$ is the estimated disturbance level of the system. Since in mechanical systems the measured error, $e(n)$ is the superposition of the disturbance and the controller output, $e(n) = d(n) + u(n)$, using the model of the controller dynamics $\widehat{\boldsymbol{S}}(z)$ and $e(n)$, $d'(n)$ can be estimated using Eq..(3.2)

$$d'(n) = \mathrm{e(n)} - \sum_{i=0}^{M-1} \hat{S}_i y(n-i) \tag{3.2}$$

the SM formulation aims to minimize the $E\{e'(n)^2\}$ instead of $E\{e(n)^2\}$ where the $e'(n)$ is

$$e'(n) = pf_{d'}(n) - \sum_{i=1}^{N_b} b_i(n) pf_{d'}(n-i) + \sum_{j=0}^{N_f} a_j(n) pf_{x_f}(n-j) \tag{3.3}$$

The $pf_{d'}(n)$ and $pf_{x_f}(n)$ are given in Equation (3.4a-b)

$$pf_{d'}(n) = d'(n) + \sum_{i=1}^{N_b} b_i(n) pf_{d'}(n-i)$$

$$pf_{x_f}(n) = x_f(n) + \sum_{i=1}^{N_b} b_i(n) x_f(n-i) \tag{3.4a-b}$$

To minimize $\{e'(n)^2\}$, using Equation (3.3) and the gradients $\frac{d(e'(n)^2)}{d(A)}$ and $\frac{d(e'(n)^2)}{d(B)}$ the weight coefficient vectors $\boldsymbol{A}(n)$ and $\boldsymbol{B}(n)$ corresponding to the $\boldsymbol{A}(z)$ and $\boldsymbol{B}(z)$ at time instant n are updated using Equation (3.5a-b)

$$\boldsymbol{B}(n+1) = \boldsymbol{B}(n) + 2\mu e'(n)\boldsymbol{PF}_{\boldsymbol{d'}}(n) \quad \text{(3.5a-b)}$$
$$\boldsymbol{A}(n+1) = \boldsymbol{A}(n) - 2\mu e'(n)\boldsymbol{PF}_{\boldsymbol{x_f}}(n)$$

Here $\boldsymbol{PF}_{\boldsymbol{x_f}}(n)$ and $\boldsymbol{PF}_{\boldsymbol{d'}}(n)$ includes N_f and N_b most recent values of $pf_{x_f}(n)$ and $pf_{d'}(n)$ respectively such as

$$\boldsymbol{PF}_{\boldsymbol{x_f}}(n) = \left[pf_{x_f}(n) \ldots pf_{x_f}(n - N_f + 1)\right] \quad \text{(3.6a-b)}$$
$$\boldsymbol{PF}_{\boldsymbol{d'}}(n) = [pf_{d'}(n-1) \ldots pf_{d'}(n - N_b)]$$

In Equations (3.6a-b) instead of $e'(n)$ for the sake of computational efficiency, e(n) can be used [23] and the parameter update equations of the $\boldsymbol{B}(n)$ and $\boldsymbol{A}(n)$ becomes

$$\boldsymbol{B}(n+1) = \boldsymbol{B}(n) + 2\mu e(n)\boldsymbol{PF}_{\boldsymbol{d'}}(n) \quad \text{(3.7a-b)}$$
$$\boldsymbol{A}(n+1) = \boldsymbol{A}(n) - 2\mu e(n)\boldsymbol{PF}_{\boldsymbol{x_f}}(n)$$

3.4 IIR Filtering in Frequency Domain

In this section, Frequency domain adaptive filtering approach for IIR filters is explained. The frequency domain adaptive filtering (FDAF) has advantages over the time domain adaptive approaches such as the computational efficiency and the approximately uncorrelated (orthogonal) signals generated by the Fourier Transform[49]. However, since the FDAF results in a delay due to accumulation of the signal values for one block of data, in adaptive control such implementation may deteriorate system performance [53]. Hence, in such applications, the FDAF may be reformulated in a way to perform filtering in time domain while the adaptation procedure is completed in frequency domain [53].

Figure 3.2 shows the block diagram of the frequency domain (FD) IIR filtering based on equation error formulation. Block sizes of N are assumed for both forward and feedback loops of the IIR filter. The overlap-save method is used to avoid circular convolution [49].

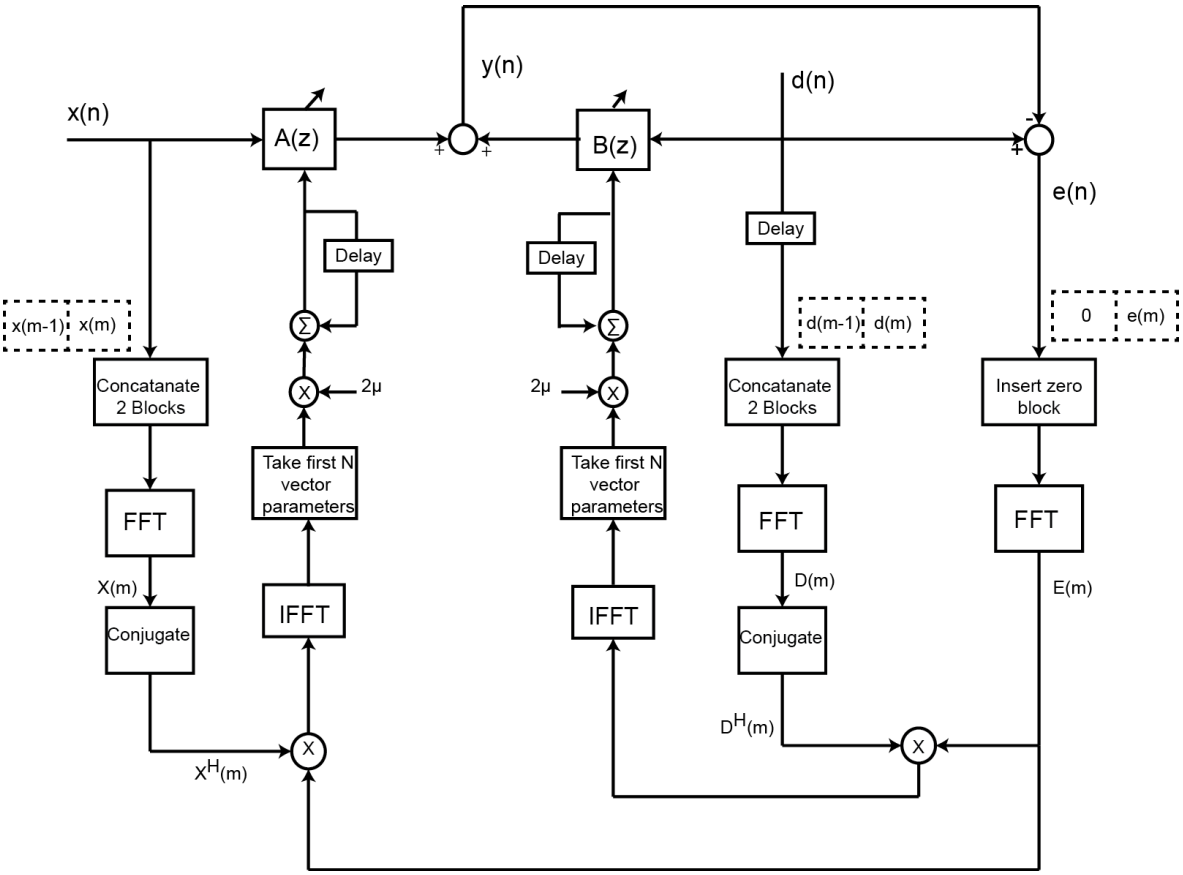

Figure 3. 2 FD IIR filtering configuration for equation error form

Here, the update of the error signal, $e(n)$ is in time domain and can be formulated as

$$e(n) = d(n) - \sum_{i=0}^{N-1} a_i\, x(n-i) - \sum_{i=1}^{N} b_i\, y(n-i) \tag{3.8}$$

Here b_i and a_i are the coefficients of the filter weights for $\boldsymbol{B}(z)$and $\boldsymbol{A}(z)$ in time instant n such as $\boldsymbol{A}(n) = [a_0(n)\ a_1(n) \ldots\ a_{N-1}(n)\ ]$ and $\boldsymbol{B}(n) = [b_1(n)\ b_2(n) \ldots\ b_N(n)\ ]$. The update equation for the adaptive filters $\boldsymbol{A}(m)$ and $\boldsymbol{B}(m)$ are written as

$$\boldsymbol{A}(m+1) = \boldsymbol{A}(m) + 2\mu.\,\mathrm{IFFT}\{\mathbf{X^H}(\mathrm{m})\mathbf{E}(\mathrm{m})\}_{\mathrm{N}} \quad (3.9a\text{-}b)$$
$$\boldsymbol{B}(m+1) = \boldsymbol{B}(m) + 2\mu.\,\mathrm{IFFT}\{\mathbf{D^H}(\mathrm{m})\mathbf{E}(\mathrm{m})\}_{N}$$

Here $\boldsymbol{B}(m)$ and $\boldsymbol{A}(m)$ are the filter weights for block index m where time index n for each block index m is $n = mN.\ \mu$ is the step size for parameter adaptation. IFFT is Inverse Fast Fourier Transform, $\{.\}_N$ indicates the causality gradient constraint which exerts first N parameters after IFFT operation, $\mathbf{X^H}(m)$ and $\mathbf{D^H}(m)$ are the complex conjugate of the vectors $\mathbf{X}(m)$ and $\mathbf{D}(m)$ in frequency domain. $\mathbf{X}(m), \mathbf{D}(m)$ and $\mathbf{E}(m)$ are the vectors of size 2N in frequency domain such as

$$\mathbf{X}(\mathrm{m}) = \mathrm{FFT}\{[\boldsymbol{x}(m-1)\ \boldsymbol{x}(m)]\} \quad (3.10a\text{-}c)$$
$$\mathbf{D}(\mathrm{m}) = \mathrm{FFT}\{[\boldsymbol{d}(m-1)\ \boldsymbol{d}(m)]\}$$
$$\mathbf{E}(\mathrm{m}) = \mathrm{FFT}\{[\mathbf{0}_N\ \boldsymbol{e}(m)]\}$$

$\boldsymbol{x}(m), \boldsymbol{d}(m)$ and $\boldsymbol{e}(m)$ are the vectors containing last N past and present signal values for $x(n), d(n)$ and $e(n)$ in the form of

$$\boldsymbol{x}(m) = [x(mN), x(mN+1) \ldots x(mN+N-1)] \quad (3.11a\text{-}c)$$
$$\boldsymbol{d}(m) = [d(mN+1), x(mN) \ldots x(mN+N)]$$
$$\boldsymbol{e}(m) = [e(mN), e(mN+1) \ldots e(mN+N-1)]$$

3.5 Hybrid Approach for Active Vibration Control

The hybrid adaptive control approach developed is presented in this section. The main idea of the algorithm proposed is to combine the SM algorithm explained in section 3.2 with the frequency domain (FD) IIR algorithm explained in section 3.3. The block diagram of the proposed algorithm is shown in Figure 3.3.

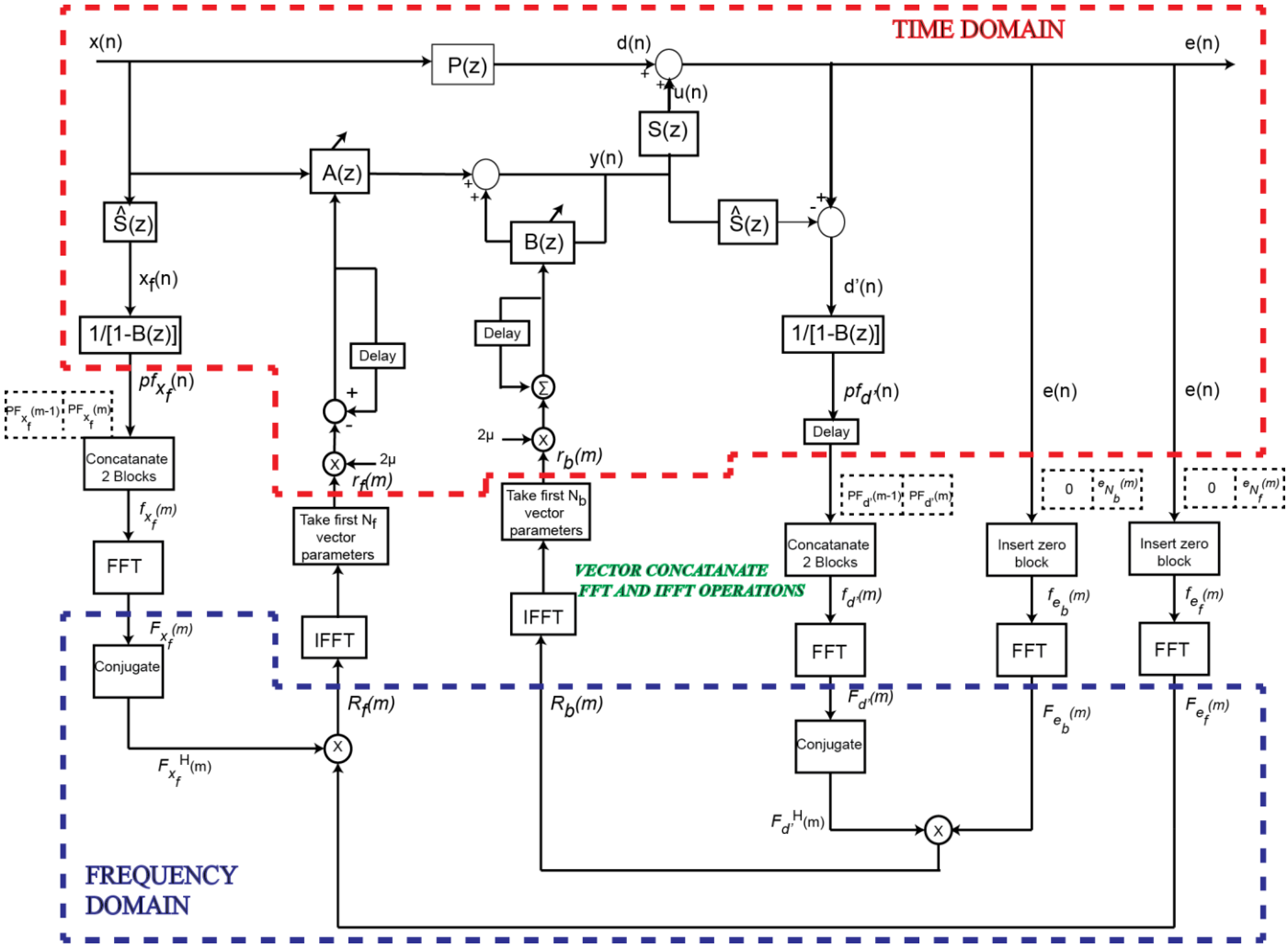

Figure 3. 3 Block diagram of the proposed algorithm

Here the $x(n)$ is the reference signal, *d(n)* is the disturbance generated on the system, *e(n)* is the measured error signal, $\boldsymbol{S}(z)$ and $\boldsymbol{P}(z)$ are secondary path and primary path

respectively. $\widehat{\boldsymbol{S}}$ is the model of the secondary path and x_f(n), pf_{x_f}(n) and $pf_{d'}(n)$ are the same variables described in section 3.2.

For FD update of the IIR filter weights, the overlap-save method is used to avoid the circular convolution [49]. To apply the Frequency domain update of the IIR filter parameters, the prefiltered signals pf_{x_f}(n) and $pf_{d'}(n)$, and error signal $e(n)$ are formed into vectors such that

$$\begin{aligned} \boldsymbol{f}_{\boldsymbol{x_f}}(m) &= \left[\boldsymbol{PF}_{\boldsymbol{x_f}}(m-1)\ \ \boldsymbol{PF}_{\boldsymbol{x_f}}(m)\right] \\ \boldsymbol{f}_{\boldsymbol{d'}}(m) &= [\boldsymbol{PF}_{\boldsymbol{d'}}(m-1)\ \ \boldsymbol{PF}_{\boldsymbol{d'}}(m)] \\ \boldsymbol{f}_{\boldsymbol{e_b}}(m) &= \left[\boldsymbol{0}_{\boldsymbol{N_b}}\ \ \boldsymbol{e}_{\boldsymbol{N_b}}(m)\right] \\ \boldsymbol{f}_{\boldsymbol{e_f}}(m) &= \left[\boldsymbol{0}_{\boldsymbol{N_f}}\ \boldsymbol{e}_{\boldsymbol{N_f}}(m)\right] \end{aligned} \tag{3.12a-d}$$

In eqns.(13a-d) the $PF_{x_f}(m), PF_{d'}(m)$, $e_{N_b}(m)$ and $e_{N_f}(m)$ are the vectors containing last N past and present signal values for $pf_{x_f}(n), pf_{d'}(n)$ and $e(n)$ in the form of

$$\begin{aligned} \boldsymbol{PF}_{\boldsymbol{x_f}}(m) &= \left[pf_{x_f}(mN_f), pf_{x_f}(mN_f+1) \ldots pf_{x_f}(mN_f+N_f-1)\right] \\ \boldsymbol{PF}_{\boldsymbol{d'}}(m) &= [d(mN_b+1), x(mN_b) \ldots x(mN_b+N_b)] \\ \boldsymbol{e}_{\boldsymbol{N_b}}(m) &= [e(mN_b), e(mN_b+1) \ldots e(mN_b+N_b-1)] \\ \boldsymbol{e}_{\boldsymbol{N_f}}(m) &= [e(mN_b), e(mN_b+1) \ldots e(mN_b+N_b-1)] \end{aligned} \tag{3.13a-d}$$

In Equations.(3.13a-d) vectors $\boldsymbol{f}_{\boldsymbol{x_f}}$ and the $\boldsymbol{f}_{\boldsymbol{e_f}}$ are used for updating the filter parameters for the forward loop $\boldsymbol{A}(z)$ of the IIR filter while $\boldsymbol{f}_{\boldsymbol{d'}}$and $\boldsymbol{f}_{\boldsymbol{e_b}}$ are used for updating the feedback weight coefficients $\boldsymbol{B}(z)$. Sizes of the vectors for the filter weight update are adjusted to $2N_f$ and $2N_b$ for the update of the $\boldsymbol{A}(z)$ and $\boldsymbol{B}(z)$. Here m is the block index introduced in section 3.3 and each block has N_f and N_b parameters according to the part of

the filter they are used for updating. After constructing vectors, FFT for their respective size is applied to convert the time domain vectors to the frequency domain.

$$\mathbf{F_{x_f}}(\mathrm{m}) = \mathrm{FFT}_{2\mathrm{N_f}}\left\{\boldsymbol{f}_{x_f}(m)\right\} \quad (3.14a\text{-}d)$$

$$\mathbf{F_{e_f}}(\mathrm{m}) = \mathrm{FFT}_{2\mathrm{N_f}}\left\{\boldsymbol{f}_{e_f}(m)\right\}$$

$$\mathbf{F_{d'}}(\mathrm{m}) = \mathrm{FFT}_{2\mathrm{N_b}}\{\boldsymbol{f}_{d'}(m)\}$$

$$\mathbf{F_{e_b}}(\mathrm{m}) = \mathrm{FFT}_{2\mathrm{N_b}}\{\boldsymbol{f}_{e_b}(m)\}$$

The change in the filter weight coefficients for the forward and feedback loops of the IIR filter in frequency domain can be calculated as

$$\mathbf{R_f}(\mathrm{m}) = \mathbf{F_{x_f}}^{\mathbf{H}}(\mathrm{m}).\mathbf{F_{e_f}}(\mathrm{m}) \quad (3.15a\text{-}b)$$

$$\mathbf{R_b}(\mathrm{m}) = \mathbf{F_{d'}}^{\mathbf{H}}(\mathrm{m}).\mathbf{F_{e_b}}(\mathrm{m})$$

Here operator H stands for the complex conjugate operation on any vector. Taking IFFT of the $\mathbf{R_f}(\mathrm{m})$ and $\mathbf{R_b}(\mathrm{m})$ and extracting first N_f and N_b parameters yield the change in parameters of the IIR filter in time domain such that

$$\boldsymbol{r_f}(m) = \mathrm{IFFT}\{\mathbf{R_f}(\mathrm{m})\}_{N_f} \quad (3.16a\text{-}b)$$

$$\boldsymbol{r_b}(m) = \mathrm{IFFT}\{\mathbf{R_b}(\mathrm{m})\}_{N_b}$$

Thus, the parameters of the IIR filter are updated using

$$\boldsymbol{A}(m+1) = \boldsymbol{A}(m) - 2\mu\boldsymbol{r_f}(m) \quad (3.17a\text{-}b)$$

$$\boldsymbol{B}(m+1) = \boldsymbol{B}(m) + 2\mu\boldsymbol{r_b}(m)$$

Please note that, in the proposed configuration, calculation of the $x_f(\mathrm{n})$, $pf_{x_f}(\mathrm{n})$ and $pf_{d'}(n)$ is completed in time domain while filter weight coefficients are updated in FD.

Such configuration is preferred to avoid the possibility of introducing delay by block processing when the $\widehat{\boldsymbol{S}}$, $\boldsymbol{A}(z)$ and $\boldsymbol{B}(z)$ have different number of parameters.

The computational complexity of the proposed hybrid controller is also compared to the time domain SM algorithm. The Table 3.1 shows the number of the multiplications required by both of the algorithms due to significance of those operations in computational complexity. The FFT and IFFT operations are considered as $2L\log_2 2L$ real multiplications for block with length of $2L$ [23]. Furthermore, 8L real multiplications are required for complex multiplication of a block with length of 2L. In our method the filtering of the reference signal $x(n)$ requires M multiplications as well as the calculation of the $d'(n)$. The prefiltering of the $x_f(n)$ and $d'(n)$ require $2N_b$ multiplications in total. Up to now, the SM and the proposed hybrid form use the same number of parameter evaluation. After prefiltering, SM algorithm requires multiplication of PF_{x_f}(n) and $PF_{d'}(n)$ vectors with $e(n)$ and μ yielding $N_f + N_b + 2$ multiplication for each sampling period for parameter update of $\boldsymbol{A}(z)$ and $\boldsymbol{B}(z)$. On the other hand, the proposed method requires 4 FFT and 2 IFFT operations and 2 complex multiplication for calculation of $\boldsymbol{r_f}(m)$ and $\boldsymbol{r_b}(m)$. This procedure yields $6N_f \log_2 2N_f + 8N_f$ real multiplications for updating $\boldsymbol{A}(z)$ and $6N_b \log_2 2N_b + 8N_b$ multiplications for updating $\boldsymbol{B}(z)$. After conversion to time domain, multiplication with the step size, μ requires N_f and N_b additional real multiplication for parameter update after exerting the first N_f and N_b parameters of the $\boldsymbol{r_f}(m)$ and $\boldsymbol{r_b}(m)$. In our approach, this procedure takes place after each data block for index m is accumulated.

Table 3. 1 Computational complexity analysis of the SM and proposed Hybrid algorithm

Algorithm	Eqn	×
SM	(1)	M
	(2)	M
	$(4a-b)$	$2N_b$
	$(7a-b)$	N_b+N_f+2
	$Total$	$F_s(2M+N_f+3N_b+2)$
Hybrid SM	(1)	M
	(2)	M
	$(4a-b)$	$2N_b$
	$(14a-d)$	$\left(4N_f\log_2 2N_f\right)+(4N_b\log_2 2N_b)$
	$(15a-b)$	$8N_f+8N_b$
	$(16a-b)$	$\left(2N_f\log_2 2N_f\right)+(2N_b\log_2 2N_b)$
	$(17a-b)$	N_f+N_b
	$Total$	$F_s(2M+2N_b)$ $+\frac{F_s}{N_f}\left(6N_f\log_2 2N_f+9N_f\right)$ $+\frac{F_s}{N_b}(6N_b\log_2 2N_b+9N_b)$

3.6 Experimental Setup

In this section, the experimental set-up used for the demonstration of the developed methodology is presented.

3.6.1 System Architecture

In this section, the details of experimental setup used to verify the proposed methodology is shown. The structure is obtained by saw cutting the rear left quarter of BIW of a newly designed vehicle. The rear left quarter is selected based on the problematic behavior of the region on the vehicle level NVH tests. The damping materials on the panels are removed. An iron frame is built to support the quarter BIW assembly through four air springs. The frame also provides an inclination angle of the structure similar to the configuration of a real vehicle. Additionally, reinforcements are applied on specific regions to inhibit residual modes due to non-contact sections as a consequence of rough saw cutting process.

The system is composed of the rear left quarter of the BIW vehicle, PZT actuators and sensors, a digital controller, signal generator and signal analyzer. Details of the experimental set-up and the components of the set-up are shown in Figure 3.4

Figure 3. 4 Details of the experimental set-up a) PZT actuator b) PZT sensor c) Shaker d) Controller Unit e) DC Power Supply f) PZT amplifier g) Oscilloscope h) Signal Generator i) Signal Analyzer

The piezoelectric actuators and sensors are the PI P876.A12 bender type actuators which are explained in section 2.5.1. Those are the high voltage low weight structures which do not affect the dynamic characteristics of the system. The structure is made of steel with thickness of 1.2mm.

3.6.2 Sensor/Actuator Placement

To have control authority on the system for the target frequency range is crucial in vibration control for good performance of the vibration suppression. The PZT actuators used in study are the strain type actuators and the high strain regions are the suitable ones for the effective operation of the PZT actuators [41]. To identify such regions, finite element model (FEM) of the structure is built. The FEM is built via MSC.Nastran by measuring the accurate dimensions of the quarter BIW structure. Since the wheelhouse of the vehicle is found to be problematic region in NVH tests, 74 measurement points are selected to perform experimental modal analysis. The most suitable region on the wheelhouse for the PZT implementation and the most influential part of the wheelhouse is found and named as zone 1 as shown in Figure 3.5a.

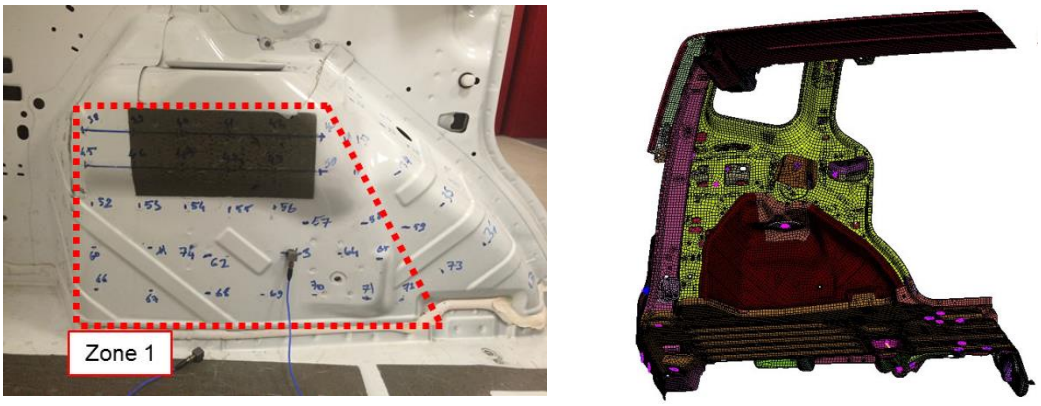

Figure 3. 5 a) The complex 3D structure sub-region for piezo patch applications b) Experimental Setup FEM

After the creation of the FEM, the modal analysis is performed and the results are verified by the experimental analysis. The low frequency modes of the wheelhouse are listed in Table 3.2 for FEM and experimental analysis while the mode shapes are shown in Figure 3.6.

Table 3. 2 Results of the FEM and Experimental Modal Analysis

	Mode 1	Mode 2	Mode 3
Numerical	143.2 Hz	186.5 Hz	201.4 Hz
Experimental	143.1 Hz	183.3 Hz	198.7 Hz

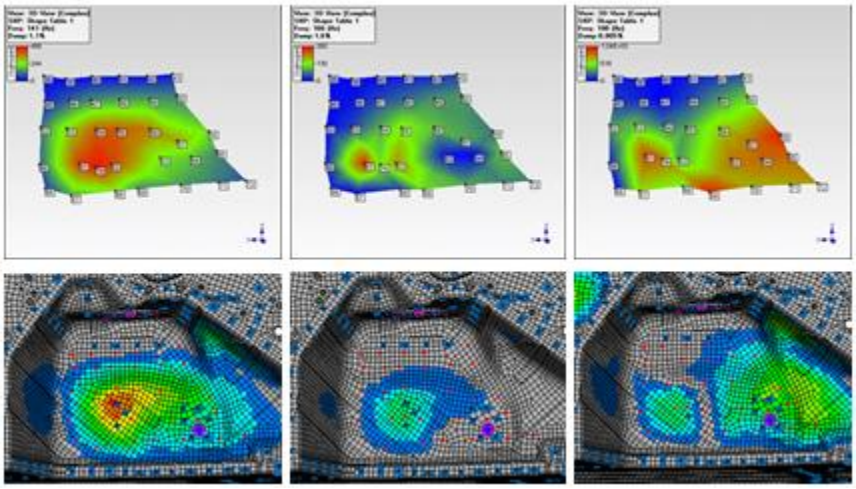

Figure 3. 6 Zone 1 Modal Test Results, experimental and FE as a) Mode Shape 1 b) Mode Shape 2 c) Mode Shape 3

Based on the evaluations of the modal properties, the PZT actuator and sensors are located on the positions shown in Figure 3.7.

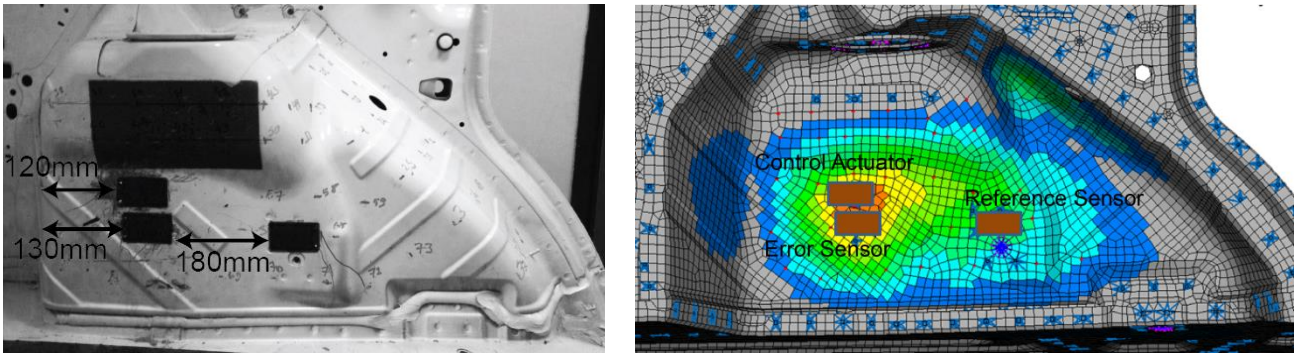

Figure 3. 7 Piezoelectric patch locations on the structure a) Experimental Set-up b) FEM

3.6.3 Modelling of the System

In order to generate accurate representation of the system, the models of the primary path P(z), and secondary path S(z) are generated. Both of the modelling procedures are accomplished in time domain using FIR filters and 512 parameters are used for the representation of the dynamics.

A random signal with variance of 0.2 is generated and filtered to confine the signal within the bandwidth of the 0-220 Hz for the modelling of the primary path, P(z). The generated signal is send to the shaker which is used as the disturbance actuator by using output channel of the NI-PCI 6229 m-series DAQ unit. The reference signal, x(n) is measured using a nearly-collocated PZT sensor with the disturbance actuator. Meanwhile, the error sensor, which is nearly-collocated with the control actuator is used to measure the e(n) and using MATLAB/Simulink, LMS algorithm is implemented to extract the model of the P(z). Figure 3.8 shows the error level between the estimated output at the error sensor using the reference signal and the actual measured error signal.

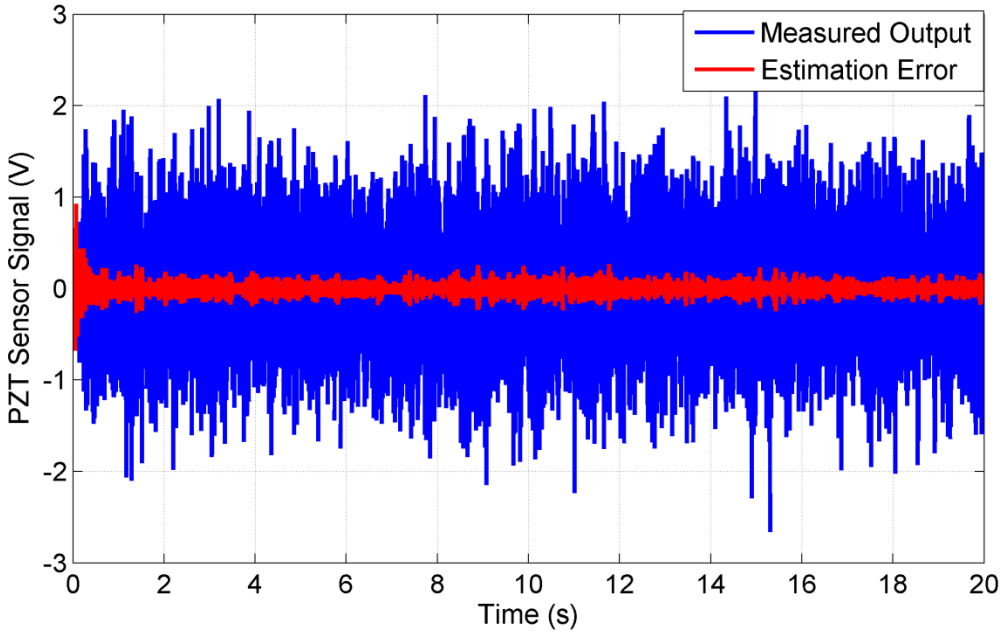

Figure 3. 8 Modeling of the P(z)

The LMS algorithm is also used for the derivation of the secondary path model, S(z). For the modelling of the S(z), again the NI-PCI 6229 is used to generate a random signal with the properties explained for deriving the P(z). However, this time the generated

signal itself is used as the reference signal and the error sensor is used to measure the error signal e(n). Using MATLAB/Simulink, the LMS algorithm is implemented and the resultant filter parameters are used for further analysis. Figure 3.9 shows the actual output level of the error sensor measurement and the error between the estimated model output and the actual output.

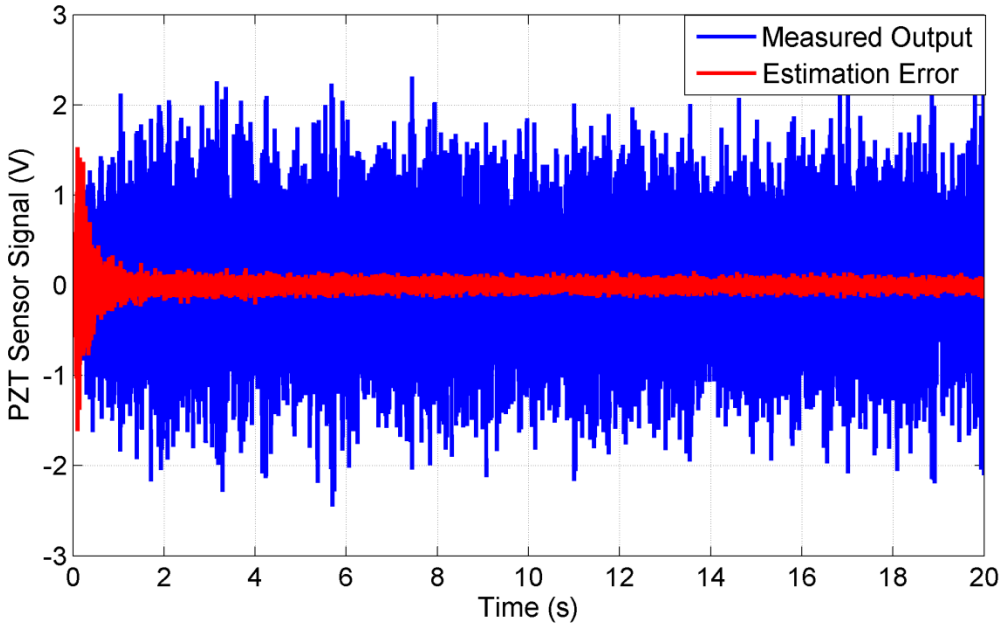

Figure 3. 9 Modeling of the S(z)

Figure 3.10 a-b shows the filter parameters obtained after the modeling procedure and the Figure 3.10 c-d shows the frequency responses of the modeling filters for primary and secondary paths respectively. Please note that the behavior of the modeling filters observed in frequency domain differs from the FRF measurements and this is due to nature of the FIR filters.

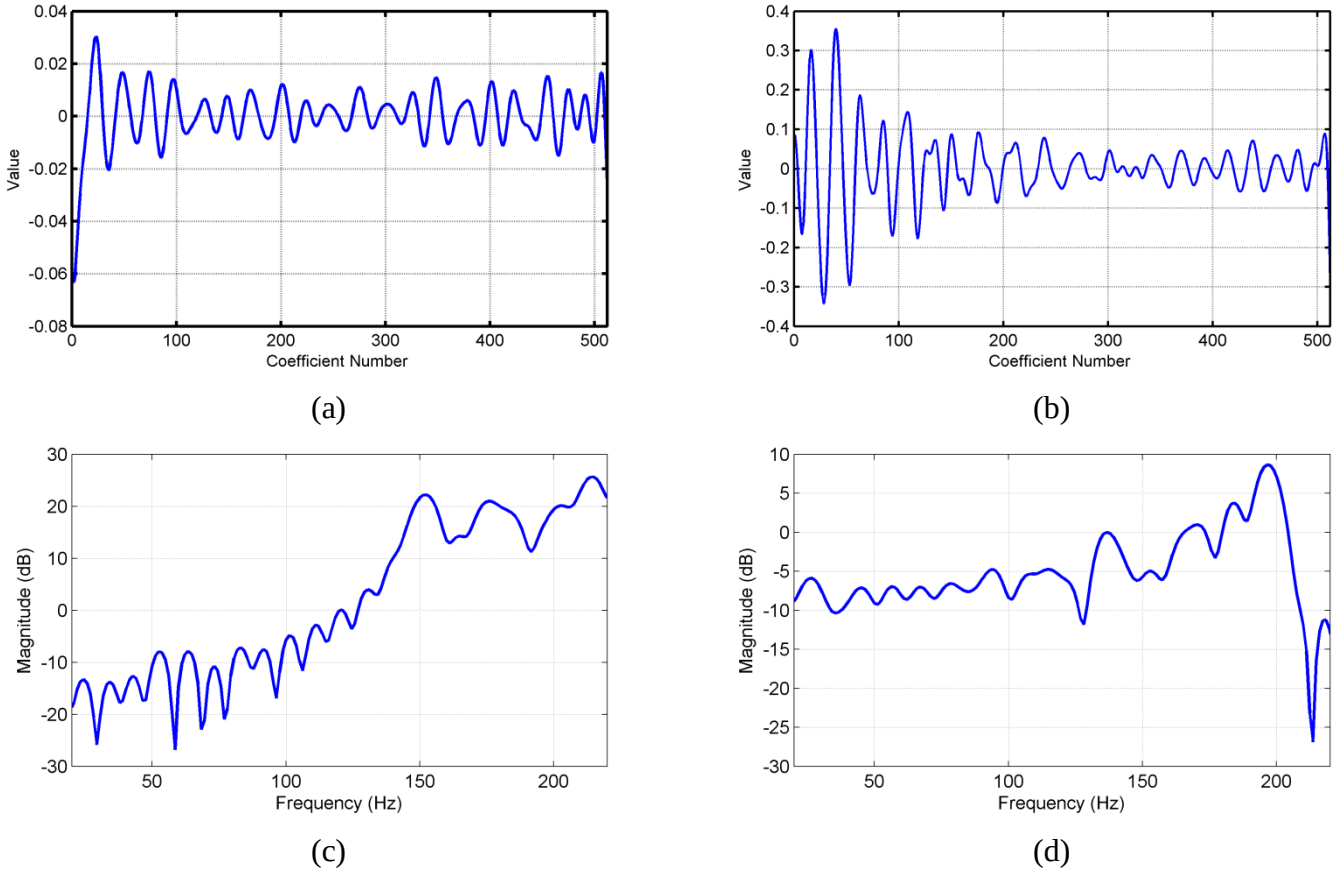

Figure 3. 10 Modeling Filter Parameters a) Primary Path P(z) b) Secondary Path S(z) c) Frequency response of the P(z) modeling filter d) Frequency response of the S(z) modeling filter

Please note that, unlike many previous studies, the reference signal, x(n) does not have the uniform frequency characteristics. Thus, the dynamics between the primary disturbance which is the signal generated by NI-PCI 6229 and its effect on the BIW structure which is the signal level on the reference sensor should be known for numerical evaluation. For this purpose, Frequency Response Function (FRF) of the dynamics between the generated random input and the reference sensor is measured and an 8^{th} order transfer function model

is generated to represent those dynamics for numerical evaluation. The Figure 3.11 shows the frequency response function (FRF) of the actual system and modeled dynamics between disturbance signal and the reference sensor.

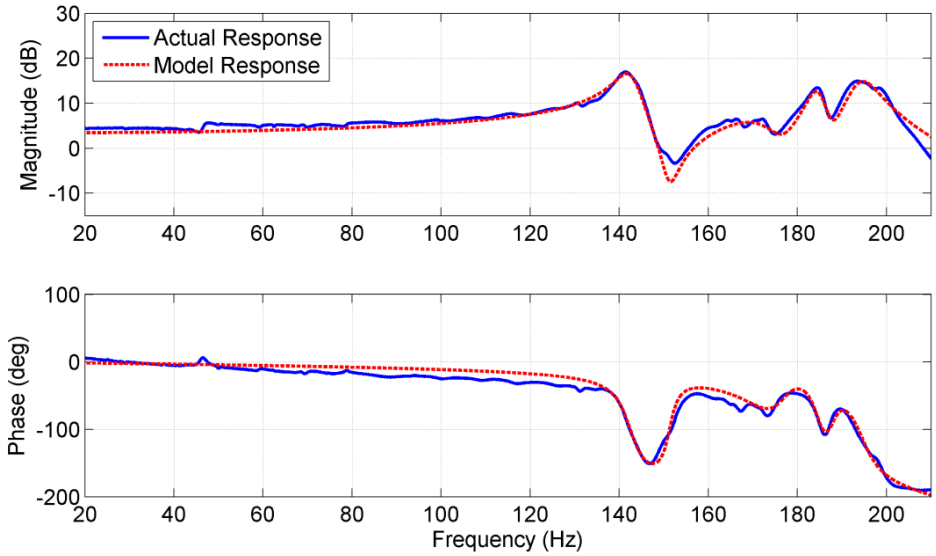

Figure 3. 11 Frequency Response Function (FRF) of the disturbance signal and the reference sensor for actual dynamics and model dynamics

3.7 Controller Implementation

The diagram of the controller architecture is shown in Figure 3.12. The undesired vibration on the structure is generated using a signal generator and a shaker is used for stimulating the undesired vibration on the structure. The reference sensor is placed close to the shaker (nearly collocated configuration). Since our aim is to mimic the moving vehicle, it is not possible to implement the collocated configuration. Such difficulty is due to the presence of the tire assembly and vulnerability of the sensor to the operational effects (such that the dust, stones etc.) on the outer side of the structure. Furthermore, even though such problems can be avoided, the cabling requirements for data transfer are still very problematic in collocated configuration. The control actuator is used to suppress the

vibration of the structure and the error sensor is also configured as nearly collocated to the control actuator. NI-PCI 6229 DAQ unit is used for controller implementation and the performance of the controller is monitored utilizing a signal analyzer. The error sensor signal and reference sensor signals are transferred to NI PCI 6229 DAQ unit to generate control signal. The control signal is then transferred to the control actuator utilizing the E413.D2 type signal amplifier.

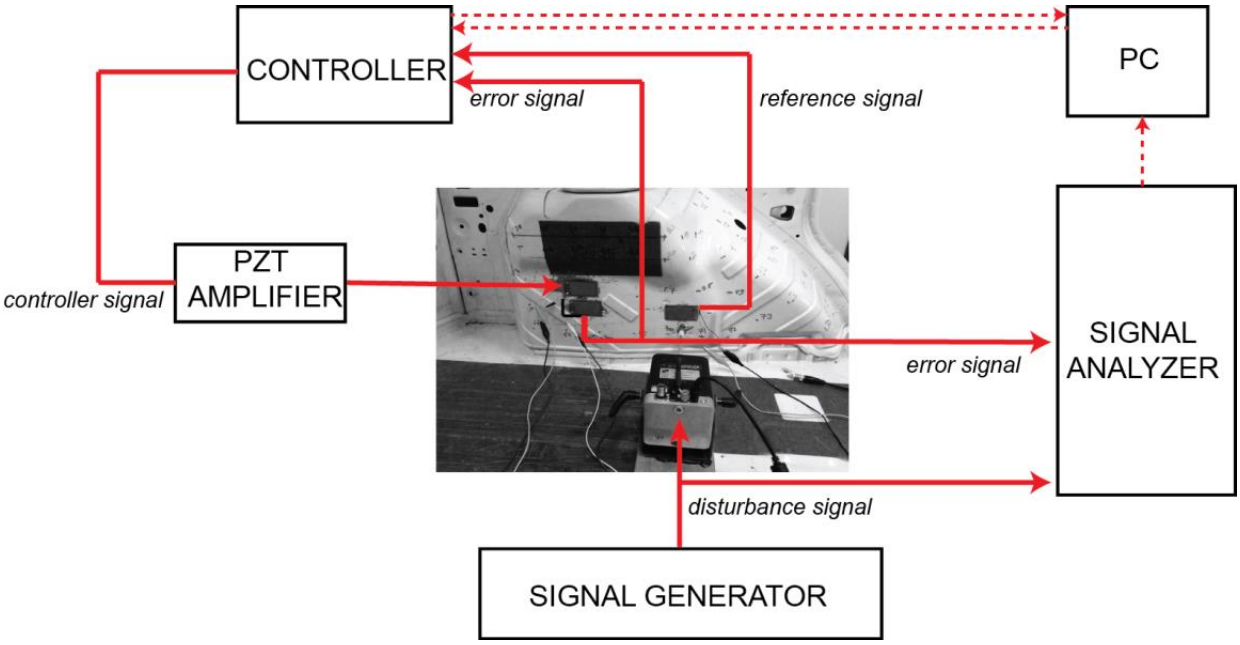

Figure 3. 12 Schematics of the controller configuration

3.8 Numerical and Experimental Results

In this section, numerical and experimental evaluation of the SM and the proposed algorithm for AVC is presented. The frequency range of interest is chosen as 50-220 Hz since the dominant low frequency modes of the BIW structure lay within this range of frequency. To evaluate the performance of the controller numerically and experimentally, a random signal is generated using the signal generator to induce primary disturbance on the

system. The primary disturbance signal is used to excite structure via a modal shaker and the dynamic characteristics of the primary input on the BIW structure is evaluated using the reference signal.

For numerical evaluations, the level of the disturbance signal is adjusted to 0.15Vrms. The disturbance signal induced reference signal with level of 0.1Vrms. The open loop response level at the error sensor is 0.5Vrms. MATLAB/Simulink is used for performance assessment of the controllers. The performance evaluations for both of the algorithms are completed using only random input since the road induced vibration has random characteristics rather than purely harmonic effects. The performances of numerical and experimental configurations are compared both in time domain and frequency domain. Sampling frequency of the system is adjusted to 5000Hz for both numerical and experimental studies. The SM algorithm implementation requires an IIR filter and the filter includes 512 parameters for forward loop and 512 parameters for the feedback loop. The step size μ is 0.0001 in time domain controller while it is 0.0006 in developed methodology.

In Figure 3.13 time domain control performances for both of the algorithms are compared. The Figure 3.13a-b shows the time domain vibration suppression performance of the SM algorithm whereas Figure 3.13c-d shows the time domain performance for the proposed algorithm. The controller is activated 5 seconds after the disturbance initiation. From the Figure 3.13, it is observed that the simulations match very well with the experimental results. During the transition, the time domain approach and the proposed approach behaved similarly. After the convergence to the steady state levels, the time domain amplitude of the proposed algorithm is slightly less than the SM approach. Still similar amplitudes are observed for the steady state performance. This is acceptable since the SM algorithm ensures the convergence of the filter parameters to the near optimal solution which should be close for both of the cases.

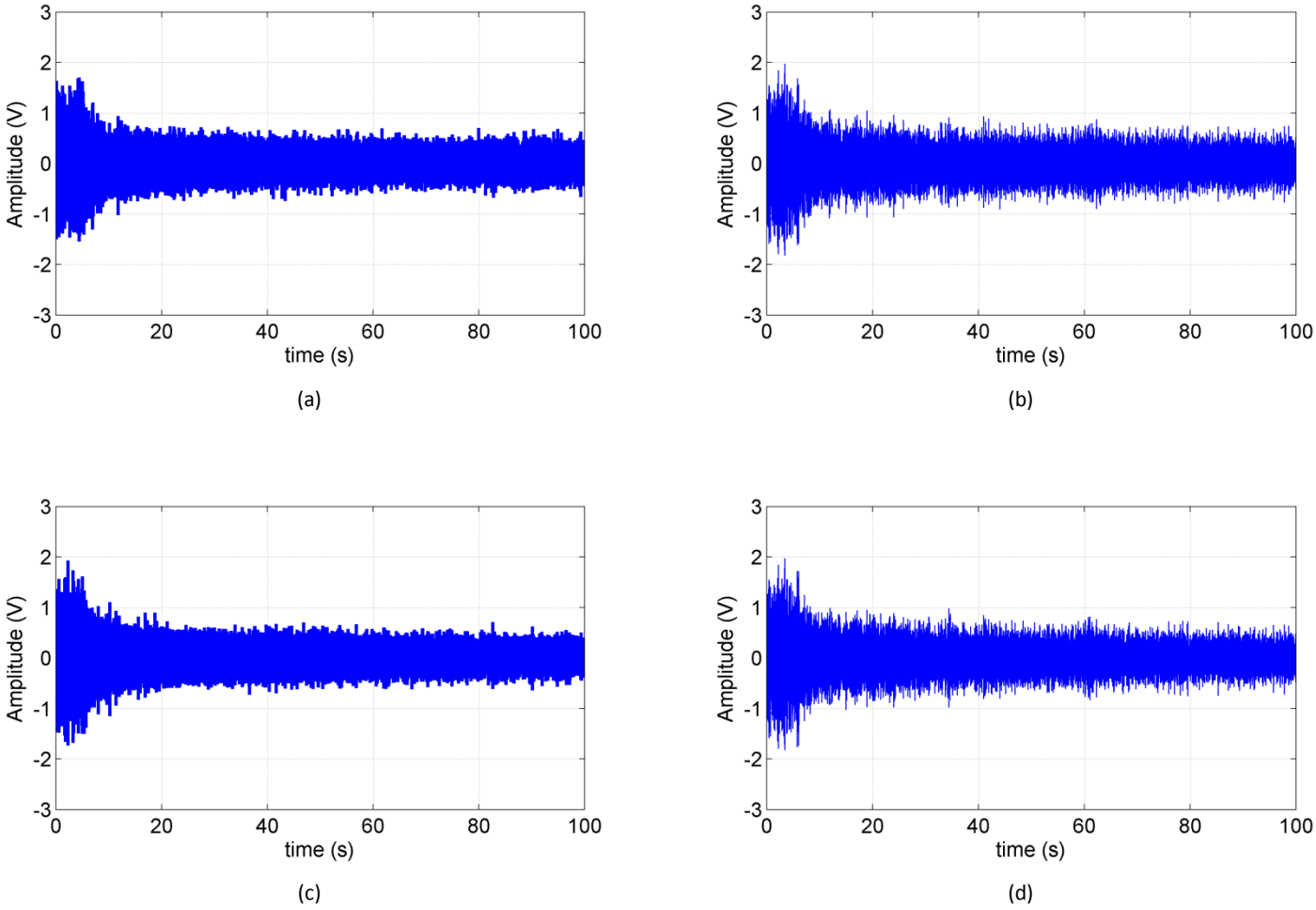

Figure 3. 13 Time domain performance evaluation for the SM and the time-frequency domain SM method a) SM in experiments b) SM in simulations c) Hybrid SM in experiments d) Hybrid SM in simulations

For further analysis, the frequency domain characteristics of the controller for both SM and proposed approach are calculated and compared. For this purpose, open loop and closed loop measurements are completed when the controller is offline and online. The experimental results are obtained by averaging10 different experiments. The Figure 3.12 a-b shows the frequency domain suppression performance of the time domain SM controller

for experiment and simulations, respectively. Figure 3.12 c-d shows the controller performance of the proposed approach in experiments and simulations. From the figure 3.12 it can be concluded that the frequency domain suppression levels are accurately predicted by the simulation model and both of the algorithms are successful in suppressing the vibrations of the structure.

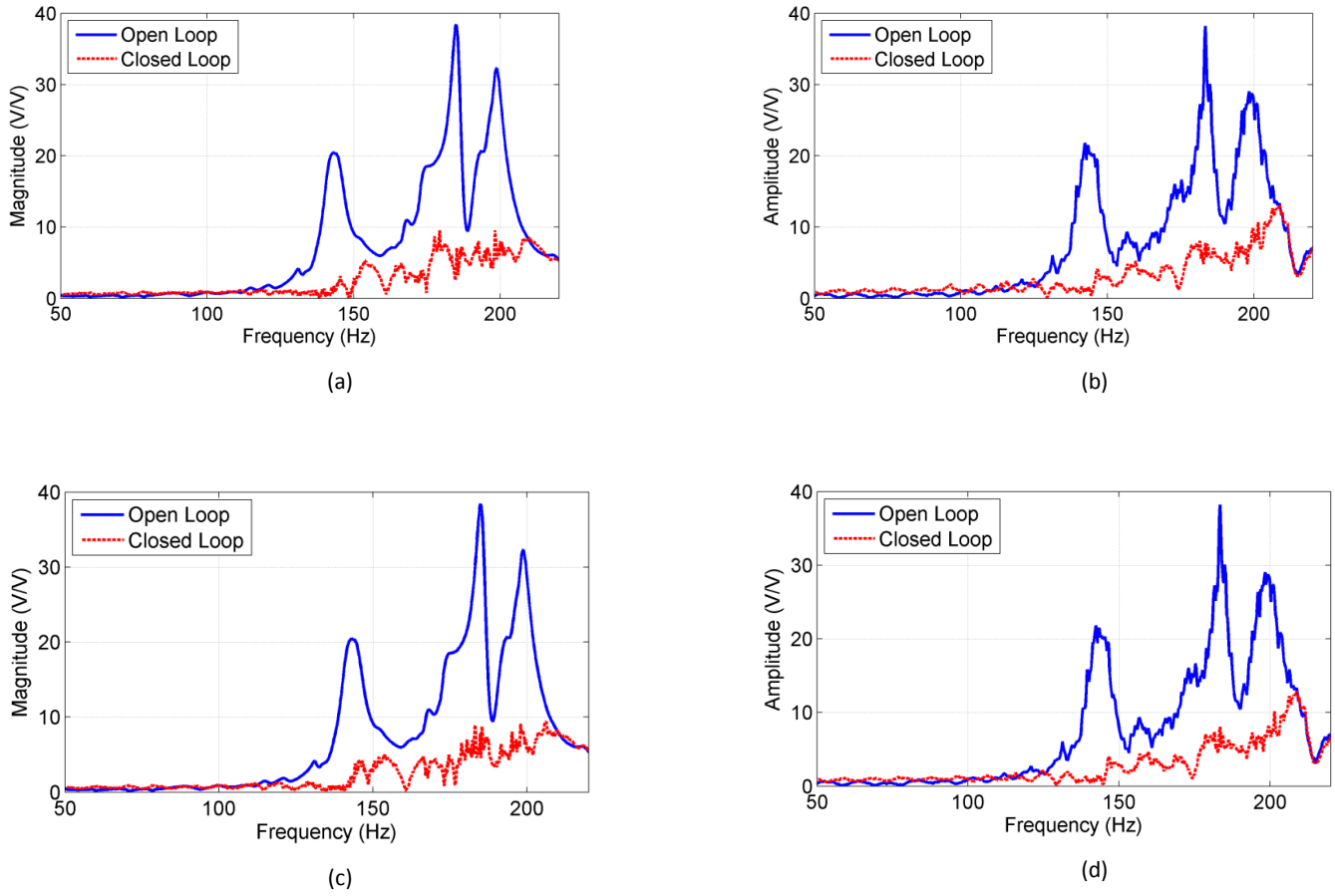

Figure 3. 14 Frequency domain performance evaluation for the SM and the time-frequency domain SM method a) SM in experiments b) SM in simulations c) Hybrid SM in experiments d) Hybrid SM in simulations

However the proposed hybrid approach has one advantage over the SM algorithm. Recalling the Table 3.1 and evaluating the number of multiplications for both of the

approach yields the following results shown in Table 3.3. Table 3.3 shows the number of multiplication required for per second of the both algorithms. The evaluation of the number of the multiplications shows that the computational complexity is decreased by 28.9% by updating the filter weight coefficients in frequency domain.

Table 3. 3 Comparison of the computational complexity for the SM and proposed Hybrid algorithm for parameter numbers of our case

Algorithm	***Parameters***	×	***total*** **computation**	***Percent saving per second*** $\left(\frac{\boldsymbol{SM-Hybrid}}{\boldsymbol{SM}}\right)\mathbf{100}\%$
SM	$M = 512$ $N_f = 512$ $N_b = 512$ $F_s = 5000$	$F_s(2M + N_f + 3N_b + 2)$	15370000	$= \frac{15370000 - 10930000}{15370000} \times 100\%$ $= 28.9\%$
Hybrid	$M = 512$ $N_f = 512$ $N_b = 512$ $F_s = 5000$	$F_s(2M + 2N_b)$ $+ \frac{F_s}{N_f}\left(6N_f \log_2 2N_f + 9N_f\right)$ $+ \frac{F_s}{N_b}(6N_b \log_2 2N_b + 9N_b)$	10930000	

3.9 Conclusion

In this chapter, a new hybrid AVC algorithm based on IIR filtering is proposed. For this purpose the SM algorithm is taken as reference and modified in a way to include the FDAF approach. Then, the performance of the SM algorithm and proposed hybrid SM method are investigated and compared numerically and experimentally. To demonstrate the efficiency of both SM algorithm and the proposed method, an experimental set-up is constructed using left quarter BIW model of a real vehicle. The sensor actuator configuration is adjusted based on the FEM of the experimental set-up. The FEM of the structure is constructed and compared with the experimental response of the structure. Both

of the algorithms are implemented on the structure in numerical and experimental analysis. The results showed that both of the algorithms are beneficial in terms of vibration suppression and showed similar performances both in time domain and simulations. The proposed method is beneficial since computational performance of the algorithm is increased by 28.9% for the number of parameters specified for the analysis.

Chapter 4

ACTIVE VIBRATION CONTROL OF A VEHICLE IN OPERATING CONDITIONS USING PZT ACTUATORS

4.1 Introduction

In this chapter, active vibration control methodology developed for controlling the road induced disturbances on a vehicle is presented. A vehicle produced by Ford-OTOSAN Company is used in the AVC studies.. The preliminary analysis and tests completed by Ford OTOSAN on the vehicle show that the vibration problem on the driving condition is mainly due to wheelhouse of the structure around 150 Hz. The studies completed in this chapter demonstrate that it is possible to suppress such vibration characteristics by using PZT actuators. For this purpose, two different feedback approaches are implemented and compared. In the first step, the PZT actuator and sensor locations are determined for the vehicle. Then, in order to suppress the structural mode of the wheelhouse, a Positive Position Feedback (PPF) algorithm and an LQG controller are implemented. The results of those two approaches are compared afterwards.

The controller setup used in this chapter consists of a commercial vehicle with PZT actuators bonded on the surface of the wheelhouse. DSpace autobox 1401/1507 model real time controller is used to implement the aforementioned algorithms. In order to use DSpace autobox, a signal conditioner circuit is built for the modification of the sensor and actuator signal to ensure proper signal processing. The tests are performed on a prespecified track while the vehicle is moving with 40kph at 2^{nd} gear. Those operation conditions are determined to ensure that the structural modes of the wheelhouse are excited while driving the car. Performances of the controller in both algorithms are evaluated for open loop and

closed loop cases. Since the reference signal is not measurable, autospectrum of the PZT sensor is measured as the indicator of the controller performance. Furthermore, two accelerometers are used in addition to monitor the vibration suppression level on two different regions of the wheelhouse to demonstrate the fact that the actuators do not amplify the vibrations in the other locations of the structure. The results presented in this chapter are the average of 10 different road tests to eliminate the discrepancies between adjacent measurements.

4.2 PPF Controller

In this section, Positive Position Feedback (PPF), which is initially proposed by Fanson and Caughey [54], is explained.

PPF is known to be effective on suppressing single mode vibrations of structures [55]. In addition to that, PPF is also known to control the target vibration mode without destabilizing other modes with higher bandwidths of the structure [54].

The governing equations for the PPF controller are shown as follows.

$$structure: \ddot{\delta} + 2\zeta\omega\dot{\delta} + \omega^2\delta = g\omega^2\eta$$
$$compensator: \ddot{\eta} + 2\zeta_f\omega_f\dot{\eta} + \omega_f^2\eta = \omega_f^2\delta \quad (4.1)$$

Here δ is the modal coordinates of the target structure, η is the compensator coordinate, ω and ω_f are the structure and filter frequencies. ζ and ζ_f are the structural and compensator damping ratios respectively. g is the scalar gain of the controller.

After manipulating the eq (4.1), the transfer function for the PPF compensator can be written as

$$H_f = \frac{\omega_f^2}{s^2 + 2\zeta_f \omega_f s + \omega_f^2} \tag{4.2}$$

The basic tuning parameters of the PPF are the natural frequency ω_f and the damping ratio ζ_f of the PPF controller. It is reasonable to adjust natural frequency of the PPF controller to the vibration mode of interest of the target structure since the signal created by the controller would be effective at that particular frequency.

The block diagram of the PPF controller is given in Figure 4.1. Here d is the disturbance signal on the structure created by the input, w. The output signal y is the measured sensor output. The designed PPF controller has the input of the sensor signal, y. The output of the controller is then fed to the actuator used for the suppression of the vibration.

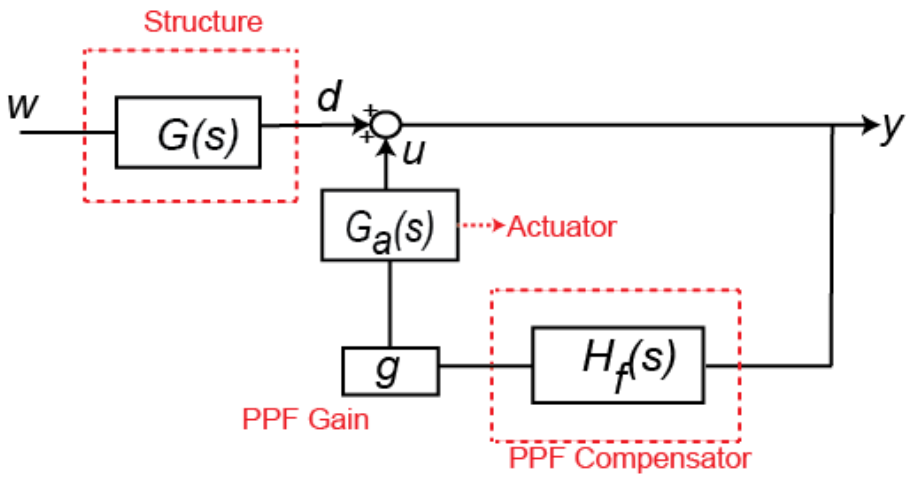

Figure 4. 1 PPF block diagram

4.3 LQG Controller

In this section, design and implementation of the LQG controller is presented. LQG controllers are both considered optimal and robust. LQG controller utilizes system model to generate controller output while an optimal estimator is used to compensate for the possible discrepancies in the state estimation due to process and measurement noises present in the system. In general, LQG controllers are the combination of the Linear Quadratic Regulator (LQR) and Kalman State Estimator algorithms. Prior to detailed explanation on the LQR and Kalman Estimator, it is suitable to define the state space representation and the optimal control law.

4.3.1 State-Space Representation

A state-space representation is a mathematical model of a physical system as a set of input, output and state variables related by first order differential equations. For the dynamic system, the state of a system is described in terms of a set of state variables such as

$$\boldsymbol{x} = [x_1(t)\ x_2(t)\ x_3(t) \dots\ x_n(t)] \tag{4.3}$$

State variables describe the present configuration of the system and can be used to determine the future response given the excitation inputs and the equations describing the dynamics[56].

Response of a system is described as set of first order differential equations written in terms of state variables and the inputs. These first order differential equations can be written as

$$\begin{aligned}
\dot{x}_1 &= a_{11}x_1 + a_{12}x_2 + \dots + a_{1n}x_n + b_{11}u_1 + \dots + b_{1m}u_m \\
\dot{x}_2 &= a_{12}x_1 + a_{22}x_2 + \dots + a_{2n}x_n + b_{21}u_1 + \dots + b_{2m}u_m \\
&\vdots \\
\dot{x}_n &= a_{n1}x_1 + a_{n2}x_2 + \dots + a_{nn}x_n + b_{n1}u_1 + \dots + b_{nm}u_m
\end{aligned} \tag{4.4}$$

In this representation $\dot{x} = \frac{dx}{dt}$ and those set of equations can be converted to matrix form as in Equation 4.5

$$\frac{d}{dt}\begin{bmatrix} x_1 \\ x_2 \\ \cdot \\ \cdot \\ x_n \end{bmatrix} = \begin{bmatrix} a_{11} & a_{12} & \dots & a_{1n} \\ a_{21} & a_{22} & \dots & a_{2n} \\ \vdots & \vdots & \ddots & \vdots \\ a_{n1} & a_{n2} & \dots & a_{nn} \end{bmatrix} \begin{bmatrix} x_1 \\ x_2 \\ \cdot \\ \cdot \\ x_n \end{bmatrix} + \begin{bmatrix} b_{11} & \dots & b_{1m} \\ \vdots & \ddots & \vdots \\ b_{n1} & \dots & b_{nm} \end{bmatrix} \begin{bmatrix} u_1 \\ \vdots \\ u_m \end{bmatrix} \tag{4.5}$$

The column matrix consisting the state variables is called the state vector and written as

$$\boldsymbol{X} = \begin{bmatrix} x_1 \\ x_2 \\ \cdot \\ \cdot \\ x_n \end{bmatrix} \tag{4.6}$$

The vector of the input signal is defined as *u*. Then the system can be represented by the compact notation of the state space differential equations

$$\dot{\boldsymbol{x}} = \mathbf{A}\boldsymbol{x} + \mathbf{B}\boldsymbol{u} \tag{4.7}$$

A is the square matrix with dimension of n-by-n and **B** is called input matrix with a dimension of n-by-m. The state differential equation relates the rate of change of the state vector to the state of the system and the input given to the system. The outputs of the system are related to the state variables and the input signals by the output equation

$$\boldsymbol{y} = \boldsymbol{C}\boldsymbol{x} + \boldsymbol{D}\boldsymbol{u} \tag{4.8}$$

Where y is the set of output signals, expressed in column vector form. The state space representation comprises the state differential equation and the output equation[56].

4.3.2 Optimal Control Law

In this section, optimal control law is presented. Optimal control law is nothing but the reformulated form of an optimization approach specific to control applications. Thus, a functional which defines the optimality of the control action must be defined first. The Equation 4.9 is the general form of the functional used for the optimal control:

$$u^{*}(t) = f(x(t), t) \tag{4.9}$$

The functional, *f*, in Equation 4.3 is the optimal control law or in other words optimal control policy. Such configuration of the functional suggests that the optimal control input is dependent on the measurement of the system states $x(t)$ and time.

An example of optimality is given by using the path selection problem given in Figure 4.3. According to the figure, it is possible to reach to point c by starting at point a and stopping at point b using 9 different combinations. However, the shortest path is only one of those combinations and to find the shortest path is the problem of optimality.

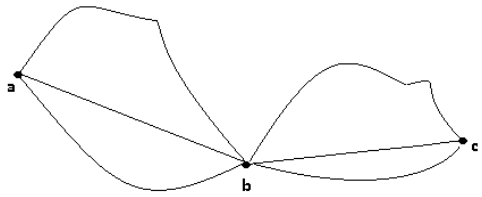

Figure 4. 2 Optimality Problem, Path Selection

To solve such a problem, cost functions are used to represent the problem in mathematical terms. Considering the optimality problem in terms of control and the functional given in Equation 4.3, cost function should have two components to incorporate the current values of the states and the control input u for the optimal generation of the control action. The most basic form of optimal control cost function is given in Eq 4.10

$$J = x^2(T) + \lambda \int_0^T u^2(t) \tag{4.10}$$

Here, the problem is designed for a time window where the *T* is the final time. Cost function *J* allows adjustment of the contribution of the two terms through weighting, λ. *x(T)* and *u(t)* are squared since negative or positive terms of those values have equal importance. *J* reflects desire to drive final state close to its desired value without excessive expenditure of control effort. Amount of effort for control system is regulated by the weighting included in the cost function.

4.3.2.1 Linear Quadratic Regulators

In this subsection, Linear Quadratic Regulators (LQR) are presented. LQR aims to minimize integral square error by minimizing cost function *J* over a time interval. In linear regulation problem the optimal control law can be determined in the form of a linear time-varying function. The plant interested in this optimality problem is described by linear state equations and given by:

$$\dot{\boldsymbol{x}}(t) = \boldsymbol{A}(t)\boldsymbol{x}(t) + \boldsymbol{B}(t)\boldsymbol{u}(t) \tag{4.11}$$

The aim of the control law is to minimize the cost function J which is the performance measure and given by:

$$J = \frac{1}{2}\boldsymbol{X^t}(t_f)\boldsymbol{H}\boldsymbol{x}(t_f) + \frac{1}{2}\int_{t_0}^{t_f}[\boldsymbol{X^T}(t)\boldsymbol{Q}(t)\boldsymbol{X}(t) + \boldsymbol{U^T}\boldsymbol{R}(t)\boldsymbol{U}(t)]dt \tag{4.12}$$

Here *X* is state vector and *U* is input vector. $\boldsymbol{Q}$ and $\boldsymbol{R}$ are called weighting matrices. For a particular linear quadratic regulator design, tuning parameters are those two matrices.

The final time is fixed ("t_f"), $\boldsymbol{H}$ and $\boldsymbol{Q}$ are real symmetric positive semi-definite matrices, and R is a real symmetric positive definite matrix. It is assumed that the states and controls are not bounded, and $\boldsymbol{x}(t_f)$ is free. It is desired to maintain the state vector close to the origin without an excessive expenditure of control effort.

In order to obtain a solution to such problem, matrix Riccati equations are used. Following equation is the general form of the Riccati equations for optimum solution in LQR.

$$\dot{\boldsymbol{K}}(t) = -\boldsymbol{K}(t)\boldsymbol{A}(t) - \boldsymbol{A^T}(t)\boldsymbol{K}(t) - \boldsymbol{Q}(t) + \boldsymbol{K}(t)\boldsymbol{B}(t)\boldsymbol{R^{-1}}(t)\boldsymbol{B^T}(t)\boldsymbol{K}(t) \tag{4.13}$$

With the boundary condition $(t_f) = \boldsymbol{H}$. Here $\boldsymbol{H}$ stands for the Hamiltonian. For further information for the steps of the solution please refer to [57].

These equation can be integrated numerically by a digital computer by starting the integrating at $t = t_f$ and proceeds backwards in time to $t = t_0$ $\boldsymbol{K}(t)$ is stored and solution of the cost function leads to convergence to an optimal gain matrix, $\boldsymbol{K}$, which is used in calculating optimal input such that :

$$\boldsymbol{u}(t) = -\boldsymbol{K}\boldsymbol{x}(t) \tag{4.14}$$

Where x is state vector. For a time interval specified by, cost function is solved using iterative methods but as the final time goes to infinity, optimal gain matrix K, is the riccati solution of the cost function. In Figure 4.3, block diagram for the Linear Quadratic Regulator is shown.

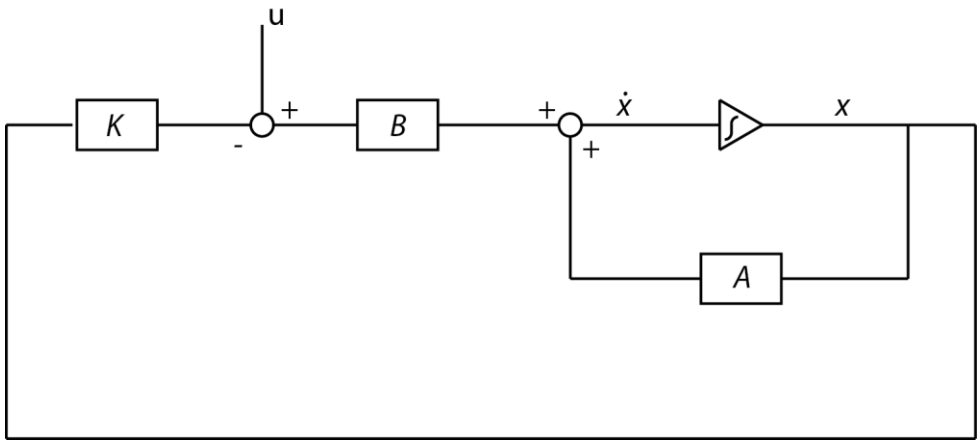

Figure 4. 3 Block Diagram of the Linear Quadratic Regulator

4.3.2.2 Kalman Filter

In this section the Kalman Filter algorithm is described. Since the discrete time approach is used in this chapter, discrete time Kalman Filter is presented [58]. The Kalman Filter addresses the general problem of estimating the states of a process described by linear stochastic equations such that

$$\begin{aligned} \boldsymbol{x_k} &= \boldsymbol{A x_{k-1}} + \boldsymbol{B u_k} + \boldsymbol{W w_{k-1}} \\ \boldsymbol{y_k} &= \boldsymbol{C x_k} + \boldsymbol{D u_k} + \boldsymbol{v_k} \end{aligned} \tag{4.15}$$

Here x_k is the states of the system, $\boldsymbol{A}, \boldsymbol{B}, \boldsymbol{C}$ and $\boldsymbol{D}$ are the system matrices with appropriate dimensions, $\boldsymbol{y_k}$ is the measurement for time instant k. $\boldsymbol{w_k}$ and $\boldsymbol{v_k}$ are process noise and measurement noise respectively. They are assumed to be independent from each other, and as white noises with normal probability distribution with process noise covariance $\boldsymbol{Q_k}$ and $\boldsymbol{R_k}$ respectively. The values of the $\boldsymbol{Q_k}$ and $\boldsymbol{R_k}$ may change with the time however here we also assume that they are constant.

There are two different origins of the Kalman Filter. Those are computational origins and the probabilistic origins. Starting with the computational origin of the filter, first $\hat{\boldsymbol{x}}_{\boldsymbol{k}}^{-}$ is defined as a priori estimate of the system states based on the knowledge of the process prior to time step k. Then a posteriori estimate at time step k is defined as $\hat{\boldsymbol{x}}_{\boldsymbol{k}}$. The estimate errors for a priori and a posteriori estimates with respect to actual state values can be defined as

$$\begin{aligned} \boldsymbol{e_k^-} &\equiv \boldsymbol{x_k} - \hat{\boldsymbol{x}}_{\boldsymbol{k}}^{-} \\ \boldsymbol{e_k} &\equiv \boldsymbol{x_k} - \hat{\boldsymbol{x}}_{\boldsymbol{k}} \end{aligned} \tag{4.16}$$

Then, the a priori and a posteriori estimate error covariance are defined as $P_k^- = E\left[e_k^- e_k^{-T}\right]$ and $P_k = E[e_k e_k^T]$. In deriving the equations of the Kalman Filter, the goal is to find an equation that computes $\hat{\boldsymbol{x}}_{\boldsymbol{k}}$ as linear combination of the $\hat{\boldsymbol{x}}_{\boldsymbol{k}}^{-}$ and the weighted difference between the predicted measurement $\boldsymbol{C}\hat{\boldsymbol{x}}_{\boldsymbol{k}}^{-}$ and the actual measurement $\boldsymbol{y_k}$ as

$$\hat{\boldsymbol{x}}_{\boldsymbol{k}} = \hat{\boldsymbol{x}}_{\boldsymbol{k}}^{-} + \boldsymbol{K}_{\boldsymbol{obs}}(\boldsymbol{y}_{\boldsymbol{k}} - \boldsymbol{C}\hat{\boldsymbol{x}}_{\boldsymbol{k}}^{-}) \tag{4.17}$$

The difference $(\boldsymbol{y}_{\boldsymbol{k}} - \boldsymbol{C}\hat{\boldsymbol{x}}_{\boldsymbol{k}}^{-})$ is called residual. The residual is the discrepancy between the actual measurement and the predicted output. $\boldsymbol{K}_{\boldsymbol{obs}}$ in Equation 4.17 is the gain or the blending factor that minimizes the a posteriori error covariance given as $P_k = E[e_k e_k^T]$. Such minimization problem can be solved by incorporating Equation. 4.17 to Equation 4.16 with taking derivative of the total equation system with respect to $\boldsymbol{K}_{\boldsymbol{obs}}$ and setting the result to the 0. For more details please consult to [59] One form of the resulting K_{obs} that minimizes the $P_k = E[e_k e_k^T]$ is given by

$$\boldsymbol{K}_{\boldsymbol{k}} = \boldsymbol{P}_{\boldsymbol{k}}^{-}\boldsymbol{C}^{\boldsymbol{T}}(\boldsymbol{C}\boldsymbol{P}_{\boldsymbol{k}}^{-}\boldsymbol{C}^{\boldsymbol{T}} + \boldsymbol{R})^{-\boldsymbol{1}} \tag{4.18}$$

From Equation 4.18 it is obvious that the as R approaches 0, the gain $\boldsymbol{K}_{\boldsymbol{obs}}$ weights the residual more heavily. On the other hand as P_k^- approaches zero, the gain K_{obs} weights the residual less heavily. In other words, as the measurement error covariance R decreases, the actual measurement y_k is trusted more and more while the predicted measurement $\boldsymbol{C}\hat{\boldsymbol{x}}_{\boldsymbol{k}}^{-}$ is trusted less and less. On the other hand as the P_k^- approaches zero the $\boldsymbol{C}\hat{\boldsymbol{x}}_{\boldsymbol{k}}^{-}$ is trusted more and more while the actual measurement y_k is trusted less and less. With this remark the computational origins of the Kalman Filtering is finished. From now on, the probabilistic origin of the Kalman filter is presented.

Recalling the Equation 4.17 the justification is rooted in the probability of the estimate $\hat{\boldsymbol{x}}_{\boldsymbol{k}}^{-}$ on all prior measurements z_k (Bayes' rule). For now let it suffice to point out the first two moments of the state distribution are used by Kalman Filter.

$$E[x_k] = \hat{x}_k \tag{4.19}$$
$$E[(x_k - \hat{x}_k)(x_k - \hat{x}_k)^T] = P_k$$

The a posteriori state estimation Equation 4.17 reflects the mean of the state distribution which is normally distributed if the conditions of normal probability

distribution with process noise covariance $\boldsymbol{Q_k}$ and $\boldsymbol{R_k}$ holds. The a posteriori estimate covariance $P_k = E[e_k e_k^T]$ reflects the variance of the state distribution such as

$$p(x_k|z_k) \sim N(E[x_k], E[(x_k - \hat{x}_k)(x_k - \hat{x}_k)^T]) = N(\hat{x}_k, P_k) \quad (4.20)$$

After the introduction of the computational and probabilistic background of the Kalman Filter, the discrete Kalman Filter Algorithm is presented. Kalman Filter is used to estimate the states of a system by utilizing the measured output as a feedback term even when the available measurement is noisy. The equations involving the Kalman filter falls into two distinct groups such as time update and measurement update equations. The time update equations are used to project forward the current states and error covariance estimates to obtain a priori estimates for the next time step while the measurement update equations are responsible for incorporating the new measurement into a priori estimate to obtain an improved a posteriori estimate. With this form Kalman Filter is in fact a predictor and corrector algorithm as shown in Figure 4.4

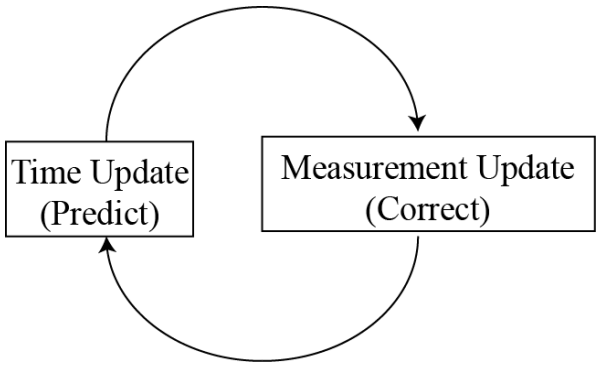

Figure 4. 4 Summary of the Kalman Filter

The specific equation for the time and measurement updates are given below

$$\widehat{\boldsymbol{x}}_{\boldsymbol{k}}^{-} = \boldsymbol{A}\widehat{\boldsymbol{x}}_{\boldsymbol{k-1}} + \boldsymbol{B}\boldsymbol{u}_{\boldsymbol{k}}$$

$$\underbrace{\boldsymbol{P}_{\boldsymbol{k}}^{-} = \boldsymbol{A}\boldsymbol{P}_{\boldsymbol{k-1}}\boldsymbol{A}^{\boldsymbol{T}} + \boldsymbol{Q}}_{Time\ Update\ Equations} \tag{4.21}$$

$$\boldsymbol{K}_{\boldsymbol{obs}} = \boldsymbol{P}_{\boldsymbol{k}}^{-}\boldsymbol{C}^{\boldsymbol{T}}(\boldsymbol{C}\boldsymbol{P}_{\boldsymbol{k}}^{-}\boldsymbol{C}^{\boldsymbol{T}} + \boldsymbol{R})^{-\boldsymbol{1}}$$

$$\widehat{\boldsymbol{x}}_{\boldsymbol{k}} = \widehat{\boldsymbol{x}}_{\boldsymbol{k}}^{-} + \boldsymbol{K}_{\boldsymbol{obs}}(\boldsymbol{y}_{\boldsymbol{k}} - \boldsymbol{C}\widehat{\boldsymbol{x}}_{\boldsymbol{k}}^{-})$$

$$\underbrace{\boldsymbol{P}_{\boldsymbol{k}} = (\boldsymbol{I} - \boldsymbol{K}_{\boldsymbol{obs}}\boldsymbol{C}\boldsymbol{P}_{\boldsymbol{k}}^{-})}_{Measurement\ Update\ Equations}$$

The update equations of the Kalman Filter shows iterative nature. Such property of the Kalman Filter is in fact extremely appealing since it makes practical implementation much more feasible than Wiener Filters. In this chapter, the observer gain $\boldsymbol{K}_{\boldsymbol{obs}}$ is calculated offline. The convergence of the $\boldsymbol{K}_{\boldsymbol{obs}}$ usually takes place within first 50 iterations. As initial conditions, the P_k^- is selected as a large value while the estimated state $\hat{x}_k^-$ is selected as zeros.

In order to calculate the estimated state values, the a priori state estimation $\widehat{x}_k^-$ part of the time update equations and the a posteriori state estimation $\hat{x}_k$ part of the measurement update equations are combined. The combination of those equations gives

$$\widehat{\boldsymbol{x}}_{\boldsymbol{k+1}} = \boldsymbol{\Phi}\widehat{\boldsymbol{x}}_{\boldsymbol{k}} + \boldsymbol{\Gamma}\boldsymbol{u}_{\boldsymbol{k}} + \boldsymbol{K}_{\boldsymbol{obs}}\boldsymbol{y}_{\boldsymbol{k}}, where$$

$$\boldsymbol{\Phi} = (\mathbf{I} - \mathbf{K}_{\boldsymbol{obs}}\mathbf{C})\mathbf{A}, \tag{4.22}$$

$$\boldsymbol{\Gamma} = (\mathbf{I} - \mathbf{K}_{\boldsymbol{obs}}\mathbf{C})\mathbf{B}$$

The block diagram of the Kalman Filter is shown in Figure 4.5

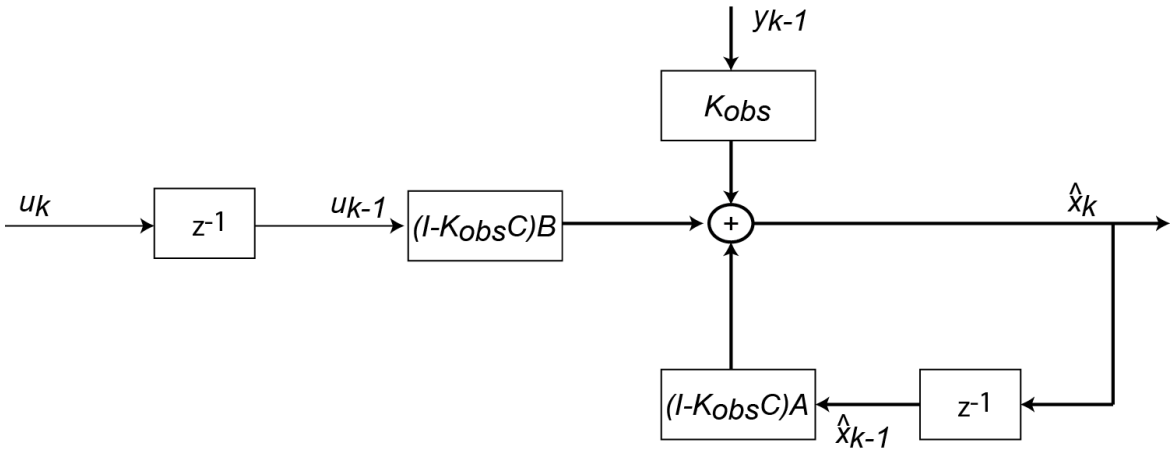

Figure 4. 5 Block Diagram of the Kalman Filter

The combination of the Kalman Filter and the LQR is the basic form of the LQG. In Figure 4.6 the LQG block diagram combining the Kalman filter and the LQR approach is shown.

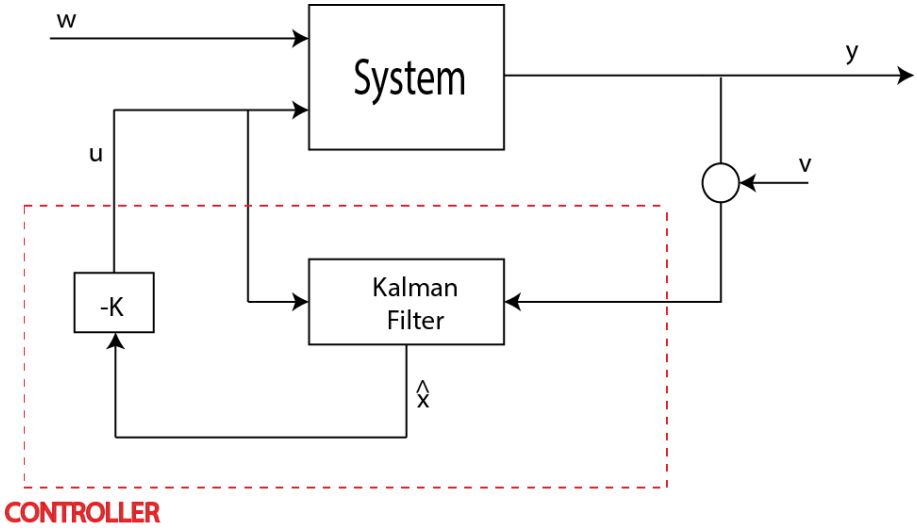

Figure 4. 6 Block Diagram of the LQG Algorithms

4.4 Experimental Set-Up

In this section, the experimental set-up used for the demonstration of the approach for implementing AVC on the commercial vehicle is presented. In Figure 4.7 the vehicle used in the study is shown.

Figure 4. 7 The Commercial Vehicle

The structure is made of steel with thickness of 1.2mm. In contrast to previous structures, there are the damping materials and the protective layers as well as the additional substructures due to fuel line and tire assembly on the outer side of the vehicle as shown in the Figure 4.8.

Figure 4. 8 Outer Side of the Wheelhouse

4.4.1 System Architecture

In this section, details of the experimental configuration used to verify the efficiency of our approach for both algorithms is shown. The structure is a commercial vehicle produced by the Ford OTOSAN Company. The rear left wheelhouse is selected as the host structure for implementing the active vibration control. The wheelhouse was found to be a potential problem panel based on the preliminary studies performed on the vehicle.

The experimental setup is composed of the vehicle, PZT actuators and sensors, controller unit and a signal analyzer. Details of the experimental set-up and the components are shown in Figure 4.9

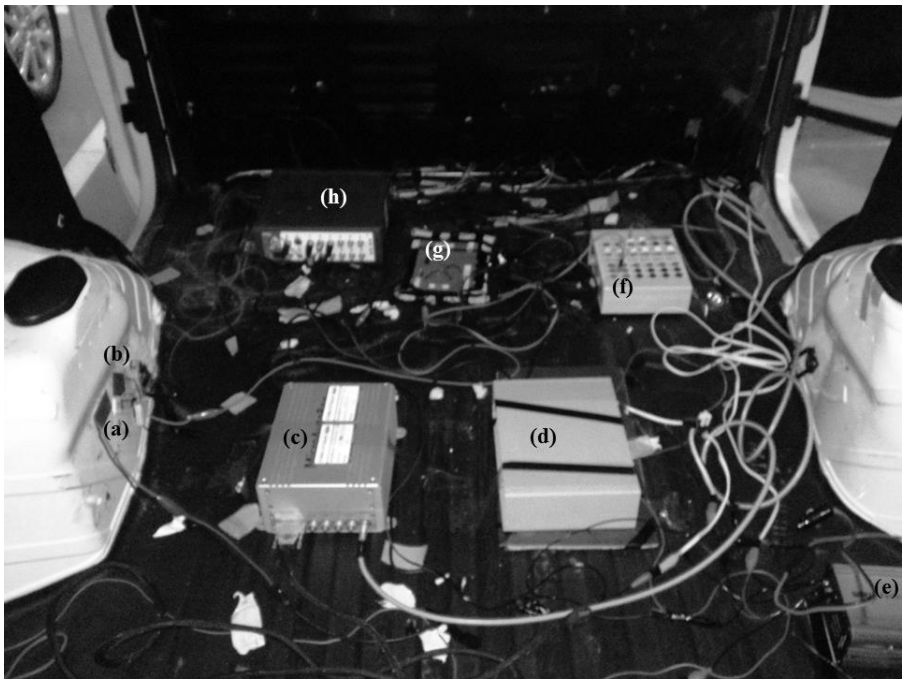

Figure 4. 9 Details of the experimental set-up a) PZT actuator b) PZT sensor c) DSpace Autobox d) PZT Amplifier e) DC-DC Inverter f) Autobox Connector g) Signal Conditioner h) Signal Analyzer

The piezoelectric actuators and sensors are the PI P876.A12 bender type actuators which are explained in section 2.5.1. Those are the high voltage low weight actuators which do not affect the dynamic characteristics of the system. Dspace Autobox 1401/1507 is used as the controller. Unlike NI-PCI 6229, the DSpace Autobox accepts the signal level of 0-5V as input and 0-4.56V output. Thus a signal conditioner consisting passive capacitors, resistors and active op-amps are built to ensure the proper operation of the controller. The signal conditioner configuration is shown in Figure 4.10

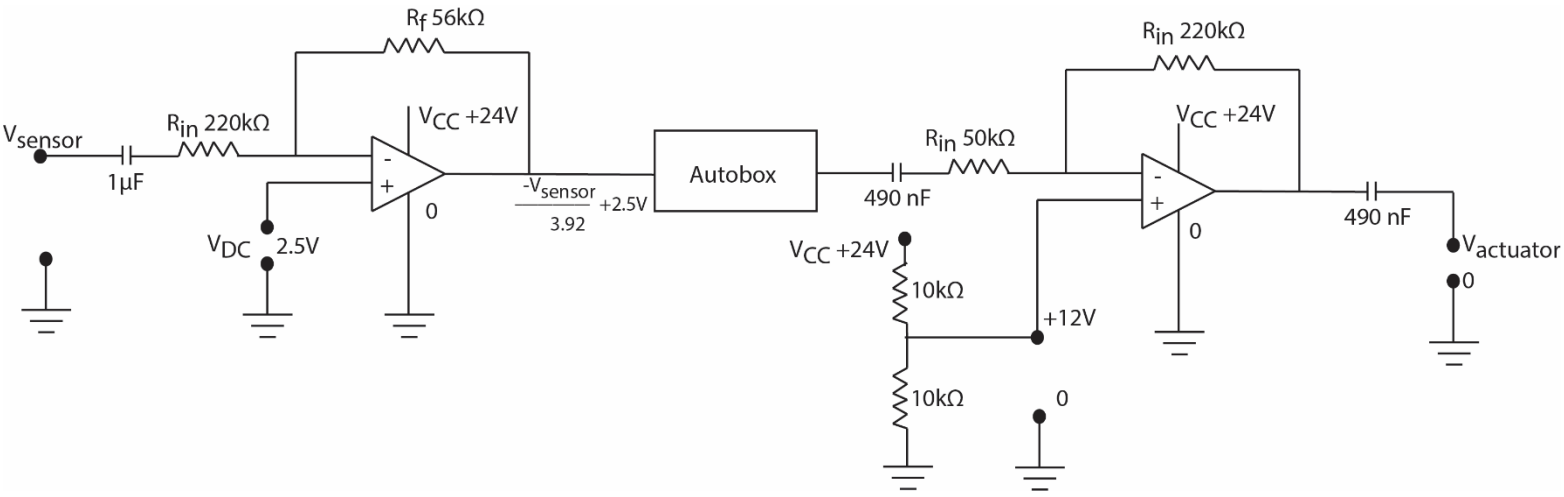

Figure 4. 10 Circuit Diagram of the Signal Conditioner

The values of the passive elements of the circuit shown above are tuned by trial error to ensure the desired signal characteristics between the sensor input and the autobox output. The op-amp used for the application is the LM324N single supply op-amp. The LM324N is rail to rail type and suitable for the usage in single supply with low-noise characteristics. The signal conditioner is composed of two inverting amplifiers in DC amplification mode. In this configuration, the sensor signal is shifted by V_{DC} and divided by 3.92. In the autobox, the DC component is removed and the controller algorithm is implemented to generate the output signal. Since the output channel of the autobox generates the values between 0-4.56V, the DC shift to the calculated output is a must. For this reason, the calculated signal is summed with 2.28V in the autobox for ensuring the signal level to be in positive range. The output channel of the autobox is then passed through a 490nF capacitor to remove the DC component. Then, the signal is amplified around 12VDC using the second inverting amplifier in the configuration. Using another 490nF capacitor the 12VDC component of the signal is removed and delivered to PZT amplifier. The Figure 4.11 shows the signal conditioning unit of the setup explained above

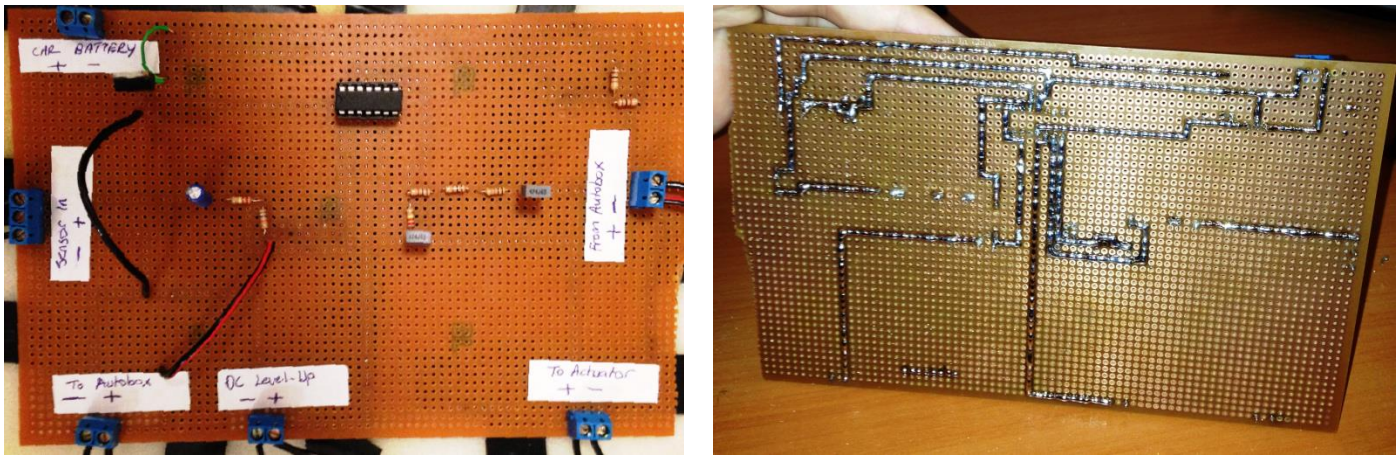

Figure 4. 11 Signal Conditioner

The disturbance source is the road induced vibrations through the wheels. The road tests were performed on a track at Koç University. The test drive was performed on cobble stone road. The tests are performed at 2nd gear while the vehicle speed was 40kph which effectively excited the target mode of the wheelhouse. In Figure 4.12, the test track is shown

Figure 4. 12 Test track and the Components of the Road

4.4.2 Sensor/Actuator Placement

The control authority for the targeted frequency range is crucial in vibration control for achieving good performance while suppressing the vibrations. The PZT actuators used in study are the strain type actuators and the high strain regions are the suitable regions for effective operation of the PZT actuators [41]. To identify such regions, experimental modal analysis is performed on the wheelhouse. 18 measurement points are selected to perform experimental modal analysis. A shaker is used to excite the structure for the modal analysis while 4 set of accelerometers are used for the measurement. Figure 4.13 shows the experimental modal analysis configuration for the wheelhouse.

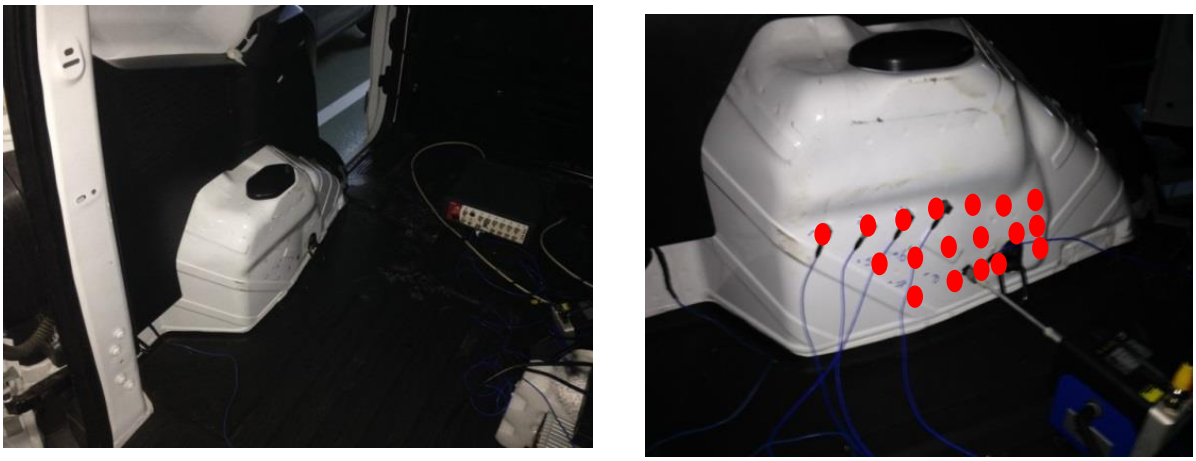

(a)

Figure 4. 13 a) The rear left wheelhouse b) The measurement points for modal analysis

After the measurements of the modal analysis are completed, the average of all measurements is obtained to examine the modal frequencies and all individual measurements are used to examine mode shapes. Figure 4.14 shows the average results of the FRF measurements completed through the modal analysis.

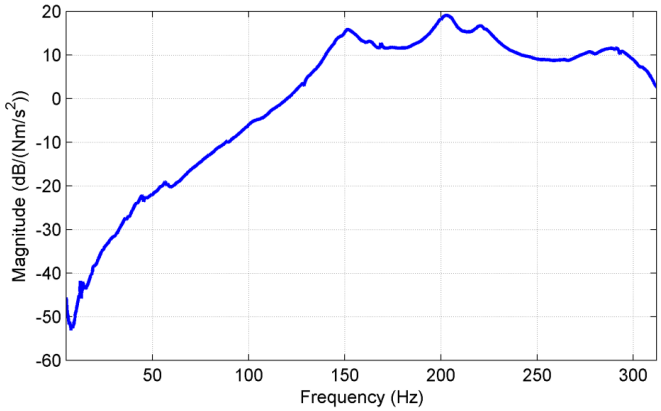

Figure 4. 14 Average of the measurements obtained through the modal analysis

The low frequency modes of the wheelhouse are listed in Table 4.1 while the mode shapes are shown in Figure 4.15.

Table 4. 1 Results of the Experimental Modal Analysis

	Mode 1	Mode 2	Mode 3
Experimental	152 Hz	202.9 Hz	221.1 Hz

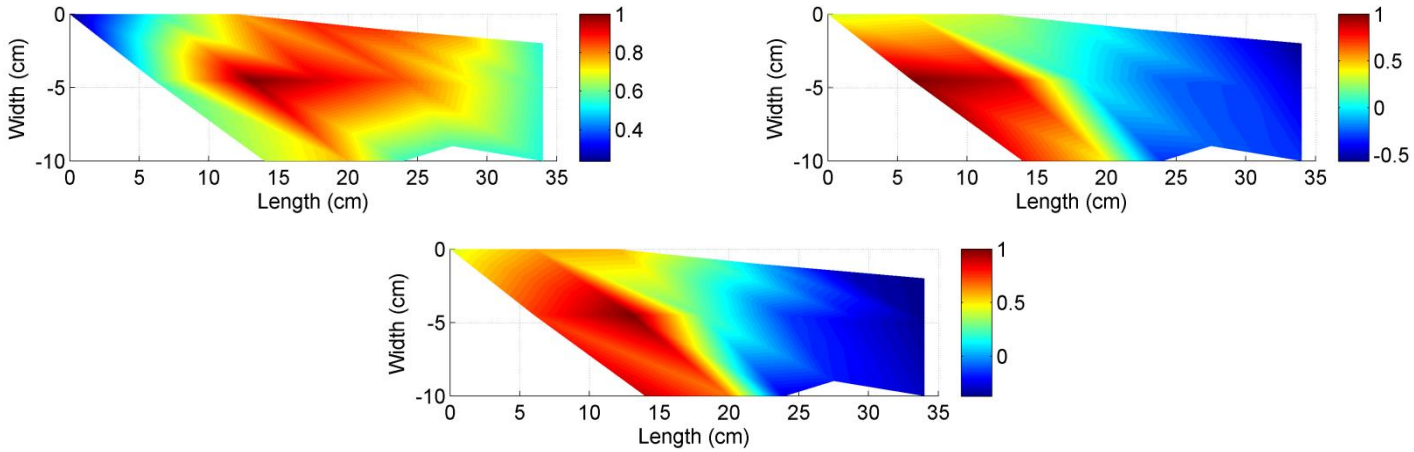

Figure 4. 15 Mode Shapes of the Wheelhouse

Based on the evaluations of the modal properties, the PZT actuator and sensors are located on the positions shown in Figure 4.16.

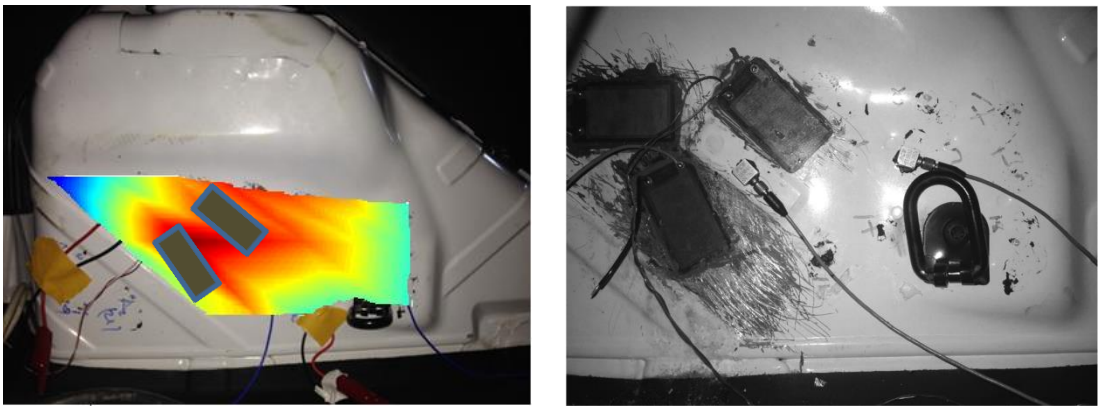

(a) **(b)**

Figure 4. 16 a) Mode Shape of the Structure for the first mode b) Piezoelectric patch locations on the structure

Please note that the sensor and actuator are attached on the surface different from the location described in section 3.5.2. The reason for such difference is the presence of the components on the other side of the vehicle which increases thickness and decrease the efficiency of the PZT patches for those positions. The dimension costraints and the assembly elements of the wheelhouse yielded such positioning of the sensor and actuator.

4.4.3 Modelling of the System

In this section, the procedure for the system identification of the vehicle is presented. For this purpose, frequency domain behavior of the wheelhouse is obtained for the sensor/actuator position described in the section 4.4.2. MATLAB is used for modeling and control system design.

FRF measurements of the system are performed using an actuator PZT patch, a sensor PZT patch and a data acquisition system. A sine sweep signal is generated to drive the actuator PZT patch using output channel of the data acquisition system and specified as the reference signal for the FRF measurement. Sensor PZT patch is used to acquire data at the sensor location and this information is transmitted to the data acquisition unit.

The system identification procedure is completed for the operating condition of the vehicle. For that reason there existed a road induced disturbance at the sensor location and this effect corrupted the measurements. It was minimized by taking the average of the FRF measurements. Thus it is important to have as many averaging of the signal as possible. The track that was presented in section 4.4 enables the driving of the vehicle for 30 seconds with the specified operation conditions. The target frequency range is selected as 50-300 Hz since the problematic frequency lies within this range and the duration of the sweep sine is adjusted to 30 seconds since the duration of the measurement during operation is 30 seconds. Furthermore, 10 different measurements are completed and averaged under the same operation condition to increase the number of FRF measurements such that effect of the disturbances can be minimized.

During the measurements, piezoelectric patch is driven with the sine-sweep signal. It took 30 seconds for the signal to increase from 50 Hz to 300 Hz. Sensor data is collected with block size of 1024 for each run. 37 averages are taken to generate better results for each run and a total of10 runs were completed. Figure 4.17 shows the schematic of the experimental set-up for the system identification.

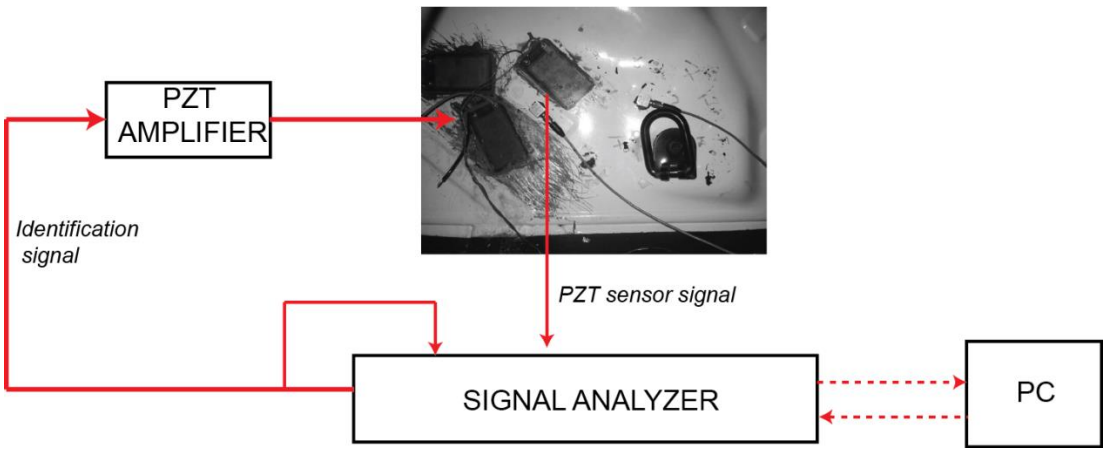

Figure 4. 17 Schematic of the Experimental Set-Up for System Identification

Later, the FRF measurements acquired from the Signal Analyzer is used to derive the system model. The model is in the form of a state-space representation and it is obtained by using the fitsys command in MATLAB. Thus, the states do not have any physical meaning. The matrices **A**,**B**,**C** and **D** matrices of the state space representation are also created by the least square algorithm using the fitsys command in MATLAB.

A 12th order model is found to be sufficient to represent the dynamics in that frequency range. The Figure 4.18 shows the measured FRF and the model response.

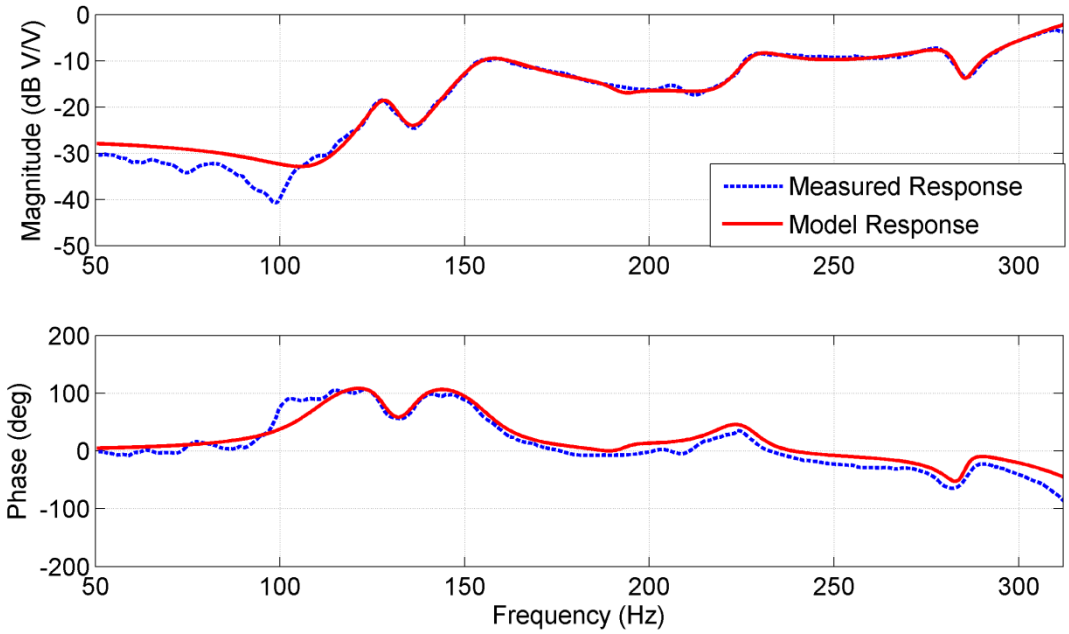

Figure 4. 18 FRF of the Actual Response and Model Response

First, the continuous time model of the system in state space form is generated by using the measured FRF. Later, "c2d" command in MATLAB is used to obtain A, B, C, and D matrices.

The model is then used for the controller design. Since LQG algorithm is used, Kalman filter implementation is required. A disturbance modelling technique is used in

order to use LQG for disturbance rejection[60]. This technique requires a disturbance model and it must be included in the plant model to generate the control action. However, it is not possible to measure the disturbance level at the source to generate a disturbance model. Thus, a virtual modeling approach is used.

In this technique, disturbance can be modeled as an output of a filter excited with white noise if the disturbance spectrum is known [60]. It is possible to consider the disturbance model as follows

$$\dot{\boldsymbol{x}}_{\boldsymbol{f}} = \boldsymbol{A}_{\boldsymbol{f}}\boldsymbol{x}_{\boldsymbol{f}} + \boldsymbol{B}_{\boldsymbol{f}}\boldsymbol{w} \tag{4.24}$$

$$\boldsymbol{y}_{\boldsymbol{f}} = \boldsymbol{C}_{\boldsymbol{f}}\boldsymbol{x}_{\boldsymbol{f}}$$

Here A_f, $B_f$and C_f are the system matrices with the appropriate dimensions. The x_f is the disturbance states and w is the zero mean Gaussian white noise process.

During the operation of the vehicle, it is known that there is a significant narrow-band effect of the road induced disturbances on the system around 150Hz. For that reason, the statistical properties of the induced harmonic on the sensor patch should be known. This can be done by measurement of the time domain signal for the open loop case. The bandwidth is selected between 145-155Hz and the signal is filtered to understand the statistical properties of the disturbances on the system. Results of the 10 different measurements showed that the variance of the signal component for 145-150 Hz bandwidth is 0.005 and by assuming a zero-mean white noise with covariance of 0.01 generates such output. Then using this information a virtual disturbance model is generated in MATLAB/Simulink. The system matrices of the generated disturbance model are shown in Equation 4.25 and associated frequency response of the disturbance model is given in Figure 4.19.

$$A_f = \begin{bmatrix} 0.9828 & 0.0002 \\ -171.4438 & 0.9769 \end{bmatrix}, B_f = 1e-3\begin{bmatrix} 0 \\ 0.1982 \end{bmatrix}, C_f = [300000 \quad 0] \tag{4.25}$$

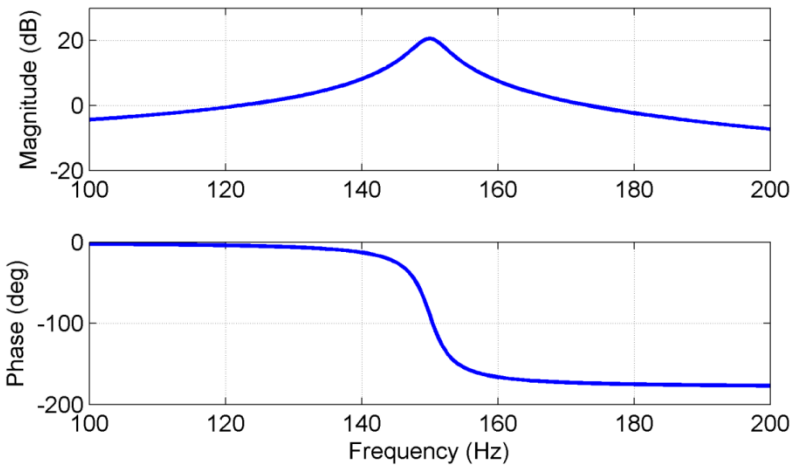

Figure 4. 19 FRF of the Virtual Disturbance Model

Consider the plant as a combination of the disturbance model and the control actuator/sensor model given in section 4.3.1.2. For the disturbance rejection, instead of considering the disturbance as an additional effect, now, the disturbance is included as a system input by utilizing the virtual disturbance model given in Equation 4.24 in combination with the actuator/sensor dynamics the following form where [60].

$$\begin{bmatrix} \dot{\boldsymbol{x}} \\ \dot{\boldsymbol{x}}_{\boldsymbol{f}} \end{bmatrix} = \begin{bmatrix} \boldsymbol{A} & \boldsymbol{BC}_{\boldsymbol{f}} \\ \boldsymbol{0} & \boldsymbol{A}_{\boldsymbol{f}} \end{bmatrix} \begin{bmatrix} \boldsymbol{x} \\ \boldsymbol{x}_{\boldsymbol{f}} \end{bmatrix} + \begin{bmatrix} \boldsymbol{0} \\ \boldsymbol{B} \end{bmatrix} \boldsymbol{u} + \begin{bmatrix} \boldsymbol{B}_{\boldsymbol{f}} \\ \boldsymbol{0} \end{bmatrix} \boldsymbol{w} \tag{4.26}$$

$$\boldsymbol{y} = [\boldsymbol{C} \quad \boldsymbol{0}] \begin{bmatrix} \boldsymbol{x} \\ \boldsymbol{x}_{\boldsymbol{f}} \end{bmatrix} + \boldsymbol{v}$$

After generation of the augmented model, the measurement noise covariance and the disturbance are incorporated into Kalman filter design as 0.00075 and 0.01 The measurement noise covariance is found by measuring the noise level in the sensor when the system is stationary and no excitation is present on the system. It is found that the covariance of the sensor measurement noise is 0.00075. The measurement noise covariance is unknown but as previously explained, level of 0.01 covariance is assumed for the disturbance on the system.

Then the LQR approach is implemented for the optimal feedback control using dlqr command in MATLAB. The **Q** and **R** matrices of the LQR implementation are chosen as **Q=180*** $\boldsymbol{I_{12x12}}$ and R=0.1. Please note that the disturbance states are unknown and should not be incorporated into the control action. Thus, the corresponding values of the $\boldsymbol{K_{lqr}}$ to those states must be 0.

4.5 Controller Implementation

The controller architecture is shown in Figure 4.20. It is not possible to implement the collocated configuration. Such impossibility is due to the presence of the tire assembly and vulnerability of the sensor to the operational conditions (such that the dust, stones etc.) on the outer side of the structure. Furthermore, the cabling requirements for data transfer are also very problematic in the collocated configuration. However the sensor actuator pair is located as close as possible to each other to avoid the delay between the control actuation and the effect of the actuation on the sensor. DSpace Autobox 1401/1507 is used for the controller implementation in combination with the previously described signal conditioner unit. The performance of the controller is monitored utilizing a signal analyzer. The control signal is then transferred to the control actuator utilizing the E413.D2 type signal amplifier.

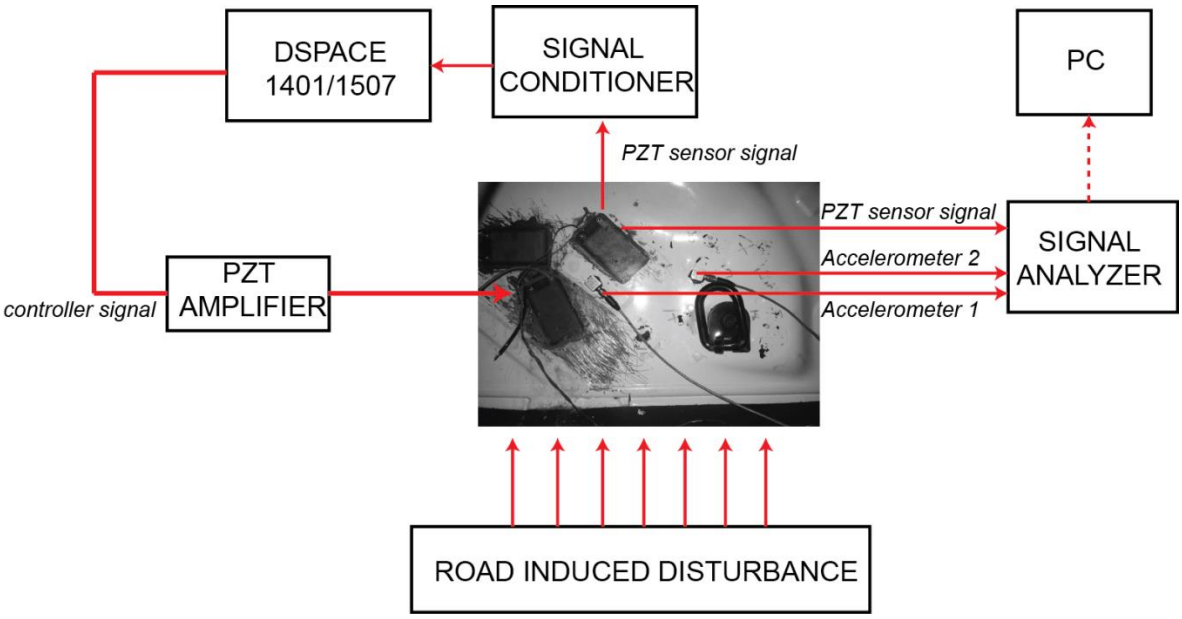

Figure 4. 20 Schematics of the controller configuration

4.6 Results

In this section, experimental results of the PPF and LQG algorithms for AVC are presented. The autospectrum measurements are used for the controller performance evaluation since the reference signal is not available for the real operating conditions.

4.6.1 PPF Performance

In this section the performance of the PPF algorithm is presented. As previously explained the damping ratio and the gain of the PPF algorithm are selected as 0.15 and -2.2. Figure 4.21 shows the vibration suppression performance on different locations of the wheelhouse.

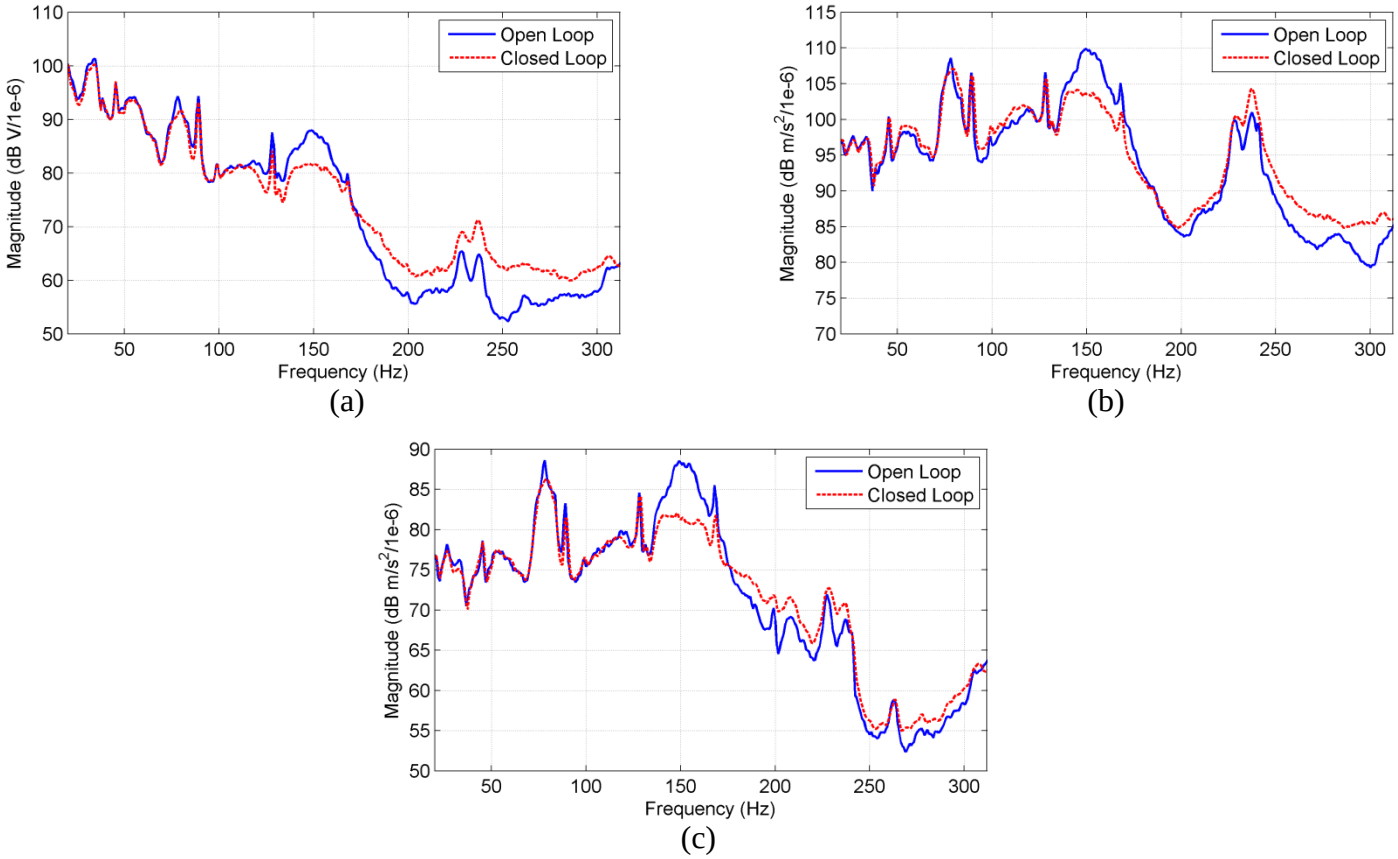

Figure 4. 21 Controller performance for open loop and closed loop cases a) PZT Sensor b) Accelerometer 1 c) Accelerometer 2

From Figure 4.21 it is obvious that the vibration of the wheelhouse is suppressed effectively around 150 Hz where the contribution of the road induced disturbance is high. However, an increase in the vibration level is observed in the 200-300Hz. frequency range The reason for the amplification of the vibration level can be explained by the closed loop dynamics of the system.

The FRF of the closed loop response of the system is shown in Figure 4.22. The closed loop dynamics of the system are obtained by convolving the sensor/actuator model with the transfer function of the PPF controller. From the figure, it is observed that the closed loop gain of the mode at 220Hz is -4dB.. Furthermore, the phase behavior of the

closed loop system dynamics suggest that the controller output fails to suppress the vibrations. In the following section, the LQG controller is presented.

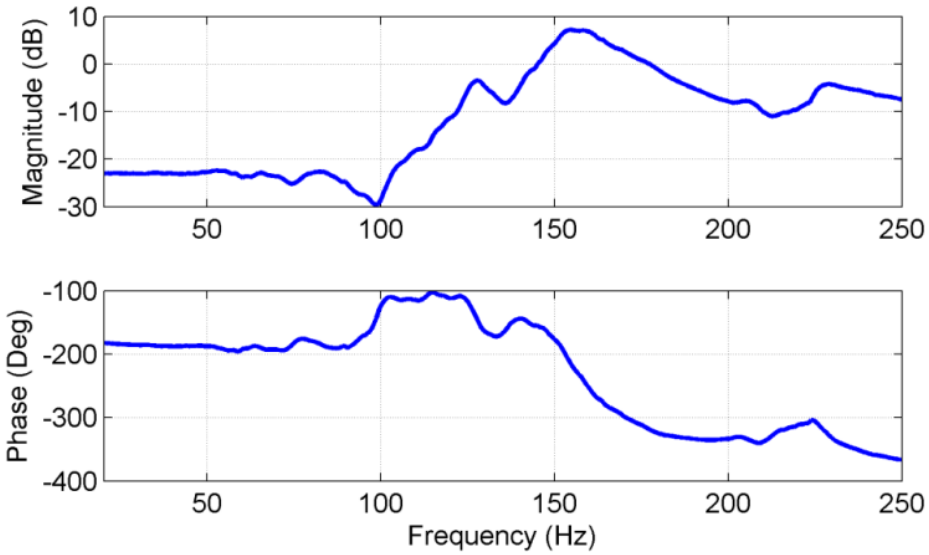

Figure 4. 22 Composite response of the System with PPF controller

4.6.2 LQG Performance

In this section performance evaluation of the LQG controller for the AVC of the moving vehicle is presented. As indicated in section 4.7.1, the PPF controller amplified the magnitude of the frequency response in 200-300Hz bandwidth.

In order to solve the amplification problem in 200-300 Hz region, LQG controller is implemented. Using the design methodology in section 4.3 and the model described in section 4.4.3, LQG controller is designed and implemented. The measurements are completed for open loop and closed loop cases on the exactly same track with the PPF. Figure 4.23 shows the performance of the LQG controller.

Figure 4.23 shows that the vibration level is suppressed around 150Hz while the vibration amplification of the frequency band 200-300Hz is significantly reduced. The vibration suppression performance of the LQG and the PPF controllers around 150Hz are compared in Table 4.2.

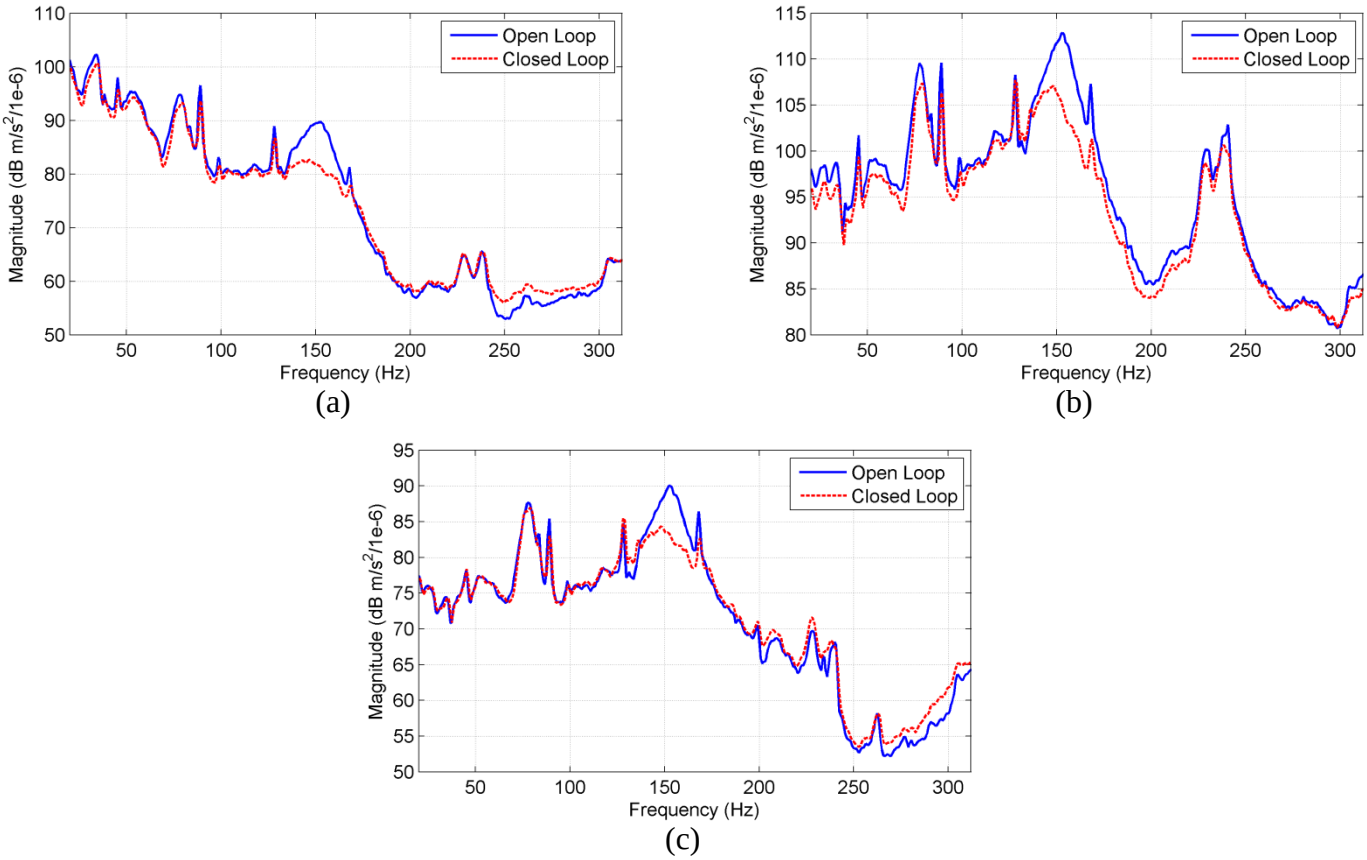

Figure 4. 23 Controller performance for open loop and closed loop cases a) PZT Sensor b) Accelerometer 1 c) Accelerometer 2

Table 4. 2 Vibration Suppression Performances of the PPF and LQG for the Sensor Locations

Sensor Type	***PPF Performance***	***LQG Performance***
PZT Sensor	6.4 dB	6.8 dB
Accelerometer 1	6 dB	6.2 dB
Accelerometer 2	6.3 dB	6.1 dB

4.7 Conclusion

In this chapter, an active vibration control configuration for controlling the road induced disturbances on a vehicle is presented. The vehicle used is a commercial vehicle manufactured by Ford motor Company. The tests are performed on a prespecified track while the vehicle is moving with 40kph at 2^{nd} gear. Since the reference signal is not measurable, autospectrum of the PZT sensor is measured as the indicator of the controller performance. Furthermore, two accelerometers are used in addition to monitor the vibration suppression level on two different regions of the wheelhouse. Results showed that the PPF algorithm has capability of the controlling the vehicle level disturbances for the operation conditions at the target frequency by ~6.4 dB. However, the level of vibration for the 200-300Hz band is excited because of the current control configuration. The LQG implementation solved the problem by its model based optimal approach with probabilistic observation capability. Thus, the vibration level on the structure is attenuated by ~6.8 dB around 150 Hz while the excitation on the high frequency modes is eliminated.

Chapter 5

DISCUSSION AND CONCLUSION

The passive isolation techniques are not generally feasible and efficient for low frequency vibration suppression; instead, Active Vibration Control (AVC) can be used to suppress the low frequency vibrations. The implementation of the AVC requires various control architectures using different kinds of sensor actuator configurations. The contributions of this thesis in the field of AVC can be analyzed in two main cathegories. First cathegory is to develop IIR filtering based adaptive approaches for active vibration control systems and demonstrate the efficiency of the developed methodologies on two different case studies. The other category is to develop a methodology to suppress vibrations on the wheelhouse of a newly designed commercial vehicle produced by Ford OTOSAN during operating conditions.

In chapter 2, adaptive IIR filtering technique was implemented in combination with the online modelling secondary path modelling methodology to develop a novel controller configuration for Active Vibration Control. In order to develop such a methodology, Filtered-U LMS (FULMS) algorithm was used to update the controller filter parameters while a recently developed online secondary path modelling algorithm continuously updated the modeling filter parameters. The sensor signal was transferred to a computer and the developed methodology was implemented via a rapid prototyping controller unit to generate the output for vibration suppression. The active vibration control methodology was implemented on the first three low- frequency modes of a flexible vehicle panel to demonstrate the efficiency of the developed approach. Furthermore, a simulation model that mimics the controller configuration was used to demonstrate and predict the vibration suppression behavior before the experiments took place. The results were evaluated for both periodic and random input types in time and frequency domains. The simulation and experimental performance of the FULMS controller with online secondary path modeling

was compared with the FXLMS counterpart. The results showed that FULMS with online secondary path modeling achieved better controller performance in terms of convergence speed and steady state error compared to the FXLMS counterpart. Results indicated that the FULMS was an effective alternative to the FXLMS in active vibration control applications.

In Chapter 3, implementation of Steiglitz-McBride (SM) adaptive IIR filtering technique for active vibration control was demonstrated on an experimental setup and a new approach was developed to enhance its computational efficiency. For this purpose, in the first step, the Steiglitz-McBride algorithm for active vibration controller was demonstrated on an experimental setup which included a quarter body in white vehicle where PZT actuators are attached on one of the panels. Later, the computational efficiency of the algorithm was improved by developing a novel configuration (hybrid SM) which combines the frequency domain adaptive filtering methodology with originally proposed algorithm. Efficiency of the developed configuration was demonstrated both experimentally and numerically. The sensor signal was transferred to the computer via a PCI interface and the methodology was implemented via a rapid prototyping controller unit to generate the output for vibration suppression. A shaker was used to generate the undesired vibrations. The vibration control was implemented on the low frequency modes of the structure (up to 220Hz) to demonstrate the efficiency of the approach. Furthermore, a simulation model of the experimental setup was developed and used to demonstrate and predict the vibration suppression behavior before the experiments. The results were evaluated in time and frequency domains for the case of random input. The results showed that both of the algorithms are beneficial in terms of vibration suppression and showed similar performances. The proposed method was found to be more efficient since computational performance of the algorithm was increased by 28.9% for the case study presented.

In Chapter 4, an active vibration control implementation for controlling the road induced vibrations on a vehicle in real operating conditions was presented. The vehicle that was used in the experiments was produced by Ford OTOSAN. After some preliminary studies on the vehicle, the wheelhouse was found to be a potential component to generate noise inside the cabin. Positive Position Feedback (PPF) and LQG controllers were implemented and compared. In the first step of the control implementation, the PZT actuator and sensor locations were determined on the wheelhouse. DSpace autobox 1401/1507 model real time controller was used to implement the controller algorithms. In order to use DSpace autobox, a signal conditioner unit was built for modification of the sensor and actuator signal to ensure proper signal processing. The tests were performed on a track while the vehicle was moving with 40 kph at 2^{nd} gear. Those operation conditions were selected such that structural mode of the wheelhouse was excited while driving the vehicle. Performances of the controller for both of the algorithms were evaluated for the open loop and closed loop cases. Since the reference signal was not measurable, autospectrum of the PZT sensor was measured as the indicator of the controller performance. Furthermore, two accelerometers were used in addition to monitor the vibration suppression level on two different regions of the wheelhouse. The measurements were collected in 10 different road tests and then averaged to eliminate the noise in the measurements. Results showed that the PPF algorithm was able to suppress the wheelhouse vibrations for the operation conditions at the targeted frequency by 6.4 dB. However, some amplification of the higher modes was observed. The LQG controller was even a better solution to the problem by its model based optimal approach with probabilistic observation capability. The vibration level on the structure was attenuated by 6.8 dB around 150 Hz while the amplification at the high frequency modes was eliminated.

The methodologies developed in this thesis can be improved in the following ways. In chapter 2 and 3, one can develop a better approach to have an accurate measurement of

the disturbance source. In vibration control, the sources of the disturbances are usually not clear and even if the source is known it is usually impossible to put a sensor at those locations. For that reason, prior to implementation of the developed algorithms, control designer should consider the availability of the reference measurements. In chapter 2, another drawback of the developed methodology is the possibility of convergence of the filter parameters to the local optimum. The only way to avoid such problem is to select proper step size for the adaptive algorithm and select appropriate initial conditions for the adaptive filter parameters. In chapter 2 and chapter 3, the unstability is another problem that must be considered during the implementation of developed algorithms. These problems can be solved with conventional methods; however it may yield extremely conservative controller parameters. In chapter 4, the developed methodology is effective in terms of vibration suppression of the wheelhouse. However, a more compact controller unit integrated with the vehicle electronic components is required such that this module can be used in the new models. While doing that the high voltage requirements, robustness and the price should be considered. Some improvements are also required before integrating the controller unit to the vehicle. For example, the developed controller algorithms can be integrated into the Electronic Control unit (ECU) of the vehicle. The high voltage connections within the vehicle can be successfully isolated by properly designing the electrical connection layout. Also voice coil actuators can be used instead of the PZT actuator.

As a future topic, self-sensing configuration of the piezoelectric materials can be studied. Self-sensing property of the piezoelectric materials is advantageous since in case of sensor failures, piezoelectric actuators can be used as sensors. This property of the piezoelectric materials makes them more effective for commercial applications. Furthermore, it is possible to use piezoelectric actuators in self-sensing configuration where

the same actuator serves as sensor as well. Such configuration decreases cost of the application and offers highest level of the collocated configuration achievable.

BIBLIOGRAPHY

[1] T. Bailey and J. E. Hubbard, "Distributed piezoelectric polymer active vibration control of a cantilever beam," *Journal of Guidance Control and Dynamics,* vol. 8, pp. 605-611, 1985.

[2] E. F. C. a. J. Luis, "Use of piezoelectric actuators as elements of intelligent structures," *AIAA Journal,* vol. 25, pp. 1373-1385, 1987.

[3] S. S. Rao and M. Sunar, "Piezoelectricity and Its Use in Disturbance Sensing and Control of Flexible Structures: A Survey," *Applied Mechanics Reviews,* vol. 47, pp. 113-123, 1994.

[4] R. G. Loewy, "Recent developments in smart structures with aeronautical applications," *Smart Materials and Structures,* vol. 6, p. R11, 1997.

[5] U. Aridogan and I. Basdogan, "A review of active vibration and noise suppression of plate-like structures with piezoelectric transducers," *Journal of Intelligent Material Systems and Structures,* May 27, 2015 2015.

[6] R. Alkhatib and M. F. Golnaraghi, "Active Structural Vibration Control: A Review," *The Shock and Vibration Digest,* vol. 35, pp. 367–383, September 2003.

[7] V. Gupta, M. Sharma, and N. Thakur, "Optimization Criteria for Optimal Placement of Piezoelectric Sensors and Actuators on a Smart Structure: A Technical Review," *Journal of Intelligent Material Systems and Structures,* vol. 21, pp. 1227-1243, August 1, 2010 2010.

[8] I. Chopra, "Review of state of art of smart structures and integrated systems," *AIAA Journal,* vol. 40, pp. 2145-2187, 2002.

[9] H. Hanselka, "Adaptronics as a key technology for intelligent lightweight structures," *Advanced Engineering Materials,* vol. 3, pp. 205-215, 2001.

[10] S. Hurlebaus and L. Gaul, "Smart structure dynamics," *Mechanical Systems and Signal Processing,* vol. 20, pp. 255-281, 2006.

[11] V. Fakhari and A. Ohadi, "Nonlinear vibration control of functionally graded plate with piezoelectric layers in thermal environment," *{JOURNAL OF VIBRATION AND CONTROL},* vol. {17}, pp. {449-469}, {MAR} 2011.

[12] H. Okumura, R. Emi, and A. Sano, "Adaptive Two degree-of-freedom Vibration Control for Flexible Plate with Piezoelectric Patches," in *{2008 PROCEEDINGS OF SICE ANNUAL CONFERENCE, VOLS 1-7}*, 2008, pp. {207-210}.

[13] U. Boz, S. Kulah, U. Aridogan, and I. Basdogan, "Analog Velocity Feedback Controller for Vibration Suppression and Sound Attenuation," *ASME Conference Proceedings,* vol. 2011, pp. 207-214, 01/01/ 2011.

[14] T. Ryall, "Two considerations for the design of a robust optimal smart structure where control energy is expensive," in *{SMART STRUCTURES AND DEVICES}*, 2001, pp. {355-362}.

[15] U. Boz, U. Aridogan, and I. Basdogan, "A Numerical and Experimental Study of Optimal Velocity Feedback Control for Vibration Suppression of a Plate-Like Structure," *Low Frequency Noise, Vibration and Active Control,* vol. 34, pp. 343-360, 2015/06/01 2015.

[16] B. Chomette, S. Chesne, D. Remond, and L. Gaudiller, "Damage reduction of on-board structures using piezoelectric components and active modal control-Application to a printed circuit board," *MECHANICAL SYSTEMS AND SIGNAL PROCESSING,* vol. 24, pp. 352-364, FEB 2010.

[17] J. K. Hwang, C.-H. Choi, C. K. Song, and J. M. Lee, "Plate with piezoelectric actuators/sensors," *Mechatronics, IEEE/ASME Transactions on,* vol. 2, pp. 205-212, 1997.

[18] T. Sanda and K. Takahashi, "Flutter and vibration control of aluminum plate wing by piezoceramic actuators," in *{SMART STRUCTURES AND MATERIALS 1998: SMART STRUCTURES AND INTEGRATED SYSTEMS, PTS 1 AND 2}*, 1998, pp. {42-49}.

[19] A. Ohsumi, T. Inomata, and J. Sawada, "Modeling and control of elastic plates and cylindrical shells," in *{SICE 2003 ANNUAL CONFERENCE, VOLS 1-3}*, 2003, pp. {545-550}.

[20] C. Song, J. Hwang, J. Lee, and J. Hedrick, "Active vibration control for structural-acoustic coupling system of a 3-D vehicle cabin model," *{JOURNAL OF SOUND AND VIBRATION},* vol. {267}, pp. {851-865}, {OCT 30} 2003.

[21] M. Strassberger and H. Waller, "Active noise reduction by structural control using piezo-electric actuators," *{MECHATRONICS},* vol. {10}, pp. {851-868}, {DEC} 2000.

[22] M. Y. Yasin, N. Ahmad, and M. N. Alam, "Finite element analysis of actively controlled smart plate with patched actuators and sensors," *{LATIN AMERICAN JOURNAL OF SOLIDS AND STRUCTURES},* vol. {7}, pp. {227-247}, 2010.

[23] C. H. Hansen, *Active Control of Noise and Vibration*: CRC Press, 2013.

[24] Q. Huang, J. Luo, H. Li, and X. Wang, "Analysis and implementation of a structural vibration control algorithm based on an IIR adaptive filter," *Smart Materials and Structures,* vol. 22, p. 085008, 2013.

[25] A. Preumont, *Vibration Control of Active Structures : An Introduction*, 2 ed. New York: Kluwer Academic, 2002.

[26] A. Preumont, *Vibration control of active structures: an introduction*: Kluwer Academic Publishers, 2002.

[27] Y. Aoki, P. Gardonio, and S. J. Elliott, "Modelling of a piezoceramic patch actuator for velocity feedback control," *Smart Materials and Structures,* vol. 17, p. 015052, 2008.

[28] G. Caruso, S. Galeani, and L. Menini, "Active vibration control of an elastic plate using multiple piezoelectric sensors and actuators," *{SIMULATION MODELLING PRACTICE AND THEORY},* vol. {11}, pp. {403-419}, {AUG 15} 2003.

[29] A. Chellabi, Stepanenko Y. and S. Dost, "Direct Optimal Vibration Control of a Piezoelastic Plate," *Journal of Vibration and Control,* vol. 15, pp. 1093-1118, 2009.

[30] X.-J. Dong, G. Meng, and J.-C. Peng, "Vibration control of piezoelectric smart structures based on system identification technique: Numerical simulation and experimental study," *{JOURNAL OF SOUND AND VIBRATION},* vol. {297}, pp. {680-693}, {NOV 6} 2006.

[31] J. Han, J. Tani, and J. Qiu, "Active flutter suppression of a lifting surface using piezoelectric actuation and modern control theory," *{JOURNAL OF SOUND AND VIBRATION},* vol. {291}, pp. {706-722}, {APR 4} 2006.

[32] Y. Hu and A. Ng, "Active robust vibration control of flexible structures," *{JOURNAL OF SOUND AND VIBRATION},* vol. {288}, pp. {43-56}, {NOV 22} 2005.

[33] P. S. R. Diniz, *Adaptive Filtering: Algorithms and Practical Implementation*: Springer, 2008.

[34] B. Huang, Y. Xiao, J. Sun, and G. Wei, "A Variable Step-Size FXLMS Algorithm for Narrowband Active Noise Control," *Audio, Speech, and Language Processing, IEEE Transactions on,* vol. 21, pp. 301-312, 2013.

[35] Z. Yang, Q. Huang, J. Han, and H. Li, "Adaptive inverse control of random vibration based on the filtered-X LMS algorithm," *Earthquake Engineering and Engineering Vibration,* vol. 9, pp. 141-146, 2010/03/01 2010.

[36] I. S. Kim, H. S. Na, K. J. Kim, and Y. Park, "Constraint filtered-x and filtered-u least-mean-square algorithms for the active control of noise in ducts," *The Journal of the Acoustical Society of America,* vol. 95, pp. 3379-3389, 1994.

[37] S. Gao, Z. Gao, Y. Shao, J. Yi, and X. Zhu, "Performance analysis and comparison of FXLMS and FULMS algorithm for active structure vibration control," in *Advanced Computer Control (ICACC), 2010 2nd International Conference on*, 2010, pp. 197-201.

[38] J. J. Shynk, "Adaptive IIR filtering," *ASSP Magazine, IEEE,* vol. 6, pp. 4-21, 1989.

[39] M. T. Akhtar, M. Abe, and M. Kawamata, "A new variable step size LMS algorithm-based method for improved online secondary path modeling in active noise control systems," *Audio, Speech, and Language Processing, IEEE Transactions on,* vol. 14, pp. 720-726, 2006.

[40] M. T. Akhtar, M. Abe, and M. Kawamata, "Noise power scheduling in active noise control systems with online secondary path modeling," *IEICE Electronics Express,* vol. 4, pp. 66-71, 2007.

[41] U. Aridogan, I. Basdogan, and A. Erturk, "Analytical modeling and experimental validation of a structurally integrated piezoelectric energy harvester on a thin plate," *Smart Materials and Structures,* vol. 23, p. 045039, 2014.

[42] K. Steiglitz and L. E. McBride, "A technique for the identification of linear systems," *Automatic Control, IEEE Transactions on,* vol. 10, pp. 461-464, 1965.

[43] P. Stoica and T. Soderstrom, "The Steiglitz-McBride identification algorithm revisited--Convergence analysis and accuracy aspects," *Automatic Control, IEEE Transactions on,* vol. 26, pp. 712-717, 1981.

[44] X. Sun and G. Meng, "Steiglitz–Mcbride type adaptive IIR algorithm for active noise control," *Journal of Sound and Vibration,* vol. 273, pp. 441-450, 5/21/ 2004.

[45] S. M. Kuo, S. Kuo, and D. R. Morgan, *Active noise control systems: algorithms and DSP implementations*: Wiley, 1996.

[46] C. R. Johnson, Jr., M. G. Larimore, P. L. Feintuch, and N. J. Bershad, "Comments on and additions to "An adaptive recursive LMS filter"," *Proceedings of the IEEE,* vol. 65, pp. 1399-1402, 1977.

[47] X. L. Tang and C. M. Lee, "Time–frequency-domain filtered-x LMS algorithm for active noise control," *Journal of Sound and Vibration,* vol. 331, pp. 5002-5011, 11/5/ 2012.

[48] D. P. Das, D. J. Moreau, and B. S. Cazzolato, "A computationally efficient frequency-domain filtered-X LMS algorithm for virtual microphone," *Mechanical Systems and Signal Processing,* vol. 37, pp. 440-454, 5// 2013.

[49] J. J. Shynk, "Frequency-domain and multirate adaptive filtering," *Signal Processing Magazine, IEEE,* vol. 9, pp. 14-37, 1992.

[50] J. J. Shynk, R. P. Gooch, and B. Widrow, "A Frequency-Domain Adaptive Pole-zero Filter With Applications," in *Circuits, Systems and Computers, 1985. Nineteeth Asilomar Conference on*, 1985, pp. 299-303.

[51] H. Fan and Y. Yang, "Analysis of a frequency-domain adaptive IIR filter," *Acoustics, Speech and Signal Processing, IEEE Transactions on,* vol. 38, pp. 864-870, 1990.

[52] M. P. Nowak and B. D. Van Veen, "A constrained transform domain adaptive IIR filter structure for active noise control," *Speech and Audio Processing, IEEE Transactions on,* vol. 5, pp. 334-347, 1997.

[53] B. Rafaely and S. J. Elliot, "A computationally efficient frequency-domain LMS algorithm with constraints on the adaptive filter," *Signal Processing, IEEE Transactions on,* vol. 48, pp. 1649-1655, 2000.

[54] J. L. Fanson and T. K. Caughey, "Positive position feedback control for large space structures," *AIAA Journal,* vol. 28, pp. 717-724, 1990/04/01 1990.
[55] M. Ratnam, B. Bhikkaji, A. J. Fleming, and S. O. R. Moheimani, "PPF Control of a Piezoelectric Tube Scanner," in *Decision and Control, 2005 and 2005 European Control Conference. CDC-ECC '05. 44th IEEE Conference on*, 2005, pp. 1168-1173.
[56] R. C. Dorf and R. H. Bishop, *Modern control systems*: Pearson Prentice Hall, 2008.
[57] D. E. Kirk, *Optimal control theory: an introduction*: Dover Publications, 2004.
[58] G. Welch and G. Bishop, "An Introduction to the Kalman Filter," University of North Carolina at Chapel Hill1995.
[59] *Stochastic Models: Estimation and Control: v. 1: Estimation and Control*: Elsevier Science, 1979.
[60] L. A. Sievers and A. H. von Flotow, "Comparison of two LQG-based methods for disturbance rejection," in *Decision and Control, 1989., Proceedings of the 28th IEEE Conference on*, 1989, pp. 483-485 vol.1.